Dark Matter Particle Astrophysics: How Dark Matter Can Affect Subhalos, Neutrinos, and Neutron Stars

Bridget Bertoni

A dissertation
submitted in partial fulfillment of the
requirements for the degree of

Doctor of Philosophy

University of Washington

2015

Reading Committee:

Ann Nelson, Chair

Sanjay Reddy

Tom Quinn

Program Authorized to Offer Degree:
Physics

University of Washington

Abstract

Dark Matter Particle Astrophysics: How Dark Matter Can Affect Subhalos, Neutrinos, and Neutron Stars

Bridget Bertoni

Chair of the Supervisory Committee:
Professor Ann Nelson
Physics

Predicted almost a century ago, dark matter explains many astrophysical observations including the motion of matter on galaxy and galaxy cluster scales, the clustering of galaxies, and the anisotropies in the cosmic microwave background. The standard cosmological model further predicts that 26% of the universe consists of dark matter, however we have yet to understand how, if at all, dark matter interacts with the rest of the known particles outside of gravity. Though hints of non-gravitational dark matter interactions exist, most experimental and observational searches only place upper limits on the strength of these interactions. In this thesis, we summarize the current knowledge of dark matter and then focus on three different astrophysical probes of non-gravitational dark matter interactions: 1) dark matter annihilation in subhalos, 2) dark matter-neutrino interactions, and 3) dark matter collection in neutron stars.

TABLE OF CONTENTS

Page

List of Figures iii

List of Tables v

Chapter 1: Introduction 1
1.1 Evidence for Dark Matter 1
1.2 ΛCDM 6
1.3 Dark Matter Candidates 12
1.4 Dark Matter Searches and Constraints 14
1.5 Prelude to the Following Chapters 25

Chapter 2: Dark Matter Annihilations in Subhalos 26
2.1 Introduction 26
2.2 Gamma-Rays From Nearby Dark Matter Subhalos 28
2.3 Unidentified Sources In the 3FGL Catalog 31
2.4 Fermi Data Analysis 33
2.5 Spatial Extension 39
2.6 Implications of 3FGL J2212.5+0703 as a Dark Matter Subhalo 50
2.7 Constraining the Dark Matter Annihilation Cross Section 52
2.8 Summary and Prospects 55

Chapter 3: Neutrino Interacting Dark Matter 58
3.1 Introduction 58
3.2 The Dark Matter Model 61
3.3 Solving the Missing Satellites Problem 79
3.4 Implications for Supernovae 85
3.5 Future tests 90

3.6 Summary and Prospects 93

Chapter 4: Dark Matter in Neutron Stars 95
4.1 Introduction 95
4.2 Dark Matter Model 98
4.3 Light Mixed Sneutrino Dark Matter 99
4.4 Thermalization Time Calculation and Results 102
4.5 Summary 120

Chapter 5: Conclusions 122

Bibliography 123

LIST OF FIGURES

Figure Number		Page
1.1	Evidence for dark matter in the flat rotation curve for Andromeda	2
1.2	The temperature fluctuations in the CMB as measured by the Planck satellite.	5
1.3	Images of the Bullet cluster.	6
1.4	Collider and direct detection limits on the dark matter-nucleon cross section.	16
1.5	Recent direct detection results.	19
1.6	Limits and preferred regions for the dark matter annihilation cross section as a function of dark matter mass.	23
1.7	Constraints on the dark matter - proton spin dependent cross section from solar neutrinos	24
2.1	Number of dark matter subhalos predicted to be bright gamma-ray sources as a function of dark matter mass and cross section	30
2.2	Distribution of variability and latitude observed among the 3FGL unassociated sources.	32
2.3	Gamma-ray spectra from bright, non-variable, unassociated 3FGL sources outside of the Galactic Plane that are well-fit to dark matter annihilation to $b\bar{b}$.	35
2.3	(Cont.)	36
2.4	Same as fig. 2.3, but for sources that are *not* well-fit by dark matter annihilating to $b\bar{b}$.	37
2.5	The distribution in galactic latitude and best-fit dark matter mass for those bright, non-variable, unassociated 3FGL sources located outside of the Galactic Plane.	38
2.6	The change in the test statistic (TS) as a function of spatial extension for the 14 bright, high-latitude subhalo candidate sources considered in our study.	43
2.7	The spectrum of J2212.5+0703, compared to that predicted from a 34 GeV dark matter particle annihilating to $b\bar{b}$.	45
2.8	Residual maps of the region surrounding the dark matter subhalo candidate 3FGL J2212.5+0703.	46

2.9 Residual maps of the region surrounding the point-like Fermi source 3FGL J1119.9-2204. 46
2.10 The change in the test statistic (TS) as a function of spatial extension for a selection of the 252 associated, bright, high-latitude Fermi sources. 48
2.11 Residual maps of the region surrounding the AGN-associated Fermi source 3FGL J0455.7-4617. 49
2.12 Favored regions of mass, distance, and angular extension from 3FGL J2212.5+0703, given its observed flux. 52
2.13 Weighted number of potential dark matter halo sources amoung the 3FGL unassociated sources and the corresponding constraint on the dark matter annihilation cross section. 53
2.14 Constraints on the dark matter annihilation cross section from searching for dark matter annihilations into gamma-rays in potential dark matter subhalos (i.e. unassociated Fermi sources). 55

3.1 Diagram relevant for neutrino scattering on dark matter and for dark matter annihilation to neutrinos. 65
3.2 90% C. L. upper limits on $|U_{\ell 4}|^2$, $\ell = e, \mu, \tau$, as functions of the heavy neutrino mass m_4. 68
3.3 Left: one loop diagram which gives rise to an effective χ-$\bar{\chi}$-Z coupling. Right: diagram that contributes to the $|\phi|^2 |H|^2$ operator. 77
3.4 Allowed values for dark matter mass, mediator mass, and dark matter-neutrino coupling which can alleviate the missing satellites problem. 84

4.1 Kinematically allowed regions for dark matter-neutron scattering. 109
4.2 Thermalization time constraints on the dark matter-neutron cross section from dark matter interacting with a Fermi gas of neutrons in a neutron star. . . . 110
4.3 Comparison of effective suppression factors in the dark matter-neutron scattering rate for dark matter scattering off a non-interacting Fermi gas of neutrons. 112
4.4 Plot of dark matter and neutron superfluid kinematically allowed scattering regions. 115
4.5 Plot of regions of dark matter-electron and dark matter-neutron scattering cross sections and dark matter mass which give rise to dark matter thermalization times longer than 10^{10} years. 117
4.6 Scattering processes which contribute to dark matter thermalization inside a neutron star (i.e. electron, neutron, and phonon processes). 119

LIST OF TABLES

Table Number Page

1.1 Effective operators for dark matter coupling to quarks and gluons. 15

2.1 A list of Fermi's most promising dark matter subhalo candidates. 39

2.2 The results of our test for spatial extension for the 14 bright and high-latitude dark matter subhalo candidates with three extension models. 44

ACKNOWLEDGMENTS

I am very grateful to my advisors, Ann Nelson and Sanjay Reddy. Ann showed me the value of choosing projects that are both interesting and relevant and helped me transition from a being a student to a researcher. I thank Sanjay for emphasizing the importance of simple estimates and analytic approximations, and for sharing his excitement about physics. I also am grateful for the five months I spent learning astrophysics and working with Dan Hooper and Tim Linden at Fermilab.

I owe a great debt to the many other students and postdocs that I learned from along the way—David McKeen, Max Hansen, Jakub Scholtz, John Fuini, Han Chih-Chang, Yu-Sheng Liu, Seyda Ipek, and Akshay Ghalsasi. I will certainly miss the ability to walk into one of their offices to ask them random physics questions.

Members of the astronomy department as well have helped me a greal deal. In particular, I have had many valuable discussions with Tom Quinn, Fabio Governato, and Alex Fry. I am especially grateful to Tom Quinn for his careful reading of my thesis. I also want to thank the particle theory and nuclear theory groups for each taking me on as an extra half of a student. I have benefited greatly from my multidisciplinary education. I am happy I spent my time at the University of Washington and had the opportunity to learn from many other wise professors: David Kaplan, Larry Yaffe, Andreas Karch, Steve Sharpe, and Steve Ellis.

Finally, I particularly want to thank my incredible friend, John, for his support and encouragement throughout my graduate school experience.

Chapter 1

INTRODUCTION

1.1 Evidence for Dark Matter

The first work concerning dark matter began in the early 1900's when the first attempts to estimate the total mass density near the Sun, using stellar motions perpendicular to the galactic plane, began. (For a thorough history of dark matter see [1,2].) The results of these efforts varied, concluding that the amount of dark matter in our solar neighborhood was consistent with 0–2 times the amount of visible matter. It has since been confirmed that there is no significant amount of dark matter ($< 15\%$ of the total mass) in the local galactic disk [3–6].

It was not until the 1933 work of Fritz Zwicky [7] that the first real evidence for dark matter surfaced. Zwicky measured redshifts of galaxies in the Coma cluster and found that the velocities of the galaxies with respect to the cluster velocity were too large for the cluster to remain gravitationally bound. In order for the cluster to remain bound it needed to have an amount of dark matter equal to roughly ten times the amount of visible matter.

In the following decades, many other "missing mass" discrepancies were observed, including a novel measurement of the mass of the combined Milky Way-Andromeda binary system using the motion of Andromeda relative to us [8], which predicted roughly 6 times more mass than previous estimates (in which for example, for the mass of the Milky Way, only employed measurements of the rotational velocities of stars and gas from in the inner ~ 8 kpc [9]). It was also observed that the rotation curves for galaxies became flat at large radii instead of decreasing with the radius r as $r^{-1/2}$ as predicted by applying Newtonian physics to the mass of the observed light distribution (and using known mass to light ratios of galactic stellar populations), see fig. 1.1. This resulted in very large mass to light ratios observed

in the outer regions of the spiral galaxy Andromeda (M31) [10] and in the S0 galaxy NGC 3115 [11]. Light curves for spiral galaxies were measured with much higher accuracy in the 1970's, confirming a flat light curve for M31 [12, 13], M81 [14], and many others [15–17].

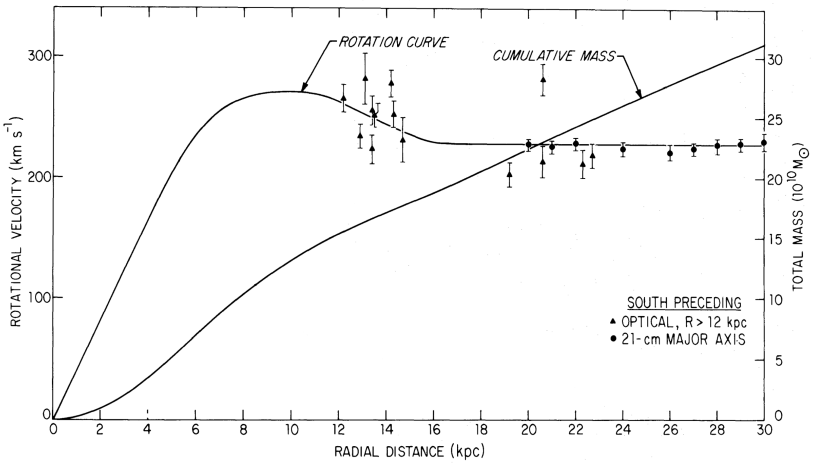

Figure 1.1: Flat rotation curve for Andromeda, showing the need for a large amount of mass far away from the center of the galaxy. Figure adapted from [13].

By the late 1970's, it was known that one way to rectify the flat rotation curve data with the observed mass to light ratios of known stellar populations was to hypothesize the presence of a large, spherical halo of unknown, dissipationless content with a very large mass to light ratio (i.e. dark matter). It was understood that the dark matter had to be a new type of matter for several reasons. If the dark matter halos were made up of regular *ionized* gas, then its thermal bremsstrahlung should be observable [18, 19]. On the other hand, if they were made up of regular neutral gas, then hot intergalactic ionized gas would ionize it, making it observable [20]. It was also hypothesized that the dark matter consisted of old dark stars, but extrapolations of star formation, mass to light ratios and stellar ejecta do not produce enough dark matter (without also producing a lot of visible matter) to explain the discrepancies [19]. Searches for microlensing due to these dark objects (called MACHOs for massive astrophysical compact halo objects) were carried out much later, conservatively restricting their contribution to dark matter to be at most around 20% [21,22] for objects with

mass between $10^{-6}M_{\odot}$ and $10M_{\odot}$ where $M_{\odot}$ is the mass of the Sun. Additionally the amount of baryonic (neutron and proton) matter in the universe was known from measurements of the primordial light element abundances; however, if these baryons made up the majority of matter, then one would expect to see fluctuations on the order of 10^{-3} in the cosmic microwave background (CMB) radiation, through by this time, it was clear that any CMB flutations would be on a much smaller scale [23].

In the early 1980's it was proposed that the dark matter could be composed of the only massive, stable, electrically neutral, non-baryonic particle known, the neutrino [24,25]. However this scenario was soon ruled out as neutrinos were too relativistic in the early universe to be sufficiently drawn into gravitational potential wells, and so they could not provide enough structure formation to match what was observed in galaxy surveys (unless structure formation occurred via fragmentation, but this was inconsistent with early simulations of non-linear structure formation [26], and observations of supercluster and galaxy ages and their dark matter content estimates [27]). Hence the dark matter must be due to some new, weakly-interacting, non-baryonic particle that was very non-relativistic, or "cold" during the early universe [27].

However this cold dark matter solution to these astrophysical and cosmological observations had its competitors, most notably modified Newtonian dynamics (MOND), which was suggested in 1983 [28, 29]. MOND was designed to explain the large velocities of stars on the outskirts of galaxies the created flat galaxy rotation curves. It did this by altering Newton's law such that for objects experiencing very small accelerations, the gravitational force becomes proportional to the square of the acceleration, i.e. $F_g = GMm/r^2 = ma^2/a_0$ where $a_0 \approx 10^{-10}$ m/s^2 is a constant that gets fit to the data. MOND was successful at explaining the flat galactic rotation curves, and as a nice side effect, it naturally explained the Tully-Fisher relation (in the dark matter picture, this is an empirical relation that the visible mass of a disk galaxy is proportional to the asymptotic rotational velocity of the galaxy to the fourth power) and the anti-correlation between the surface brightness of a galaxy and the dark matter content [30]. However MOND was also unsatisfactory on many accounts.

MOND was great at explaining observations of galaxies, but it failed for galaxy clusters [31] and globular clusters (which have only a small amount of dark matter) [32]. MOND was also just an empirical theory that had no relativistic formulation analogous to general relativity, meaning that it could not be tested by measurements of gravitational lensing, gravitational waves, or cosmology, where a relativistic formulation is required.

In the following years a relativistic formulation of MOND, known as Tensor-Vector-Scalar Gravity (TeVeS), was proposed which incorporated all of the successes of MOND, but also could explain gravitational lensing observations [33]. It was also confirmed that TeVeS could well reproduce CMB and galaxy distribution observations so long as dark energy and a large contribution to the energy density from neutrinos is included [34]. However, TeVeS could not reproduce the height of the third peak the CMB temperature power spectrum as well as the standard theory of general relativity with dark matter and dark energy.

The height of the third peak relative to the second peak is an important probe of the amount of dark matter: the CMB power spectrum is an imprint of the acoustic oscillations in the hot, coupled plasma of the early universe in the cosmic photons, just before the photons decoupled. The oscillations occur due to the competing forces of gravity and pressure in the coupled photon-baryon fluid. The peaks in the power spectrum correspond to resonances in which the photons decouple from the plasma when its acoustic oscillation is at its largest over- or under-density. The peaks in the power spectrum are expected to decrease in size as the angular scale decreases since the imprint of these acoustic oscillations gets erased by the scattering of the relativistic particles in the plasma. If dark matter is present, it will only couple to the rest of the plasma via gravity, so as the plasma oscillates between over- and under-dense regions, the dark matter simply continues to collect in over-dense regions. This enhances the amplitude of the plasma oscillation into the over-dense regions, which in turn enhances the amplitude of the odd-numbered peaks in the CMB power spectrum (the even numbered peaks correspond to the photons decoupling from under-dense regions). In the dark matter picture, this is what explains why the height of the third peak in the power spectrum is roughly equal to the height of the second peak, see fig. 1.2. This is a signature

of the presence of some weakly-coupled, gravitationally-interacting particle that is different from ordinary matter and this is hard to reproduce by simply modifying gravity.

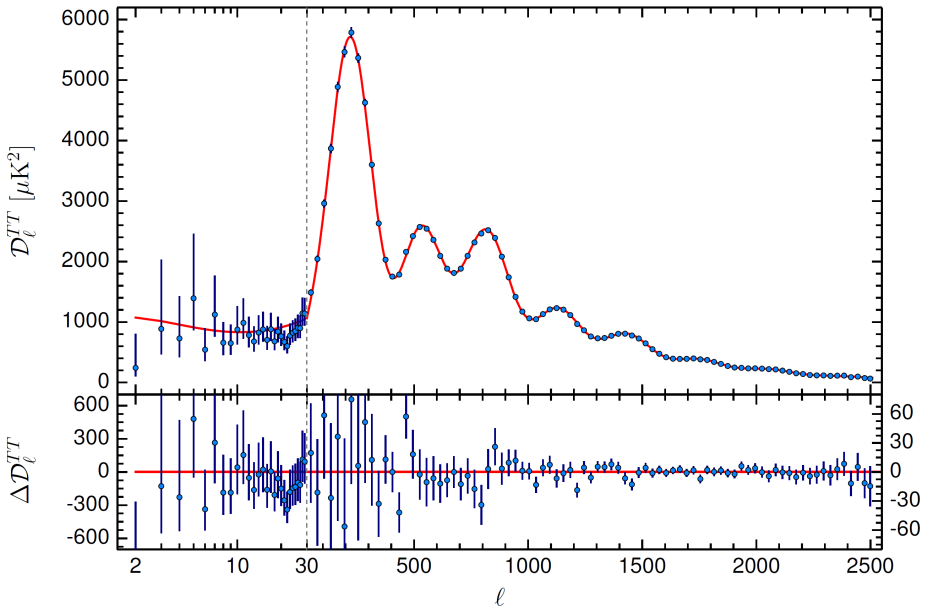

Figure 1.2: The temperature fluctuations in the CMB as a function of angular scale on the sky as measured by the Planck satellite. Notice the approximately equal heights of the second and third peaks—a "smoking gun" signature of dark matter. Figure from [35].

In the early 2000's the gravitational lensing observations of the Bullet cluster appeared [36], see fig. 1.3. The Bullet cluster consisted of two galaxies clusters that had collided. The hot gas (which makes up most of the regular matter of galaxy clusters) surrounding the galaxies in each cluster collided and heated up, releasing x-rays, and making it visible. The spatially separated galaxies passed through the collision region unhindered. The lensing observations revealed that most of the matter, as seen by its gravitational effects, was centered around the two galaxy clusters that had passed through each other, and not around the majority of the visible mass in the hot gas which was stalled by the collision. This 8σ observation that the center of mass did not agree with the center of the visible matter was not something that could be reproduced by TeVeS, or any modification of gravity (without adding dark matter) in which these two centers must agree. The Bullet cluster, like the height of the third CMB peak, was strong evidence in favor of dark matter.

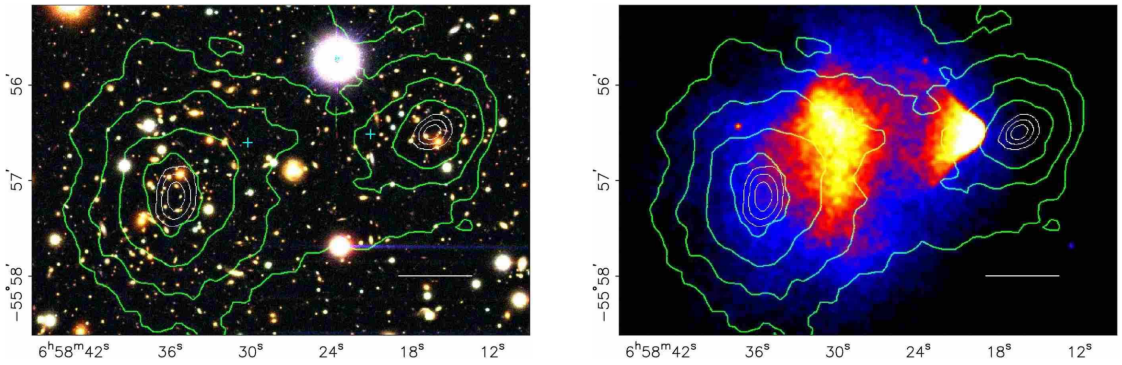

Figure 1.3: Optical image from Magellan (left) and x-ray image from Chandra (right) of the the galaxy cluster 1E 0657-56, the "Bullet cluster." The green contours map out the mass distribution as measured by weak lensing. From the left image one can see that the galaxies and stars in each cluster have passed through the other cluster, whereas from the right image one can see that the hot gas (which makes up most of the mass of the regular matter) from the clusters has collided and slowed down, producing x-rays. The lensing contours show that the majority of the mass in the clusters has followed the path of the galaxies—this is due to the presence of dark matter which also passes through the collision region unhindered. Figure from [36].

Since the Bullet cluster observation, there have been many further observations that strengthen the evidence for dark matter. The Planck satellite [35] has measured the CMB temperature power spectrum to incredible accuracy, including the enhanced height of the third peak. Multiple surveys of large scale structure have been conducted that also observe evidence for baryon acoustic oscillations in the clustering of galaxies and confirm the need for dark matter in the formation of structure, e.g. [37]. Many other colliding galaxy clusters similar to the Bullet Cluster have also been observed [38] which combine to give 7.6σ evidence for dark matter. The evidence for gravitationally-interacting dark matter is now overwhelming and this has helped us to build a more complete model for our universe, known as the ΛCDM model, which has passed many experimental tests.

1.2 ΛCDM

The standard cosmological model today is known as ΛCDM. It consists of general relativity, homogeneity, isotropy, and flatness on large scales due to an early period of inflation of scale-

free, adiabatic primordial fluctuations, dark energy (Λ), cold dark matter (CDM), and the low-energy elementary particle content of the standard model of particle physics (electrons, protons, neutrons, neutrinos, photons, and their interactions).

The assumption that the universe is homogeneous and isotropic on large enough scales leads to a unique prediction for the spacetime metric (known as the Friedmann-Robertson-Walker metric, or FRW metric) given by

$$ds^2 = dt^2 - a(t)^2 \left(\frac{r^2}{1 - kr^2} + r^2 d\Omega \right) \ , \tag{1.1}$$

in spherical coordinates, where $a(t)$ is the time-dependent scale factor and k is the curvature constant. $k = 1$ for a positively curved space, -1 for a negatively curved space, and 0 for a flat space. Here, and throughout all equations are in natural units in which $c = \hbar = k_B = 1$. [1] Einstein's equations for this metric responding to a homogeneous and isotropic energy-momentum tensor (with total energy density ρ and total pressure P) give rise to the Friedmann equations

$$\dot{a}^2 + k = \frac{8\pi\rho a^2}{3M_{\rm Pl}^2} \ , \tag{1.2}$$

$$\dot{\rho} = -\frac{3\dot{a}}{a}(\rho + P) \ , \tag{1.3}$$

where dots denote time derivatives, and $M_{\rm Pl} = 1.22 \times 10^{19}$ GeV is the Planck mass.

The critical density is defined as the density which solves (1.2) for the case of a flat universe with $k = 0$:

$$\rho_{\rm crit} = \frac{3M_{\rm Pl}^2 H^2}{8\pi} \ , \tag{1.4}$$

where $H = \dot{a}/a$ is known as the Hubble parameter. The total energy density ρ consists of five components, the baryon (in this context, regular matter) energy density, the cold dark matter energy density, the dark energy density, and the curvature density. When these

[1] Note that conventionally the numerical value for the dark matter annihilation cross section $\langle \sigma v \rangle$ utilizes $c = 3 \times 10^8$ m/s which should be clear from its stated units of cm^3/s.

energy densities are divided by the critical energy density, they are denoted by Ω. The most recent measurements (incorporating data from the CMB power spectrum, lensing, baryon acoustic oscillations, polarization, and supernovae) of these parameters from Planck [35] with 68% confidence levels (95% for Ω_k) are

$$\Omega_b h^2 = 0.02230 \pm 0.00014 \ , \tag{1.5}$$

$$\Omega_c h^2 = 0.1188 \pm 0.0010 \ , \tag{1.6}$$

$$\Omega_\Lambda = 0.6911 \pm 0.0062 \ , \tag{1.7}$$

$$\Omega_k = 0.0008^{+0.0040}_{-0.0039} \ . \tag{1.8}$$

Here $h = H_0/(100 \text{ km Mpc}^{-1} \text{ s}^{-1}) = 0.6774 \pm 0.0046$ is the reduced Hubble parameter today. This tells us that the universe is essentially flat, with about 5% regular matter, 26% cold dark matter, 69% dark energy.

Additionally this model contains two inflationary parameters, the assumed to be constant scalar spectral index n_s and the curvature fluctuation amplitude A_s, both of which describe the primordial perturbations via the dimensionless curvature power spectrum (i.e. the actual power spectrum, multiplied by $2\pi^2/k^3$) given by

$$P(k) = A_s \left(\frac{k}{k_0} \right)^{n_s - 1} \ , \tag{1.9}$$

where k is wavenumber and $k_0 = 0.05 \text{ Mpc}^{-1}$ is the chosen pivot scale. This power spectrum describes the initial scalar perturbations to the metric and the energy density. The final parameter in the model is the reionization optical depth τ, which describes the effect of CMB photons Thomson scattering off of reionized electrons after the photons decouple from

the plasma. These parameters are measured (with 68% confidence levels) to be [35]

$$n_s = 0.9667 \pm 0.0040 \ , \tag{1.10}$$

$$\log(10^{10} A_s) = 3.064 \pm 0.023 \ , \tag{1.11}$$

$$\tau = 0.066 \pm 0.012 \ . \tag{1.12}$$

As $n_s \approx 1$, the dimensionless curvature power spectrum is essentially scale-free. The small value for τ indicates that Thompson scattering does not damp the features in the CMB power spectrum too much.

The ΛCDM model has passed countless tests. It explains the existence and structure of the CMB, the large scale structure of the Universe measured in galaxy surveys and in the Lyman-alpha forest, gravitational lensing, the light element abundances, and the accelerated expansion of the universe. However, despite all of its successes, there are still many pieces that are unexplained. These include the precise mechanisms for inflation and baryogenesis, an understanding of the cosmological constant and its value, and the empirical relationships that MOND can explain (i.e. the Tully-Fisher relation, the mass transition in galaxies from baryon-dominated to dark matter-dominated at $v_c^2/r \approx a_0$, etc.). In addition, there are some aspects of the ΛCDM model which appear to be in conflict with observations. In the next few paragraphs we summarize several of the well known controversies with the ΛCDM model.

The ΛCDM model does not predict the correct abundance for Lithium (for a review see [39, 40]). The predicted relic abundance for Lithium exceeds the values of the Lithium abundance inferred from observations of metal-poor stars in the galaxy by a factor of $\sim$ 3–4 (a highly significant discrepancy). Lithium is produced along with Deuterium and Helium during Big Bang Nucleosynthesis (BBN) at temperatures around an MeV. The production of these light elements in ΛCDM (with 3 neutrinos) depends only on one free parameter, the

baryon to photon ratio defined by

$$\eta = \frac{n_b}{n_\gamma} = \left(\frac{3 \cdot 10^4 M_{\rm Pl}^2 \Omega_b h^2}{8\pi m_N}\right) \Bigg/ \left(\frac{2\zeta(3) T_0^3}{\pi^2}\right) = 2.72 \times 10^{-8}\ \Omega_b h^2 = \ 6.07 \times 10^{-10}\ , \quad (1.13)$$

where m_N is the nucleon mass and T_0 is the temperature of CMB photons today. Given η, the number densities of neutrons, protons, and nuclei (assuming equilibrium of their nuclear reactions) can be calculated as a function of temperature.

The primordial abundances of light elements are difficult to extract today since after BBN other stellar nucleosynthesis process have occurred which produce and destroy light elements. Because of this, the most metal-poor systems are studied in order to extract the primordial light element abundances. The primordial Lithium-7 abundance is measured in the atmospheres of metal-poor halo stars where it has been verified that the Lithium abundance does not correlate with the Iron abundance (and hence does not correlate with stellar nucleosynthesis). The Lithium-7 to Hydrogen ratio is observed to be $\sim 1 - 2 \times 10^{-10}$ (ref. [41] found ^{7}Li/H $= 1.23^{+0.68}_{-0.32} \times 10^{-10}$, whereas more recently ref. [42] found ^{7}Li/H $= 1.58 \pm 0.31 \times 10^{-10}$). This measured value conflicts with the value predicted using the η as measured by Planck of $4.89^{+0.41}_{-0.39} \times 10^{-10}$ [43]. However, the measured values of Deuterium and Helium-3 agree well with the Planck prediction. Many solutions to the Li^7 problem have been suggested, such as ^{7}Li destruction in stars, new resonances in nuclear reactions, or decays of new particles that alter the light element abundances during BBN, but the ^{7}Li problem has yet to be solved conclusively.

Additionally ΛCDM has difficulty describing observed small scale structures. (For general, recent reviews of these small scale structure discrepancies see [44, 45].) One of these discrepancies is titled the "core-cusp problem." This problem arises because simulations of standard cold dark matter predict that the dark matter density profile ρ in a galaxy should form a cusp at the center, $\rho \propto r^{-1}$ [46], whereas observations in some dwarf galaxies indicate that actual dark matter density profiles appear to be more cored, with a constant dark matter density in the center [47]. Recently, some simulations [48–52] and analytic models [53, 54]

that include baryonic feedback from supernovae on the dark matter indicate that this can flatten the cusps of dark matter near the centers of galaxies, hence solving the core vs. cusp problem. However, it has also been suggested that supernova feedback may be too strong in some cases [55, 56].

Simulations based on cold dark matter also predict that there should be hundreds of dark matter subhalos in a Milky Way-sized galaxy [57, 58], in contrast to the few dozen known Milky Way satellite galaxies (for a review see [59]). When the observed number of Milky Way satellite galaxies is corrected for the incompleteness of surveys, it is possible to reconcile these numbers, however this needs to be confirmed observationally and the number of currently undetectably faint satellite galaxies is still very uncertain [60]. This discrepancy is termed the "missing satellites" problem. The apparent deficit in the number of satellite galaxies could be due to conventional astrophysics, such as the inability of low mass dark matter subhalos to form stars (for example, due to supernova feedback or reionization blowing regular matter out of smaller subhalos), making them hard to detect (see [61] and references therein).

Another small scale structure problem is the “too big to fail problem.” This problem arises from simulations predicting that the most massive Milky Way satellite galaxies should be more massive than they are observed to be. Supernova feedback has been shown to reduce the dark matter density in the center of galaxies, and this helps alleviate the too big to fail problem [62]. In ref. [52], N-body simulations including supernova feedback showed that indeed the too big to fail problem could be solved by supernova feedback moving dark matter from the center region of galaxies out to larger radii. However, there is also some evidence that supernova feedback alone may not be sufficient to address the too big to fail problem [55, 63].

Another difficulty that realizations of the ΛCDM model face is the simulation of bulgeless disk galaxies, also known as the angular momentum problem. Early simulations tended to over-predict the amount of low angular momentum gas in a galaxy, resulting in a very centrally concentrated galactic disk with a prominent bulge [64, 65]. On the other hand, galaxy catalogs report that a significant fraction of galaxies are observed to contain flat,

bulgeless disks [66, 67]. Some more recent simulations have shown that this problem can be alleviated by (you guessed it!) baryonic feedback/gas outflows as well as better numerical resolution [48, 68–70].

One additional observational feature of satellite galaxies that is controversial within the ΛCDM model is the detection of planar structures in the satellite galaxies in the Milky Way and Andromeda [71, 72] as opposed to the more uniform distribution predicted by ΛCDM [73, 74]. The satellite galaxies appear to cluster around a single spatial plane of the galaxy and have a common rotation direction. It has also been argued that finding such planar structures is in fact consistent with ΛCDM once a large number of satellite systems have been studied and the look-elsewhere effect has been included [75]. The planar structure could also be due to the galactic accretion of filaments [76].

Finally, some parameters of the ΛCDM model have slightly conflicting values depending on how they are measured. These include the Hubble parameter H_0 and σ_8 (the rms fluctuation in matter in $8h^{-1}$ Mpc spheres at $z = 0$). The value of the Hubble constant as measured using Planck data alone is about 1–2σ smaller than that measured using supernovae [77]. And when using the Sunyaev–Zel'dovich effect to count clusters, Planck finds $\sigma_8 = 0.75 \pm 0.03$ [78], whereas using the Planck CMB measurements, $\sigma_8 = 0.8150 \pm 0.0087$ [35], another $\sim 2\sigma$ discrepancy. These measurements could be just statistical fluctuations, or they could be hinting at new or missed physics beyond ΛCDM.

1.3 Dark Matter Candidates

Altering dark matter properties away from the conventional cold, solely gravitationally-interacting dark matter of ΛCDM can help to alleviate some of the problems with ΛCDM. For example, axions have been invoked to solve the ^{7}Li primordial abundance problem [79]. The small scale structure problems can be mitigated by dark matter that is warm [80, 81], self-interacting [82–85], or dark matter that interacts with other relativistic particles [86–88]. Dark matter that has a self-interacting component can also explain the planar structure of satellite galaxies [89] and warm dark matter might remove the bulges from galaxies [90]. The

most compelling dark matter candidates are able to address other puzzles in particle physics and astrophysics as well. In this section, we review various production mechanisms for dark matter and we end with a short discussion of some of the most popular, well-motivated dark matter candidates. In the following section on dark matter searches and constraints (sec. 1.4), we will consider other astrophysical signatures which can be addressed by non-standard dark matter candidates.

One essential requirement for dark matter models is that the correct relic abundance of dark matter can be produced. Often the production mechanism for the relic abundance is used to characterize dark matter particles. For example, dark matter could be produced thermally in the early universe. In this case, dark matter is kept in equilibrium with other particles in the early universe through non-gravitational interactions. Once the rate for dark matter number-changing interactions becomes small compared to the expansion of the Universe ($H(t)$), the dark matter falls out of equilibrium with the thermal bath, or "freezes out." After the dark matter has frozen out and become non-relativistic, the number of dark matter particles per comoving volume ($\propto a(t)^3$) remains fixed, and must be matched to the observed relic density today. The number density of dark matter particles n_χ (antiparticles are denoted by $n_{\bar{\chi}}$) evolves according to the Boltzmann equation in an expanding Universe (see [91])

$$\dot{n}_\chi + 3Hn_\chi = \frac{d(na^3)}{dt} = -\langle\sigma v\rangle \left(n_\chi n_{\bar{\chi}} - n_\chi^{\rm eq} n_{\bar{\chi}}^{\rm eq}\right) \ , \tag{1.14}$$

where $\langle\sigma v\rangle$ is the thermally averaged dark matter annihilation cross section times the relative velocity and $n^{\rm eq}$ denotes the number density value in equilibrium. Notice that the number of dark matter particles per comoving volume becomes constant at two times: in the early universe when everything is in equilibrium and $n_{\chi,\bar{\chi}} = n_{\chi,\bar{\chi}}^{\rm eq}$, and also once the dark matter freezes out when $\Gamma = n_{\bar{\chi}}\langle\sigma v\rangle << (\text{elapsed time}) \approx H$.

For self-conjugate dark matter particles that are non-relativistic when they freeze out (during radiation domination and in the absence of entropy production), the correct relic abundance of dark matter can be obtained for 10 GeV $< m_\chi <$ 1 TeV and $\langle\sigma v\rangle \approx 3 \times 10^{-26}$

$\text{cm}^3/\text{s} \sim G_F^2 m_\chi^2$ ($G_F = 1.17 \times 10^{-5}$ GeV^{-2}), i.e. a weak-scale dark matter mass and a weak-scale annihilation cross section. This is known as the weakly interacting massive particle (or WIMP) miracle. Many supersymmetric theories contain a new, stable, particle known as the lightest supersymmetric particle or LSP, which is naturally a WIMP dark matter candidate.

Non-thermal production mechanisms for dark matter are also possible. These include production via the "freeze-in" mechanism [92] in which the dark matter interacts so feebly that it never is in thermal equilibrium but is produced via the particles in the thermal bath, the Affleck-Dine / misalignment mechanism [93], or by the decay of other particles which may or may not be in thermal equilibrium. Axions are a non-thermal dark matter candidate produced via the misalignment mechanism that were invented to explain the absence of CP violation in strong interactions (the strong-CP problem). At high temperatures the axion potential is essentially zero and the axion is uncoupled to the rest of the Universe. At late times, an axion mass term is generated nonperturbatively causing the axion field to oscillate coherently in time with frequency m_a (the axion mass). This field configuration can be interpreted as many axion particles at rest, making axions a cold, non-thermal dark matter candidate.

Similar to the axion, other dark matter candidates are motivated by their particle physics properties. For example, if dark matter particles are not self-conjugate, then there could be some initial asymmetry such that $n_\chi \neq n_{\bar{\chi}}$. This type of dark matter is called asymmetric dark matter and it is well-motivated since it can be related to the unexplained baryon asymmetry (one of the major problems in particle physics) and potentially explains why the dark matter abundance is similar to the baryon abundance. Another popular dark matter candidate is the sterile neutrino, which in addition to being dark matter, can also be the explanation for neutrino masses.

1.4 Dark Matter Searches and Constraints

There are many well-motivated dark matter candidates which have non-gravitational interactions, making them experimentally accessible. Over the past decades there has been an

extensive search for potential non-gravitational interactions of dark matter. These searches are typically classified into three classes: collider searches, direct detection searches, and indirect detection searches. We briefly discuss each in turn.

1.4.1 Collider Searches

If dark matter couples to other particles in the standard model and is less massive than a few TeV, then dark matter may be produced at colliders and detected as missing transverse energy. If the dark matter is produced back-to-back with other observable particles (like a photon, gluon, Z, or $W^{\pm}$), then these types of events (mono-photon, mono-jet, mono-Z/dilepton or jets, or mono-W/mono-lepton or jet) can be tagged and studied. These events are typically used to set limits on dark matter interactions using an effective field theory (EFT) approach in which the particles that mediate the interactions between dark matter and regular matter have a mass much larger than the momentum exchange in the processes and can be integrated out. Examples of such dark matter interactions are in tab. 1.1.

Name	Operator	Name	Operator	Name	Operator
M1	$m_q\bar{\chi}\chi\bar{q}q/2M_*^3$	D3	$im_q\,\bar{\chi}\chi\bar{q}\gamma_5 q/M_*^3$	D14	$\alpha_s\,\bar{\chi}\gamma_5\chi G_{\mu\nu}\tilde{G}^{\mu\nu}/4M_*^3$
M2	$im_q\bar{\chi}\gamma_5\chi\bar{q}q/2M_*^3$	D4	$m_q\,\bar{\chi}\gamma_5\chi\bar{q}\gamma_5 q/M_*^3$	C1	$m_q\,\chi^\dagger\chi\bar{q}q/M_*^2$
M3	$im_q\bar{\chi}\chi\bar{q}\gamma_5 q/2M_*^3$	D5	$\bar{\chi}\gamma^\mu\chi\bar{q}\gamma_\mu q/M_*^2$	C2	$im_q\,\chi^\dagger\chi\bar{q}\gamma_5 q/M_*^2$
M4	$m_q\bar{\chi}\gamma_5\chi\bar{q}\gamma_5 q/2M_*^3$	D6	$\bar{\chi}\gamma^\mu\gamma_5\chi\bar{q}\gamma_\mu q/M_*^2$	C3	$\chi^\dagger\partial_\mu\chi\bar{q}\gamma^\mu q/M_*^2$
M5	$\bar{\chi}\gamma_5\gamma_\mu\chi\bar{q}\gamma^\mu q/2M_*^2$	D7	$\bar{\chi}\gamma^\mu\chi\bar{q}\gamma_\mu\gamma_5 q/M_*^2$	C4	$\chi^\dagger\partial_\mu\chi\bar{q}\gamma^\mu\gamma_5 q/M_*^2$
M6	$\bar{\chi}\gamma_5\gamma_\mu\chi\bar{q}\gamma_5\gamma^\mu/2M_*^2$	D8	$\bar{\chi}\gamma^\mu\gamma_5\chi\bar{q}\gamma_\mu\gamma_5 q/M_*^2$	C5	$\alpha_s\,\chi^\dagger\chi G_{\mu\nu}G^{\mu\nu}/4M_*^2$
M7	$\alpha_s\bar{\chi}\chi G_{\mu\nu}G^{\mu\nu}/8M_*^3$	D9	$\bar{\chi}\sigma^{\mu\nu}\chi\bar{q}\sigma_{\mu\nu}q/M_*^2$	C6	$i\alpha_s\,\chi^\dagger\chi G_{\mu\nu}\tilde{G}^{\mu\nu}/4M_*^2$
M8	$i\alpha_s\bar{\chi}\gamma_5\chi G_{\mu\nu}G^{\mu\nu}/8M_*^3$	D10	$i\,\bar{\chi}\sigma_{\mu\nu}\gamma_5\chi\bar{q}\sigma_{\alpha\beta}q/M_*^2$	R1	$m_q\,\chi^2\bar{q}q/2M_*^2$
M9	$\alpha_s\bar{\chi}\chi G_{\mu\nu}\tilde{G}^{\mu\nu}/8M_*^3$	D11	$\alpha_s\,\bar{\chi}\chi G_{\mu\nu}G^{\mu\nu}/4M_*^3$	R2	$im_q\chi^2\bar{q}\gamma_5 q/2M_*^2$
M10	$i\alpha_s\bar{\chi}\gamma_5\chi G_{\mu\nu}\tilde{G}^{\mu\nu}/8M_*^3$	D12	$i\alpha_s\,\bar{\chi}\gamma_5\chi G_{\mu\nu}G^{\mu\nu}/4M_*^3$	R3	$\alpha_s\,\chi^2 G_{\mu\nu}G^{\mu\nu}/8M_*^2$
D1	$m_q\,\bar{\chi}\chi\bar{q}q/M_*^3$	D13	$i\alpha_s\,\bar{\chi}\chi G_{\mu\nu}\tilde{G}^{\mu\nu}/4M_*^3$	R4	$i\alpha_s\,\chi^2 G_{\mu\nu}\tilde{G}^{\mu\nu}/8M_*^2$
D2	$im_q\,\bar{\chi}\gamma_5\chi\bar{q}q/M_*^3$				

Table 1.1: Effective operators for standard model singlet dark matter χ (which is odd under a Z_2 symmetry) coupling to quarks and gluons, excluding higher order terms with derivatives acting on the quark or gluon fields. In the naming convention, M, D, C, and R stand for Majorana fermion, Dirac fermion, complex scalar, and real scalar dark matter, respectively. α_s is the strong coupling constant. Table from [94, 95].

Collider searches are used to place a lower limit the value of M_*[2] (see tab. 1.1) which can then be translated into an upper limit on the corresponding cross section. An example of cross section limits using the Dirac fermion dark matter operators $D5$ (spin-independent) and $D8$ (spin-dependent) from various collider experiments is shown in fig. 1.4.

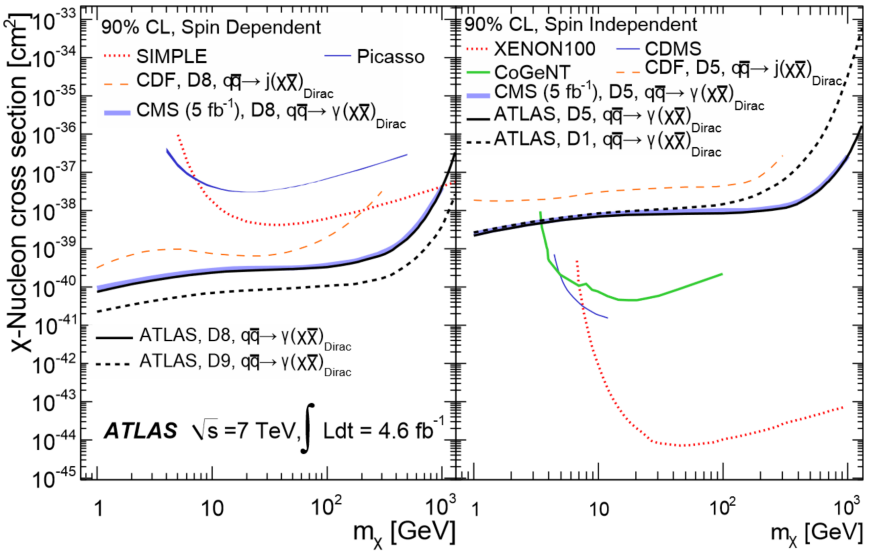

Figure 1.4: 90% confidence level upper limits on the dark matter-nucleon cross section for Dirac fermion dark matter from a mono-photon search from ATLAS [96], a mono-jet search at CDF [97], a mono-photon search at CMS [98], and direct detection searches which are discussed more in detail in sec. 1.4.2. Figure from [96].

Collider searches are valuable because they involve none of the astrophysical uncertainties that affect direct and indirect searches and they can constrain dark matter masses $\lesssim 10$ GeV, however even if a signal is discovered at a collider, it may be due to another new particle, not necessarily dark matter. The EFT approach is also limited because it does not allow for light mediators (which can lead to much weaker cross sections and less stringent constraints at transverse energies E_{t} above the mediator mass M since there $\sigma \propto 1/E_{\mathrm{t}}^2$ as opposed to $\sigma \propto 1/M^2$), interference between different operators, or how the dark matter particle is

[2]If one considers tree-level interactions in which two dark matter particles are coupled to two quarks or gluons by the exchange a mediator of mass M and couplings λ_χ and $\lambda_{q,g}$ respectively, then $M_* \sim M/(\lambda_\chi \lambda_{q,g})$. For perturbation theory to remain valid, λ_χ and $\lambda_{q,g}$ must be $\lesssim 2\pi$, hence the EFT framework is only valid for $M_* \gtrsim M/(4\pi^2)$.

incorporated into a complete theory.

1.4.2 Direct Searches

Direct searches look for evidence of the dark matter particles from the Milky Way halo interacting with nuclei (or electrons, see [99] and references therein) inside an Earth-based detector. This evidence could be phonons, bubble nucleation, or an ionization or scintillation signal. An interesting feature of any detection is that the signal should be annually modulated by a few percent due to the variation in the velocity of the "dark matter wind" on Earth as the Earth rotates about the sun.

In order to calculate the rate of expected dark matter-induced events, the dark matter distribution near the Earth must be known. The average dark matter energy density in the solar vicinity is known to be around $\rho_{DM} \simeq 0.3$ GeV/cm^3 with an error of about ± 0.1 GeV/cm^3 depending on the measurement [5, 6]. In the standard halo model, it is assumed that the dark matter velocity distribution in the reference frame of the Galaxy is a Maxwell-Boltzmann distribution that is truncated above escape velocity. It follows that the dark matter velocity distribution with respect to the Earth is $f_{MB}(\vec{v} + \vec{v}_{ES} + \vec{v}_{SG})$ where $\vec{v}$ is the velocity of the dark matter with respect to the Earth, $\vec{v}_{ES}$ is the velocity of the Earth with respect to the Sun, and $\vec{v}_{SG}$ is the velocity of the Sun with respect to the Galaxy. The dark matter speed with respect to the Earth is $\sim 10^{-3}$. This is a simplified model since the dark matter distribution is not likely to be completely uniform—instead it probably contains over-dense streams or clumps that are remnants of hierarchical structure formation. Additionally, the velocities mentioned above are only known at the 10% level. In order to bypass such astrophysical uncertainties, halo-independent analyses [100, 101] have been developed to compare event rates at different experiments.

When the dark matter particles collide with nuclei in a detector, they impart the nuclei (of mass M) with a maximum recoil energy of $E_{\max} = 2v^2\mu^2/M$ where μ is the reduced mass of the dark matter and the nuclei and elastic, non-relativistic kinematics have been assumed. $E_{\max}$ is around a few keV for typical parameters: $m_\chi \sim$ GeV and $M \sim 100$ GeV (Xenon has

a mass of 120 GeV). The rate of dark matter-nucleus scattering events expected/unit mass of the detector/recoil energy is

$$\frac{dR}{dE_R} = \int_{v_{\min}}^{v_{\max}} d^3v \; n_\chi \frac{d\sigma}{dE_R} v f_{MB}(\vec{v} + \vec{v}_{ES} + \vec{v}_{SG}) \frac{N}{M_{\det}} \; , \tag{1.15}$$

where $v_{\min} = \sqrt{ME_R/2\mu^2}$ is the minimum dark matter speed necessary to make the nucleon recoil with energy E_R, $v_{\max}$ is set by the escape velocity, N is the number of nuclei in the detector, $d\sigma/dE_R$ is the differential dark matter-nuclei cross section, and $M_{\det}$ is the mass of the detector. In addition, the observable rate must incorporate both the detector efficiency and the probability that a recoil energy of E_R is actually measured as E'_R.

Typically dark matter-nucleon interactions are classified into two types: spin-independent scattering (due to scalar or vector couplings) in which the dark matter couples to the nucleon number density, and spin-dependent scattering (due to axial vector couplings) in which the dark matter couples to the nucleon spin density. Because this is often too simple of a classification, an EFT approach towards non-relativistic dark matter-nucleon scattering has also been thoroughly investigated [102]. In order to sufficiently test all types of dark matter interactions, many direct detection experiments using different nuclei are necessary. For example, if all of dark matter were isospin-violating dark matter [103], in which the ratio of dark matter-neutron coupling to dark matter-proton coupling, $f_n/f_p \approx -0.7$, then the coupling of dark matter to Xenon is minimized, and other nuclei would be better at detecting dark matter. Additionally, the dark matter could be multi-component and interact with nucleons via an exothermic reaction in which the dark matter particle prior to the collision is heavier than the final state dark matter particle, enhancing the dark matter collision rate off lighter nuclei [104].

So far, many direct detection experiments such as LUX (Xe), XENON100 (Xe), CDMS-II-Ge, ZEPLIN III (Xe), Edelweiss II (Ge), SIMPLE (C_2ClF_5), and CRESST-II ($CaWO_4$) have seen no evidence for dark matter interactions and have placed upper bounds on strength of the dark matter-nucleon cross section. However, contrary to this, three direct detection

experiments, DAMA/LIBRA (NaI) [105], CoGeNT (Ge) [106], and CDMS-II-Si [107] have observed an excess number of events which can be interpreted as a signal from dark matter. DAMA/LIBRA found a 9.3σ annual modulation in their data that is consistent with dark matter. CoGeNT also observed an annual modulation, but only at the 1.7σ level, and CDMS-II-Si observed 3 excess events. No one type of dark matter has been postulated that is consistent with all of these constraints and potential detections.

Recent direct detection results are shown in fig. 1.5. Notice that the upper limits weaken for low and high mass dark matter. If the dark matter mass is too small, then it does not impart enough energy into the detector when it collides with a nucleus (note $v_{\min} \propto \sqrt{E_R/m_\chi^2}$), making it harder to detect. As the dark matter mass increases, its number density decreases since its energy density is fixed, and this decreases the rate of events given in (1.15).

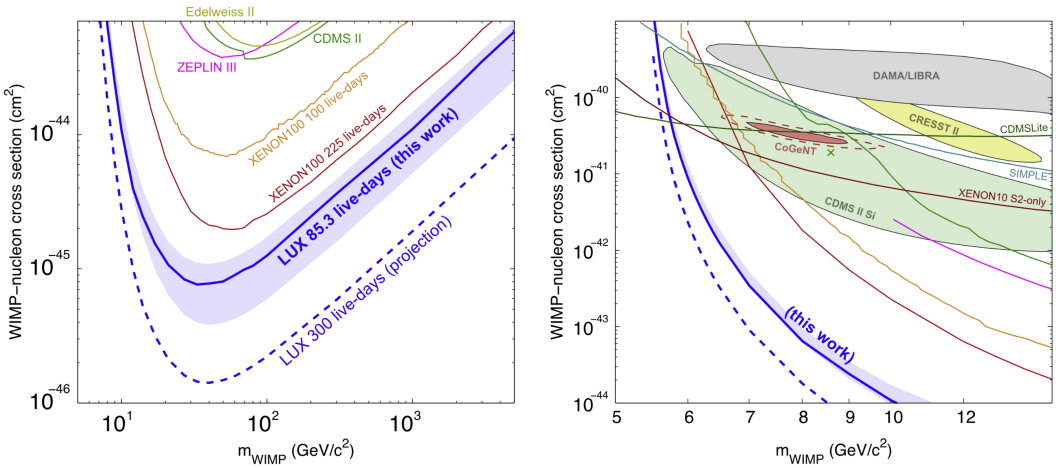

Figure 1.5: Projected 90% confidence level upper limits on the spin-independent dark matter-nucleon scattering cross section for 300 days of LUX data, plotted along with other recent results. Left: results for high mass dark matter and Right: close up on results for low mass dark matter. The preferred regions for CRESST have now been largely ruled out with their upgraded detector run [108]. Figure from [109].

Direct searches are a useful way to probe the interactions of dark matter with regular matter. They are relatively small experiments and they benefit from increased cross sections as light dark matter can scatter from the nucleus coherently (spin-independently), resulting

in a cross section proportional to the number of nucleons in a nucleus squared. However, direct searches suffer from large astrophysical uncertainties in the dark matter density and velocity distribution, uncertainties in the nuclear physics form factors for nucleons and nuclei, and potentially unrecognized systematics.

1.4.3 Indirect Searches and Astrophysical Probes

Indirect searches look for dark matter annihilation and decay products by studying astrophysical photons, neutrinos, and cosmic rays (such as positrons, antiprotons, and antideuterons) which are currently not understood in terms of conventional astrophysics. Additional astrophysical probes of dark matter include stars that have accumulated dark matter which can emit dark matter decay or annihilation products or have their standard stellar process altered by the presence of dark matter.

One common indirect detection search is for a monochromatic "line" photon signal which could be due to dark matter directly annihilating into photons ($\chi\chi \to \gamma\gamma$). The energy of the detected photons would be roughly equal to the dark matter mass. Several such line signals have already been observed. A line at 511 keV was observed coming from the Galactic Center and many dark matter interpretations of the signal were put forward, such as exciting dark matter in which an excited dark matter state decays into its ground state plus an e^+e^- pair which then annihilate into photons [110] or the annihilation of light dark matter, e.g. see [111]. However, in 2008 the INTEGRAL telescope found that the 511 keV signal region was asymmetric about the Galactic Center [112] and resembled the asymmetry seen in low mass x-ray binaries (with hard emission at photon energies > 20 keV), indicating that these binaries may be the origin of the positrons needed to produce the 511 keV line, thus decreasing interest in a dark matter explanation of the signal. There was also an observation of a 130 GeV line by the Fermi Large Area Telescope [113], however this signal strangely appeared in the limb of the Earth and seems likely to be a result of systematics [114]. Additionally, a 3.55 keV line was observed in some galaxy clusters [115–117] (though not in others [117]), Andromeda [116], and possibly in the Galactic Center [118, 119]. Potential explanations

include a 7.1 keV sterile neutrino decaying into a photon and a neutrino [115], dark atomic transitions [120], or potassium emission lines [121].

Another indirect search is for a spectrum of photons which could be due to secondary photons produced from dark matter annihilations or decays. This type of signal should be much larger than a line signal since the dark matter-photon coupling must be small. If the photon spectrum is due to dark matter, then it should fall off for energies larger than the dark matter mass. The differential flux of photons (number/time) dN/dt expected from dark matter annihilations in a volume dV a distance ℓ away is given by

$$\begin{aligned}\frac{dN}{dt} = & \text{ (Number of dark matter annihilations in } dV\text{/time)} \\ & \times \text{ (Number of photons produced per annihilation)} \times \text{(detector area}/4\pi\ell^2\text{)} \\ = & \left(x\frac{1}{2}n_\chi^2\langle\sigma v\rangle dV\right) \times N_\gamma \times \frac{dA_{\rm det}}{4\pi\ell^2} \ , \end{aligned} \tag{1.16}$$

where $n_\chi\langle\sigma v\rangle$ is the interaction rate for a single dark matter particle so muliplying this by $n_\chi dV/2$ (the number of dark matter particles in volume dV divided by 2) gives the total number of annihilations/time, assuming dark matter particles are their own antiparticle ($x = 1$). If the dark matter consists of equal numbers of distinct particles and antiparticles, then $x = 1/2$ since a given particle can only annihilate with $n_\chi dV/2$ other particles, resulting in $n_\chi dV/4$ annihilations/time.

The relevant detectable quantity is the total number of photons/time/detector area/energy/ solid angle, i.e. $\Phi \equiv dN/dt/dA_{\rm det}/dE_\gamma/d\Omega$ given by

$$\Phi = \frac{x}{8\pi m_\chi^2}\langle\sigma v\rangle\frac{dN_\gamma}{dE_\gamma}\int_{\rm los} d\ell\ \rho_\chi^2(\ell,\Omega) \quad \text{(annihilation)} \ , \tag{1.17}$$

where we have used $dV = \ell^2 d\ell d\Omega$, inserted the dark matter energy density $\rho_\chi = m_\chi n_\chi$ in place of the dark matter number density, and the integral is taken along the line of sight. If

the photons are due to dark matter decays rather than annihilations, then Φ becomes

$$\Phi = \frac{1}{4\pi m_\chi \tau} \frac{dN_\gamma}{dE_\gamma} \int_{\text{los}} d\ell \ \rho_\chi(\ell, \Omega) \quad \text{(decay)} \ , \tag{1.18}$$

where τ is the dark matter lifetime. These photon signals interpreted as dark matter are highly dependent on the so-called "J-factor", given by

$$J = \int_{\Delta\Omega} \int_{\text{los}} d\ell d\Omega \ \rho_\chi^2(\ell, \Omega) \ , \tag{1.19}$$

which contains all of the astrophysics information and can be uncertain by as much as a few orders of magnitude [122].

If a photon signal is truly due to dark matter than it should be strongest coming from areas of high dark matter density, such as the Galactic Center, dwarf galaxies, or subhalos. An excess in microwave photon emission around the Galactic Center was observed in WMAP data [123] (and so was possibly due to the synchrotron emission of dark matter decay products [124]), but the excess was discovered to have a gamma-ray counterpart [125] and is now thought to be due to activity of the black hole in the Galactic Center. On the other hand, a robust, spatially extended excess of gamma-ray photons from the Galactic center is observed and explainable by dark matter with a thermal annihilation-scale cross section [126, 127]. However the astrophysical backgrounds in the Galactic Center are considerable and this gamma-ray excess can be potentially attributed to a large population of unresolved pulsars [128, 129] or outbursts of cosmic-ray electrons [130]. Only one dwarf galaxy, Reticulum II, shows an excess of gamma-ray photons. Intrigingly this excess is compatible with the excess from the Galactic Center [131, 132]. (The other dwarf galaxies are typically farther away and have not yet been detected significantly in gamma-rays [133].) A photon signal from subhalos has not been confirmed, but searches for dark matter annihilations in subhalos are ongoing and are the subject of chp. 2 of this thesis. Constraints on the dark matter annihilation cross section into photons are shown in fig. 1.6.

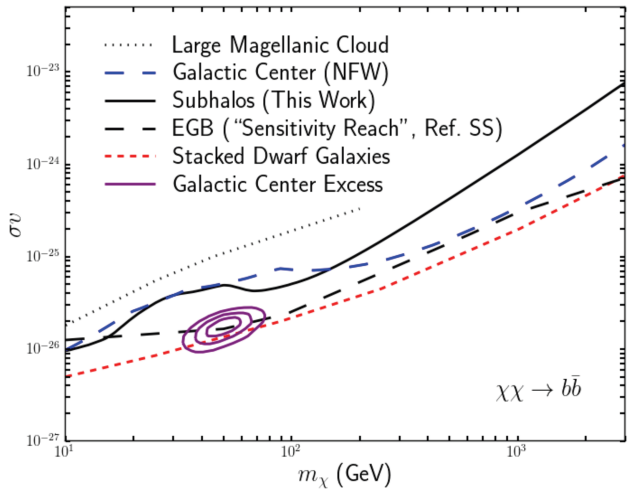

Figure 1.6: A comparison of the limit on $\langle \sigma v \rangle$ derived from subhalos in [134] (see chp. 2 for details) to those derived from gamma-ray observations of dwarf spheroidal galaxies [135], the Galactic Center [136], the extragalactic gamma-ray background [137], and the Large Magellanic Cloud [138]. Also shown is the region of parameter space that is able to account for the gamma-ray excess observed from the region surrounding the Galactic Center [126, 139–144], as presented in refs. [127, 145].

Positrons, antiprotons, and antideuterons can also be produced in dark matter annihilations and decays. Several experiments, including more recently PAMELA [146], the Fermi Large Area Telescope [147], and AMS-02 [148], have found an excess in the positron fraction $e^+/(e^+ + e^-)$ at energies above 10 GeV. However, measurements of antiproton fluxes by PAMELA [149] and AMS-02 [150] are consistent (though a little on the high side) with the secondary production of antiprotons during the propagation of cosmic rays in the Galaxy. Pulsars or supernovae could be the sources of these excess positrons, though leptophilic dark matter could explain the excess as well. Searching for antideuterons as well is advantageous due to their low background flux (especially at low energies, due to the high energy threshold for cosmic ray production of secondary antideuterons) which is expected to be orders of magnitude smaller than benchmark signals from dark matter annihilations or decays [151]. However, any process capable of producing antideuterons should also produce antiprotons, so the non-observation of an antiproton signal limits any prospective antideuteron signal from dark matter.

Additionally if dark matter interacts with regular matter, then it can scatter with particles inside the Earth or the Sun, lose energy, and become bound. The dark matter can then annihilate, potentially producing neutrinos (the only particle that could escape) which then could be observed by neutrino detectors. Typically it is assumed that the annihilation rate is equal to the capture rate and so the expected neutrino rate depends on the dark matter-nucleon scattering cross section, and can be compared to direct detection results. Since the Sun contains mostly hydrogen, the dark matter-nucleon spin-independent cross section does not benefit from coherent scattering. However, the spin-dependent cross section limits from the Sun can be even more stringent then direct detection limits, see fig. 1.7. (Note that the same effect is true for collider experiments which collide only protons and antiprotons, c.f. fig. 1.4)

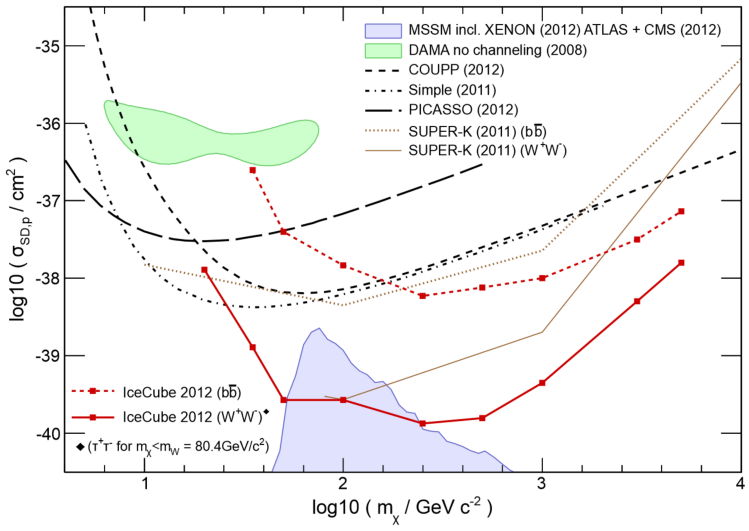

Figure 1.7: 90% confidence level upper limits on the dark matter - proton spin-dependent cross section. Results using solar neutrinos from ICECUBE [152] and Super-K [153] (red and orange) are often more constraining than the direct detection limits (black). Figure from [152].

Constraints on the dark matter annihilation cross section into neutrinos are also placed by looking at the flux of neutrinos from the Galactic Center [154]. Further constraints and consequences of neutrino-interacting dark matter are discussed in chp. 3. Also note that dark

matter can be captured most efficiently not by the Sun or the Earth, but by neutron stars, and its presence there can affect neutron star transport properties and lifetimes. Aspects of dark matter accumulation in neutron stars are examined further in chp. 4.

Indirect searches are an important way to search for signatures of dark matter annihilations, decays, and interactions that gain sensitivity by studying regions of high dark matter density like the Galactic Center, dwarf galaxies, or the inside of stars. In indirect searches, often the dark matter annihilation cross section is constrained, which is directly relevant to understanding thermal relic dark matter (unlike direct detection or collider searches which probe other dark matter cross sections). However these searches are also burdened with often large astrophysical uncertainties associated with estimating the amount and distribution of dark matter in high dark matter density regions and with the production of astrophysical antiparticles.

1.5 Prelude to the Following Chapters

This thesis focuses on three different astrophysical probes of potential non-gravitational interactions of dark matter. In chp. 2 we discuss constraints on dark matter annihilation into photons from galactic subhalos. If dark matter does annihilate into standard model particles, then the only way it would not produce photons in the process would be by annihilating into neutrinos. Hence, in chp. 3 we address the other case of neutrino-interacting dark matter and how it could address some of the small scale structure problems in ΛCDM. In chp. 4 we examine how dark matter capture and thermalization in neutron stars alters neutron star observables. Each chapter ends with a summary and outlook on the topic. A general conclusion is presented in chp. 5.

Chapter 2

DARK MATTER ANNIHILATIONS IN SUBHALOS

This chapter is based on my work with Dan Hooper and Tim Linden in refs. [134, 155].

2.1 Introduction

Numerical simulations reveal that dark matter structures form hierarchically, beginning with the smallest halos, and gradually merging to create ever larger systems, including the halos that host galaxies and galaxy clusters [156]. As a consequence of this process, in the standard cold dark matter scenario, dark matter halos are predicted to contain very large numbers of smaller subhalos. In the case of the Milky Way, the largest members of this subhalo population include the few dozen known dwarf galaxies and the Large and Small Magellanic Clouds. These systems are exceptional, however, and reflect only the very small fraction of subhalos that were large enough to capture significant quantities of gas and form stars. The vast majority of the Milky Way's subhalos harbor no significant quantities of baryonic matter and cannot be detected by optical surveys. If dark matter particles annihilate at a rate similar to that expected of a simple thermal relic, however, the nearest and most massive subhalos could generate an observable flux of gamma-rays, appearing as a population of unidentified gamma-ray sources.

The Fermi Collaboration has recently released a new catalog of gamma-ray sources, known as the Fermi-LAT Third Source Catalog, or 3FGL [157]. Along with many identified objects, this catalog contains 992 sources that have not been associated with emission observed at other wavelengths. These sources almost certainly include many presently unidentified

blazers, pulsars, and other astrophysical objects.[1] If the dark matter consists of annihilating particles with weak-scale masses, however, we should also expect a relatively small number of these unassociated sources to be dark matter subhalos [158, 159]. For example, we estimate that for a 100 GeV dark matter particle with an annihilation cross section of $\langle \sigma v \rangle \simeq 2 \times 10^{-26}$ cm^3/s, the 3FGL should contain on the order of $\sim$10 sources which are, in fact, dark matter subhalos.

The challenge, of course, lies not in merely detecting such subhalos, but in differentiating them from the much more numerous conventional unidentified sources. With this goal in mind, we expand upon previous work [160–166] in a number of ways. First of all, we employ Fermi's recently released catalog of gamma-ray sources, the 3FGL [157]. We also make use of the current Fermi dataset to extract a finely binned spectrum from each unassociated source, allowing us to make detailed comparisons with the predictions of various dark matter models. From this information, we place constraints on the dark matter annihilation cross section that are competitive with those derived from dwarf galaxies [135, 167], the Galactic Center [136], and the extragalactic gamma-ray background [137, 168]. We also identify a collection of 24 bright and high-latitude gamma-ray sources with dark matter-like spectra. We further investigate this list of prospective dark matter subhalo candidates by testing their angular distribution, and find evidence of spatial extension from the subhalo candidate source 3FGL J2212.5+0703.

The remainder of this chapter is structured as follows. In sec. 2.2, we describe our calculation of the distribution of dark matter subhalos and their predicted gamma-ray fluxes. In sec. 2.3, we discuss the characteristics of the unassociated source population presented in the 3FGL catalog, and place cuts on variability and galactic latitude in an effort to separate prospective subhalo candidates from astrophysical sources. In sec. 2.4, we describe our analysis of the Fermi data and the determination of the spectra from the 3FGL's unassociated sources. Focusing on the most promising subhalo candidates, we test these sources for

[1] In the Galactic Plane, some 3FGL sources also remain unassociated due to challenges in discriminating between multiple astrophysical objects in the same region of the sky.

indications of spatial extension and discuss how likely an extended source detection is in sec. 2.5. In sec. 2.6, we examine the implications if the detectably extended unassociated source 3FGL J2212.5+0703 is actually a dark matter subhalo. In sec. 2.7, we use the number of observed subhalo candidates to derive constraints on the dark matter annihilation cross section, finding limits that are competitive with the strongest constraints from other gamma-ray observations. Finally, in sec. 2.8, we summarize our results and comment on the prospects for future study.

2.2 Gamma-Rays From Nearby Dark Matter Subhalos

The prospects for observing gamma-rays from nearby dark matter subhalos depend not only on the characteristics of the dark matter particle itself, but on the local abundance and density profiles of the subhalos. To estimate these quantities, we make use of the results of the Aquarius Project, which has provided the highest resolution simulations to date of the dark matter subhalo populations found within the halos of Milky Way-like galaxies, identifying hundreds of thousands of subhalos, with masses as low as $3.24 \times 10^4 M_\odot$ [169]. The mass distribution of these subhalos takes the form of $dN/dM \propto M^{-1.9}$, with an overall normalization that corresponds to 13.2% of the Milky Way's total mass in dark matter.

In our calculations, we follow the approach of ref. [160], to which we direct the reader for further details. We will, however, repeat the main elements of our calculation here. Firstly, based on the results of the Aquarius simulation, we adopt the following distribution for subhalos in the local volume of the Milky Way (valid for distances $\sim 7-9$ kpc from the center) :

$$\frac{dN}{dMdV} = 260 \text{ kpc}^{-3}\, M_\odot^{-1} \times \left(\frac{M}{M_\odot}\right)^{-1.9}. \tag{2.1}$$

By integrating this expression between $M = 3.24 \times 10^4\, M_\odot$ and $10^7 M_\odot$, we find a local mass density in subhalos of 5700 $M_\odot/\text{kpc}^3$ (0.00022 GeV/cm^3), corresponding to approximately 0.054% of the overall local dark matter density (in good agreement with the local dark matter mass fraction in subhalos from fig. 12 of ref. [169]).

For each individual subhalo, we adopt an Einasto profile with $\alpha = 0.16$, truncated by the effects of tidal stripping, such that only the innermost 0.5% of the mass remains intact [160, 169]. For the initial concentration of each subhalo (prior to tidal effects), defined as the ratio of the virial and scale radii, $c \equiv r_{\rm vir}/r_{-2}$, we adopt values as presented in ref. [170], with subhalo-to-subhalo variations modeled by a log-normal distribution with a dispersion of $\sigma_c = 0.24$ [171]. In this respect, we depart from the mass-concentration relationship used in ref. [160], as based on the results of ref. [172]. This update of the mass-concentration relationship reduces the number of detectable subhalos (in gamma-rays) by a factor of approximately 4.6 relative to that presented in ref. [160].

The population of subhalos detectable in gamma-rays is dominated by the most massive and nearby members of this population. In our calculations, we include subhalos with masses up to $10^7 M_\odot$. We have chosen to limit our calculation to subhalos below this mass because we expect many of the more massive subhalos to contain significant quantities of baryons (stars and/or gas) and thus would be identified with dwarf spheroidal galaxies.

The differential gamma-ray spectrum per solid angle and energy from dark matter annihilations within an individual subhalo is given by:

$$\Phi(E_\gamma, \theta) = \frac{1}{8\pi m_\chi^2} \langle \sigma v \rangle \frac{{\rm d}N_\gamma}{{\rm d}E_\gamma} \int_{\rm l.o.s.} \rho^2[r(D, l, \theta)] \, {\rm d}l, \tag{2.2}$$

where m_χ is the mass of the dark matter particle, $\langle \sigma v \rangle$ is the thermally averaged annihilation cross section times the relative velocity, and dN_γ/dE_γ is the gamma-ray spectrum produced per annihilation, which we calculate using PYTHIA 8 [173]. The integral of the density squared is performed over the line of sight, D is the distance to the center of the subhalo, θ is the angle to the center of the subhalo, and $r(\theta, D, l) = \sqrt{D^2 + l^2 - 2Dl\cos\theta}$. The form of (2.2) assumes that the dark matter is self-conjugate. If the dark matter is not self-conjugate, then the derived cross section constraints become less stringent by a factor of 2.

In fig. 2.1, we plot the number of nearby (within a ∼kpc from us)[2] dark matter subhalos that are predicted to be bright gamma-ray sources ($F_\gamma > 7 \times 10^{-10}$ cm^{-2} s^{-1}, $E_\gamma > 1$ GeV, which is well above the threshold for inclusion in the 3FGL catalog), as a function of the annihilation cross section, for three choices of dark matter mass (for the case of annihilations proceeding to $b\bar{b}$). For an annihilation cross section near the value predicted for a simple thermal relic ($\langle \sigma v \rangle \approx 2 \times 10^{-26}$ cm^3/s), one expects such bright subhalos to exist only for relatively low values of the dark matter mass, $m_\chi \lesssim 100$ GeV. For lighter masses, however, one predicts that Fermi should have already detected gamma-ray emission from several such subhalos, constituting a population of presently unidentified sources without associated emission at other wavelengths.

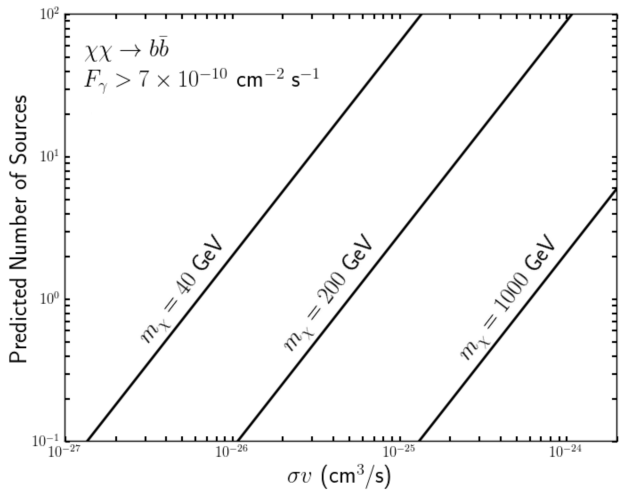

Figure 2.1: The number of nearby dark matter subhalos predicted by our calculations to be bright gamma-ray sources ($F_\gamma > 7 \times 10^{-10}$ cm^{-2} s^{-1}, $E_\gamma > 1$ GeV), as a function of the annihilation cross section, for three values of dark matter mass. We have assumed annihilations that proceed to $b\bar{b}$.

We emphasize that although non-negligible uncertainties do exist in our calculation of the number of dark matter subhalos above a given gamma-ray flux, the overall conclusions of these calculations are generally robust. Reasonable changes in our assumptions regarding the local number density of subhalos and dark matter distribution within subhalos could

[2]We will find later that subhalos that have a large ($\sim 1 \times 10^{-9}$ cm^{-2} s^{-1}) flux from gamma-rays will only be observable if they are within a kpc or so of us, c.f. fig. 2.12.

plausibly increase or decrease the predicted number of gamma-ray sources by up to a factor of a few. That being said, we have made a number of choices which we consider to be conservative, and thus expect our calculations to reflect a fairly realistic, albeit somewhat low, estimate for the number of such sources that might be observed. For example, steeper density profiles (as suggested by the Via Lactea II simulation [174]) could increase the predicted number of observable gamma-ray subhalos. Furthermore, if we had included subhalos larger than our cutoff of $10^7 M_{\odot}$, greater numbers of such sources would be predicted. We have also neglected any annihilation "boost factors" that might result from substructure within individual dark matter subhalos.

2.3 Unidentified Sources In the 3FGL Catalog

The Fermi Collaboration has recently released their third source catalog (3FGL), based on their first four years of data [157]. This catalog contains 3033 sources, each detected with greater than approximately 4σ significance. About half of these sources have been identified as, or associated with, known active galaxies (including BL Lacs, flat spectrum radio quasars, and other classes of active galaxies). A smaller, but not insignificant number, of these sources have also been associated with galactic objects, including pulsars, supernova remnants, and globular clusters. Of the 3033 sources contained in the 3FGL, 992 have not yet been identified or associated with emission observed at other wavelengths. It is among this subset of 3FGL sources that we could potentially find a population of dark matter subhalos.

The 3FGL provides information about each source that we will use to refine our search for dark matter subhalos. First, the Fermi Collaboration has tested each source for variability, as can be exhibited by some classes of astrophysical sources, but not by dark matter subhalos. Note that this test is performed by dividing the data into month-long temporal bins, and thus is not sensitive to variations taking place over shorter timescales, such as is observed from pulsars, for example. For each source, the Fermi Collaboration reports a value for its "variability index". In the left frame of fig. 2.2, we plot the distribution of this quantity observed among the 3FGL's unassociated source population. The dashed curve represents the

statistical distribution predicted for a population of non-variable sources (a χ^2 distribution with 47 degrees of freedom) [157]. For variability indices lower than approximately 80, these results are in good agreement, and thus provide no evidence of a variable population. In addition, we identify 18 unassociated 3FGL sources with a variability index greater than 80. In our analysis, we remove these 18 sources from our list of potential subhalo candidates.

In contrast to other galactic gamma-ray sources, which tend to be concentrated near the Galactic Plane, bright dark matter subhalos are predicted to be approximately isotropically distributed on the sky. We can therefore use galactic latitude as an indicator of the likelihood that a given gamma-ray source is a dark matter subhalo. In the right frame of fig. 2.2, we plot the latitude distribution of the 3FGL's unassociated sources. As a histogram binned in $\sin(b)$, an isotropic distribution would be flat, whereas the observed distribution clearly includes a population of sources that is concentrated around the Galactic Plane.

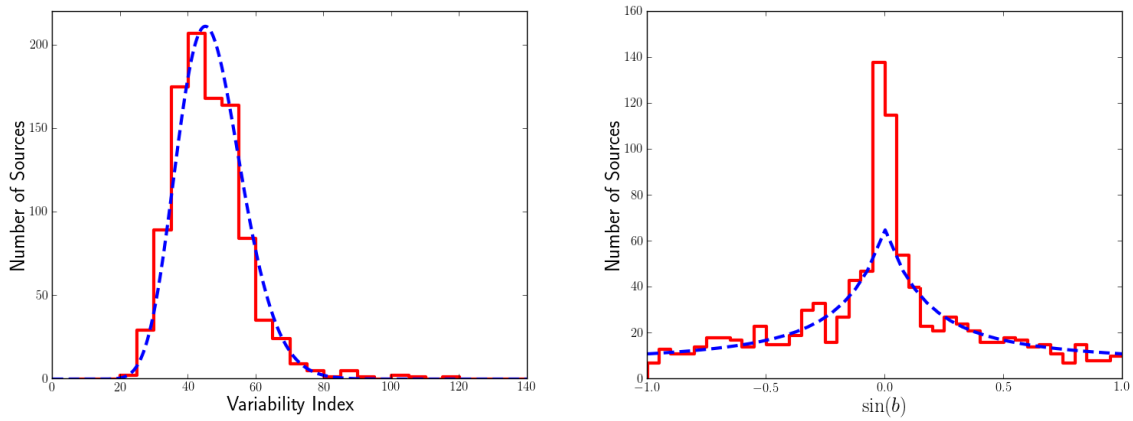

Figure 2.2: Left: The distribution of the variability index observed among the 3FGL's unassociated source population. The dashed curve represents the statistical distribution predicted for a population of non-variable sources (a χ^2 distribution with 47 degrees of freedom). Right: The latitude distribution of the 3FGL's unassociated sources. Based on a simple disk+isotropic population model (dashed curve), we estimate that approximately 20% of these sources are part of an isotropic population. In our analysis, we will focus on the unassociated sources with a variability index less than 80 and that are located at $|b| > 20^\circ$ ($|\sin b| > 0.342$).

To estimate how this distribution breaks down into different spatial populations, we model

the total distribution of sources as the sum of an isotropic component and a component with a thick disk-like distribution. For the disk-like distribution, we adopt $n \propto \exp(-z/z_0)$, and assume simply that individual sources are detectable out to a common distance of $d_{\rm max}$. Allowing the normalizations of the isotropic and disk-like components to vary, along with the parameters z_0 and $d_{\rm max}$, we find that the observed distribution is best-fit by $z_0/d_{\rm max} \simeq 0.1$ and $n_{\rm isotropic}/n_{\rm total} \simeq 0.45$ at $b = 90^\circ$ (shown as a dashed curve in the right frame of fig. 2.2). In this fit, we have neglected the innermost two bins of the distribution, which are highly biased by the incompleteness of multi-wavelength AGN catalogs in this region of the sky [157]. This simple model suggests that roughly $\sim$20% or $\sim$200 of Fermi's 992 unassociated sources are part of an isotropic population, consisting of galactic and extragalactic sources, and perhaps a small number of nearby dark matter subhalos. In our analysis, we will focus on Fermi's unassociated sources located at $|b| > 20^\circ$, allowing us to limit contamination from galactic astrophysical sources.

2.4 Fermi Data Analysis

To calculate the gamma-ray spectra from Fermi's unassociated sources, we utilize data taken over approximately 6.4 years of Fermi-LAT observations,[3] utilizing the Pass 7 Reprocessed photons in the energy range of 100 MeV to 100 GeV. We exclude events arriving at a zenith angle greater than 100°, as well as those which do not pass the "Source" photon data selection. We exclude events recorded while the instrument was not in science survey mode, when the instrumental rocking angle was >52°, or when the instrument was passing through the South Atlantic Anomaly. We examine the photons observed within a $14^\circ \times 14^\circ$ box centered around the location of each source, and divide the photons into 140×140 angular bins and 15 evenly spaced logarithmic energy bins. We analyze the instrumental exposure throughout the region of interest using the `P7REP_SOURCE_V15` instrumental response functions.

In our analysis, we employ the latest model for diffuse galactic gamma-ray emission,

[3]MET range 239557417 - 442851954

`gll_iem_v05_rev1.fit`, the latest isotropic emission template for the Source photon data selection `iso_source_v05.txt`, and include all 3FGL sources which lie within our region of interest. We allow the normalization of each source within 4 degrees to float independently in each energy bin, and do not impose any parameterization on their spectral shape. Our model also includes 3FGL sources which lie nearby (but outside) of the region of interest. To calculate the best fit flux from each source (in each energy bin), we use the Fermi-LAT `pyLikelihood` code, utilizing the `MINUIT` algorithm. We also calculate the upper limit of the source flux using the `pyLikelihood UpperLimits` tool in each energy bin, and present only the (2σ) upper limit whenever the flux is smaller than twice the calculated flux error.

In figs. 2.3 and 2.4, we plot the gamma-ray spectra from the 14 brightest ($F_\gamma > 2 \times 10^{-9}$ cm^{-2} s^{-1}, $E_\gamma > 1$ GeV) non-variable (variability index < 80), unassociated 3FGL sources located outside of the Galactic Plane ($|b| > 5^\circ$). The 9 sources shown in fig. 2.3 are reasonably well fit ($\chi^2 < 25$) by dark matter annihilating to $b\bar{b}$, and the dashed curves represent this prediction for the best-fit value of the dark matter mass. The 5 sources shown in fig. 2.4, in contrast, are not well-fit for any choice of the dark matter mass.

Of the well-fit sources shown in fig. 2.3, we note that all 9 prefer dark matter masses in the range of roughly 20 to 70 GeV. This is further explored in fig. 2.5, where we plot the galactic latitude and best-fit dark matter mass (for annihilations that proceed to $b\bar{b}$) for each of the unassociated 3FGL sources with $F_\gamma > 1.0 \times 10^{-9}$ cm^{-2}s^{-1} ($E_\gamma > 1$ GeV), variability index < 80, and $|b| > 5^\circ$. The error bars around each point represent the range of dark matter masses for which the fit to the spectrum yields $\chi^2 < 25$. We note two things about this plot. First, the distribution of these sources is not isotropic, and a component concentrated around the disk is clearly evident. Among the 12 of these sources with $|b| > 20^\circ$, however, the distribution is consistent with isotropy. Second, nearly all of these sources favor dark matter masses in the range of approximately 20 to 70 GeV. While this could represent an indication of dark matter subhalos with $m_\chi \sim 30 - 50$ GeV, the spectral shape in question is similar to that observed from many gamma-ray pulsars.

In tab. 2.1, we list what we consider to be Fermi's most promising dark matter subhalo

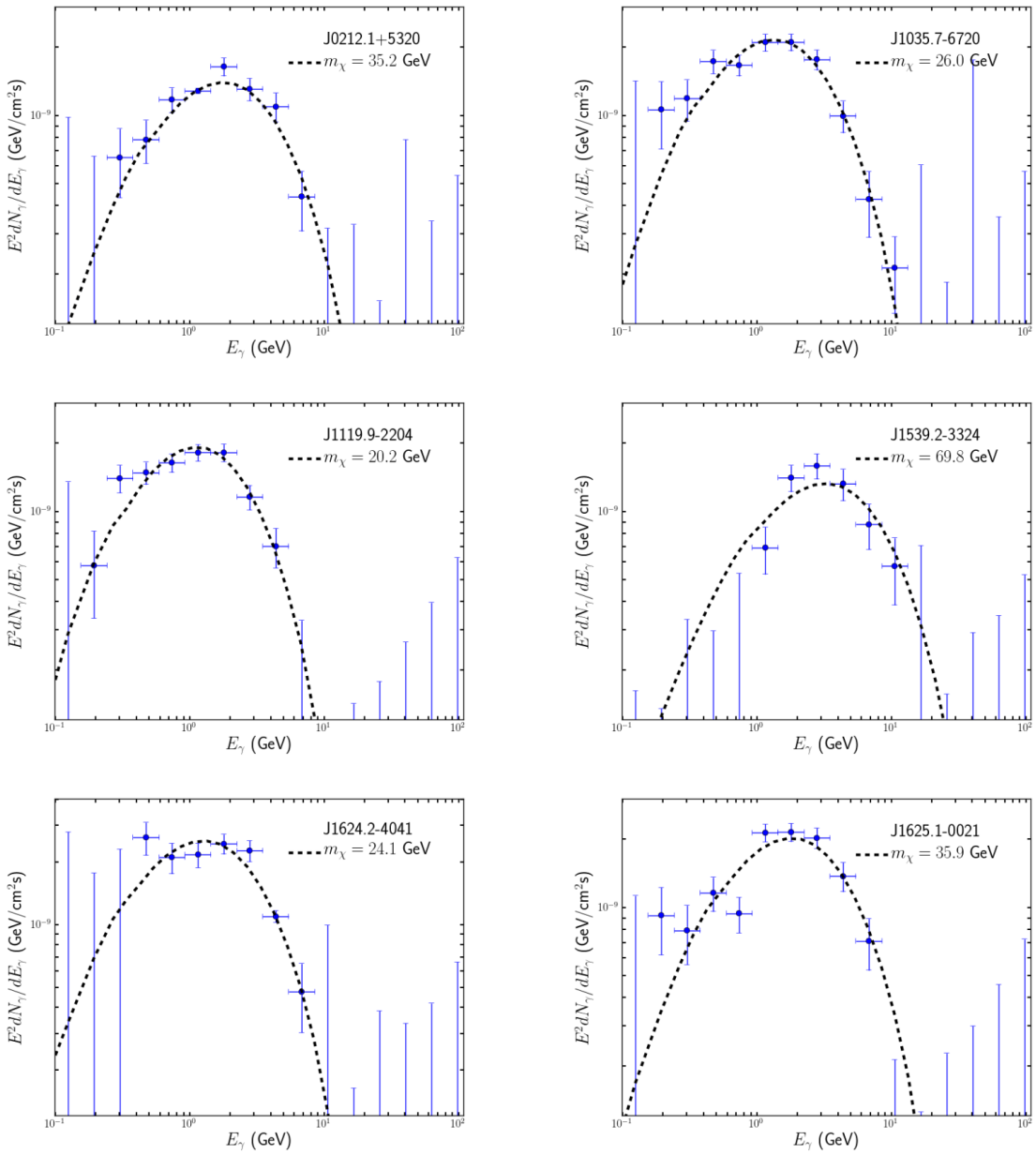

Figure 2.3: The gamma-ray spectra from 9 of the brightest ($F_\gamma > 2 \times 10^{-9}$ cm^{-2} s^{-1}, $E_\gamma > 1$ GeV), non-variable (variability index < 80), unassociated 3FGL sources located outside of the Galactic Plane ($|b| > 5^\circ$). Each of these 9 sources are reasonably well fit ($\chi^2 < 25$) by dark matter annihilating to $b\bar{b}$, and the dashed curves represent this prediction for the best-fit value of the dark matter mass.

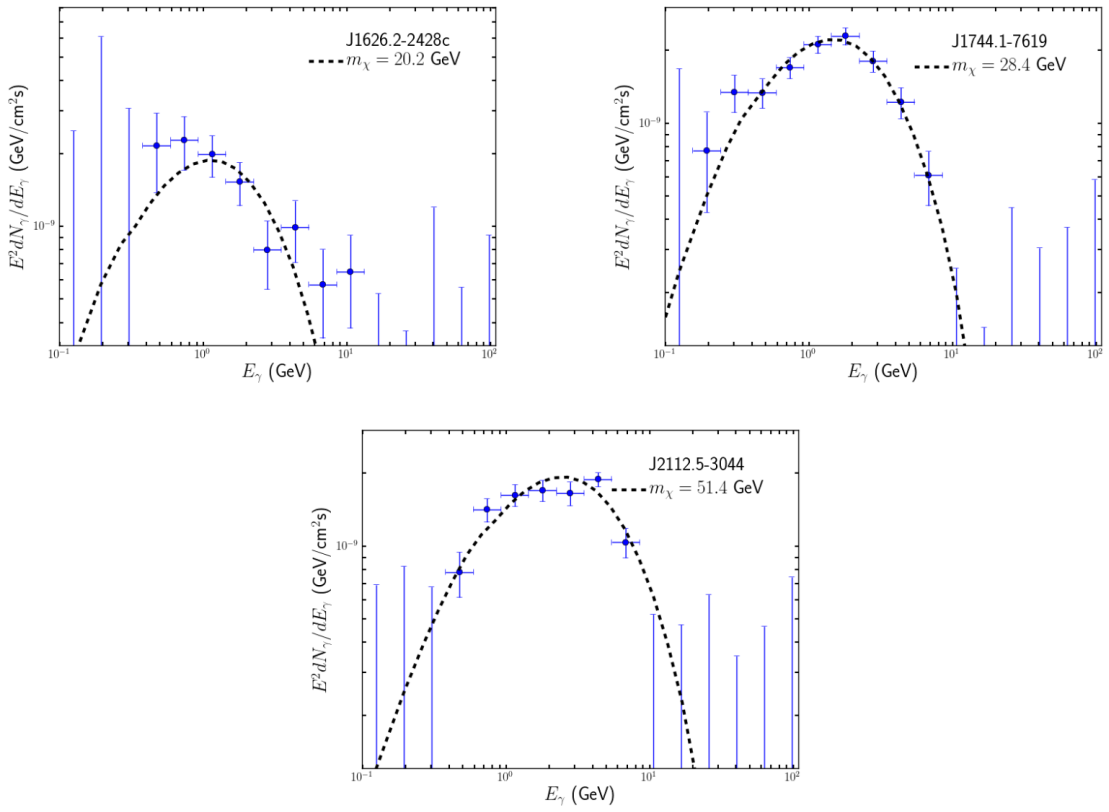

Figure 2.3 (Cont.)

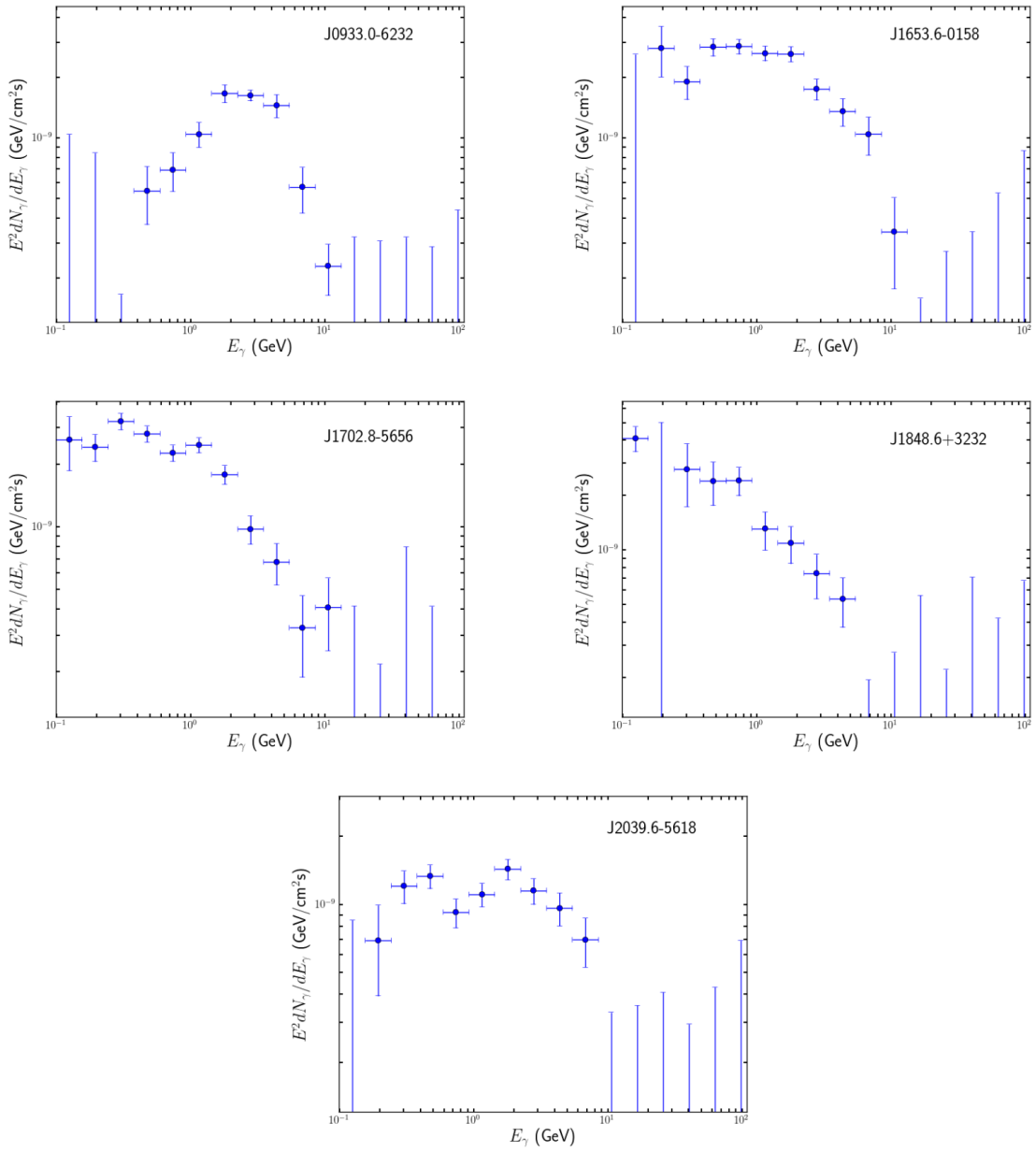

Figure 2.4: As in fig. 2.3, but for the 5 bright ($F_\gamma > 2 \times 10^{-9}$ cm^{-2} s^{-1}, $E_\gamma > 1$ GeV), non-variable (variability index < 80), unassociated 3FGL sources located outside of the Galactic Plane ($|b| > 5°$) that are *not* well-fit by any dark matter particle annihilating to $b\bar{b}$.

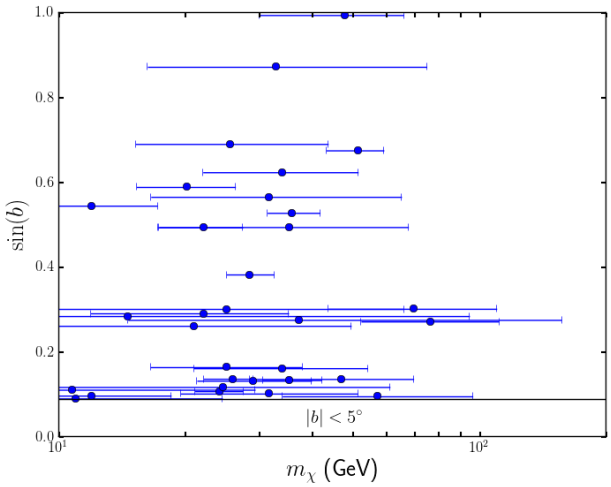

Figure 2.5: The distribution in galactic latitude and best-fit dark matter mass for those bright ($F_\gamma > 1.0 \times 10^{-9}$ cm^{-2}s^{-1}, $E_\gamma > 1$ GeV), non-variable (variability index < 80), unassociated 3FGL sources located outside of the Galactic Plane ($|b| > 5^\circ$). The error bars around each point represent the range of dark matter masses for which the fit to the spectrum yields $\chi^2 < 25$. In this figure, we have assumed annihilations that proceed to $b\bar{b}$.

candidates. This includes all unassociated and non-variable sources with $|b| > 20^\circ$, $\Phi_\gamma > 7 \times 10^{-10}$ cm^{-2} s^{-1} (> 1 GeV), and that are well-fit ($\chi^2 < 25$) by annihilating dark matter for at least one value of the dark matter's mass (assuming annihilations to $b\bar{b}$). In our opinion, the sources contained in this list merit further investigation. If associated emission can be detected at other wavelengths, these sources could be excluded as subhalo candidates, allowing us to derive stronger constraints on the dark matter annihilation cross section. Alternatively, the lack of counterparts at other wavelengths could strengthen the case that one or more of these candidates are, in fact, dark matter subhalos. Note that the sources marked with an asterisk in tab. 2.1 were discovered to have associations after the publication of our first paper [134][4] in which we derived the dark matter constraints reported in sec. 2.7 (see the caption of tab. 2.1 for details).

[4]We thank Elizabeth Ferrara, Fernando Camilo, Paul Ray, and Frank Schninzel for bringing these recent associations to our attention.

Source Name	Φ_γ (cm^{-2} s^{-1})	b (deg)	m_χ (GeV), best-fit	m_χ (GeV), $\Delta\chi^2 = 4$
3FGL J0312.1-0921	9.49×10^{-10}	-52.36	31.1	12.0 – 72.3
3FGL J0318.1+0252	1.23×10^{-9}	-43.64	25.5	19.5 – 32.2
3FGL J0456.2-6924	7.62×10^{-10}	-35.28	10.9	< 28.9
3FGL J0953.7-1510	1.25×10^{-9}	29.61	35.2	26.9 – 47.8
3FGL J1119.9-2204	2.70×10^{-9}	36.06	20.2	17.2 – 23.7
3FGL J1120.6+0713	1.10×10^{-9}	60.69	32.8	23.3 – 50.5
3FGL J1221.5-0632	8.06×10^{-10}	55.55	28.9	17.8 – 47.8
3FGL J1225.9+2953	1.42×10^{-9}	83.76	47.8	30.0 – 64.9
3FGL J1315.7-0732	8.35×10^{-10}	54.83	34.6	17.8 – 77.7
3FGL J1543.5-0244	7.35×10^{-10}	38.90	10.0	< 40.7
3FGL J1544.6-1125*	1.01×10^{-9}	32.98	12.0	< 16.8
3FGL J1601.9+2306	8.56×10^{-10}	46.94	27.4	< 187.7
3FGL J1625.1-0021	3.6×10^{-9}	31.84	35.9	31.6 – 41.4
3FGL J1659.0-0142	9.26×10^{-10}	23.91	37.9	< 273.8
3FGL J1704.4-0528	8.89×10^{-10}	20.80	35.2	< 964.7
3FGL J1720.7+0711	8.89×10^{-10}	23.41	22.9	< 72.3
3FGL J1744.1-7619*	3.85×10^{-9}	-22.47	28.4	25.5 – 32.2
3FGL J1803.3-6706	7.12×10^{-10}	-20.37	45.3	25.0 – 72.4
3FGL J1946.4-5403*	1.72×10^{-9}	-29.56	22.1	17.2 – 26.9
3FGL J2103.7-1113*	1.091×10^{-9}	-34.42	31.6	21.3 – 47.0
3FGL J2112.5-3044	3.26×10^{-9}	-42.45	51.4	43.7 – 58.3
3FGL J2133.0-6433	8.36×10^{-10}	-41.27	26.4	13.1 – 61.5
3FGL J2134.5-2131	7.06×10^{-10}	-45.08	50.5	17.5 – 165.5
3FGL J2212.5+0703	1.24×10^{-9}	-38.56	34.0	21.8 – 51.5

Table 2.1: A list of Fermi's most promising dark matter subhalo candidates. In particular, this table includes all unassociated, non-variable 3FGL sources with $|b| > 20^\circ$, $\Phi_\gamma > 7\times10^{-10}$ cm^{-2} s^{-1} (> 1 GeV), and that are well-fit ($\chi^2 < 25$) by annihilating dark matter for at least one value of the dark matter's mass (assuming annihilations to $b\bar{b}$). The sources marked with an asterisk were discovered to be associated after the publication of our first paper [134]. It was found that J1544.6-1125 is associated with a MSP [175], J1744.1-7619 with a pulsar [176], J1946.4-5403 with a MSP [176], and J2103.7-1113 with an AGN [177].

2.5 Spatial Extension

Most astrophysical gamma-ray emitters (pulsars, blazers, etc.) are effectively point sources, without any potentially observable spatial extension. A fraction of dark matter subhalos, on

the other hand, could be detectably extended, especially those most nearby and large. In this section, we study the dark matter subhalo candidate sources identified in the previous section in an effort to determine whether they exhibit any evidence of spatial extension.

We recognize, however, that there do exist classes of astrophysical sources that produce gamma-ray emission and have a spatial extension that is detectable by Fermi, including pulsar wind nebulae, supernova remnants (SNRs), molecular clouds, galaxy clusters, and nearby galaxies. More specifically, the Fermi collaboration has reported spatial extension from 25 3FGL sources [157], 21 of which are associated with known supernova remnants or pulsar wind nebulae (PWNe).[5] The other 4 of these sources are the star-forming region (SFR) Cygnus X, the lobes of the radio galaxy Centaurus A, and the satellite galaxies known as the Large and Small Magellanic Clouds (LMC, SMC). Note that all but three of these sources are located near the Galactic Plane ($|b| < 10^{\circ}$); only the LMC, SMC, and Centaurus A are located at higher latitudes. We also point out that all 25 of these gamma-ray sources are quite bright, as is expected for any source from which Fermi could detect spatial extension.

For the purposes of this study, the most important feature of this collection of Fermi sources with detectable extension is that they are all very bright and easily detectable at other wavelengths. Additionally, in order for an astrophysical object at a distance d to be spatially extended at a level detectable by Fermi, it must have a size of at least $\sim 10^{18}$ cm (d/100 pc). Such a source can clearly not be a pulsar or any other compact object. Instead, extended astrophysical sources generate gamma-rays though the interactions of cosmic ray electrons and/or protons with a surrounding diffuse target of gas or radiation. Such cosmic rays will also invariably generate radio emission via synchrotron radiation. Furthermore, the heating of the diffuse material by the shock waves associated with the cosmic rays will generate radiation at a combination of x-ray, ultraviolet, visible, and/or infrared wavelengths.

[5]The source 3FGL J1615.3-5146e (associated with SNR/PWN) is spatially coincident with a massive star cluster, which itself contains several possible gamma-ray sources, including SNRs detected at x-ray wavelengths (by both Suzaku and XMM-Newton) [178,179]. Although five pulsars have also been detected within this system, none appear to be luminous enough to power a PWN capable of producing the observed gamma-ray emission [180]. Despite the unclear origin of the gamma-ray emission from this source, it is very bright in radio, x-ray, and other wavelengths.

And in contrast to compact objects, the multi-wavelength emission generated in diffuse environments is not readily absorbed or significantly beamed, making the detectability of these accompanying signal all but inevitable.

As the Fermi Collaboration did not identify any other spatially extended sources, we do not expect any of the subhalo candidates under consideration to exhibit extension at a highly statistically significant level. Given the larger data set that is currently available, however, it is possible that spatial extension could be detectable in one or more of our subhalo candidates at a non-negligible level.

To test for evidence of spatial extension, we repeat the procedure described in the previous section, replacing the point-source template with a extended template, varying the width σ as a free parameter. We consider three models for spatial extension:

1. An angular distribution corresponding to a simple two-dimensional Gaussian.

2. An angular distribution corresponding to a Navarro-Frenk-White (NFW) dark matter profile.

3. An angular distribution corresponding to an NFW dark matter profile, truncated by the effects of tidal stripping, such that only the innermost 0.5% of the subhalo's mass remains intact [160, 169]. We consider this to be the most physically realistic of the extension models considered.

The NFW density profile itself is given by [46, 181]

$$\rho(r) = \frac{\rho_0}{(r/R_s)[1 + (r/R_s)]^2} \ . \tag{2.3}$$

To determine the subhalo's scale radius R_s we adopt the mass-concentration relationship described in ref. [170]. For each of the angular profiles described above, we define the width σ such that 68% of the photons from the source originate from within this radius.

To compare the fits to the photon data using point-like vs. extended source models, we compared the test statistic (TS) for the source, defined as twice the log-likelihood (assuming

Poisson statistics for the detected photons) of the data given a model with a source present minus twice the log-likelihood given a model with no source present (the null hypothesis), for the cases of a point-like (pt) source and an extended (ext) source, i.e.

$$TS_{\rm pt,ext} = 2\ln(\mathcal{L}_{\rm pt,ext}/\mathcal{L}_{\rm no\ source}) \ , \tag{2.4}$$

$$\mathcal{L} = \prod_{i,j} p_{ij} \ , \tag{2.5}$$

where

$$p_{ij} = \frac{\theta_{ij}^{n_{ij}} e^{-\theta_{ij}}}{n_{ij}!} \ , \tag{2.6}$$

is the Poisson probability of observing n_{ij} counts in pixel i and energy bin j when the number of counts predicted by the model is θ_{ij}. Since the model with the source requires only one new free parameter, by Wilk's theorem, the TS should be asymptotically distributed as $\chi^2/2$ with one degree of freedom, making the significance of the source equal to $\sqrt{TS}\ \sigma$ [182].

In fig. 2.6, we plot the change in the test statistic ($TS_{\rm ext} - TS_{\rm pt} = 2\ln(\mathcal{L}_{\rm ext}/\mathcal{L}_{\rm pt})$). Of the 14 sources considered (those with $|b| > 20^\circ$ and $F_\gamma > 10^{-9}$ cm^{-2} s^{-1}, $E_\gamma > 1$ GeV, which have no recent associations), we found 9 which show very little or no evidence (ΔTS < 1.0) in favor of extension for any of the three models considered. In tab. 2.2, we list the results of our tests for spatial extension from these 14 dark matter subhalo candidates. For the 5 sources that prefer an extended profile (at the level of ΔTS > 1), we provide the best-fit value for their extension parameter σ. For all 14 of these sources, we provide the 2σ upper limit on the degree of spatial extension (corresponding to the value of σ for the first time in which ΔTS > 4).

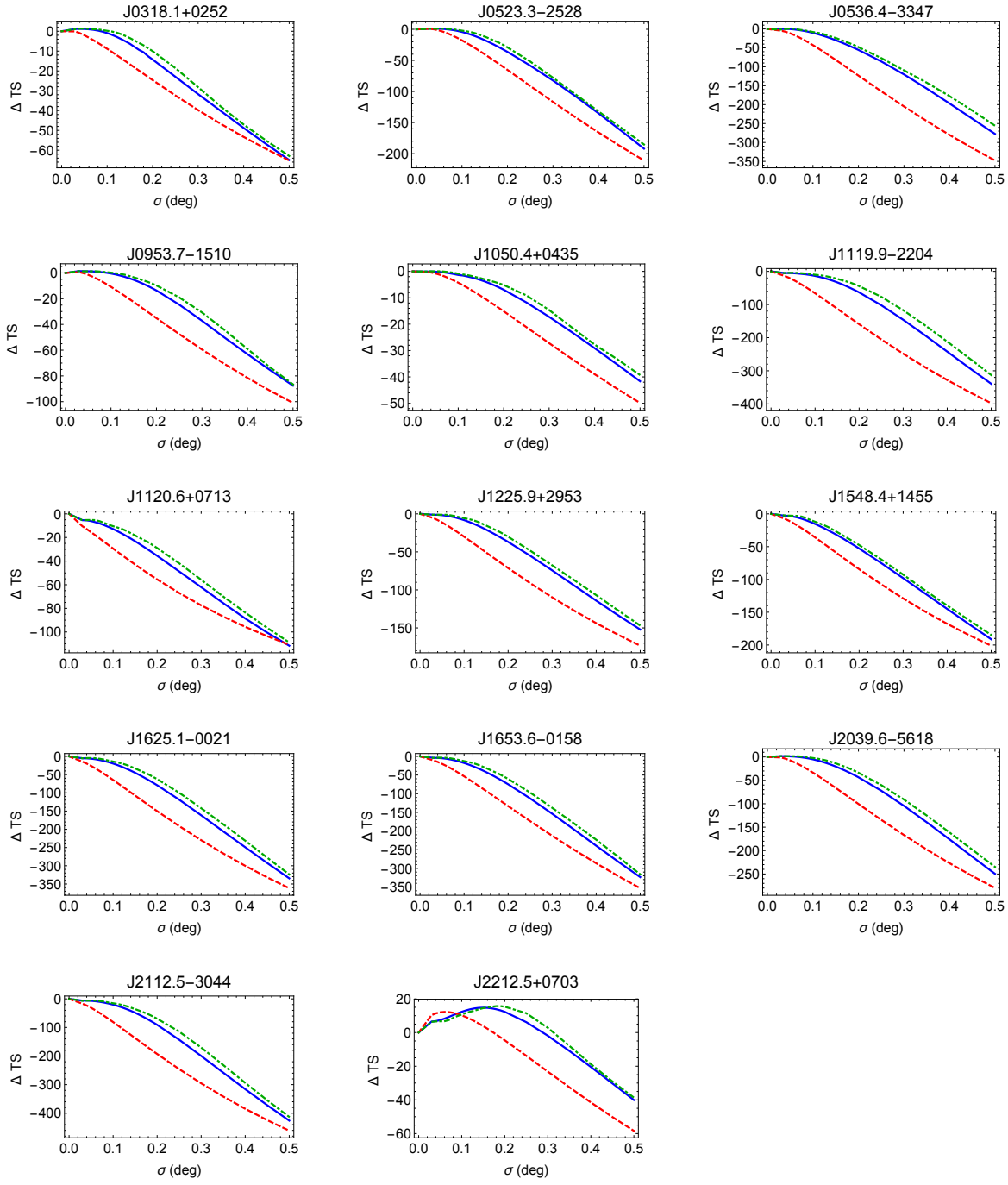

Figure 2.6: The change in the test statistic (TS) as a function of spatial extension for the 14 bright, high-latitude subhalo candidate sources considered in our study. Results are shown for three different morphologies: a tidally stripped NFW profile (green dot-dashed), an untruncated NFW profile (red dashed), and a two-dimensional Gaussian (blue solid). The source 3FGL J2212.5+0703 shows significant evidence of being spatially extended.

Source Name (3FGL)	NFW (tidally stripped)		NFW (unstripped)		Gaussian	
	σ	ΔTS	σ	ΔTS	σ	ΔTS
J2212.5+0703	0.19° ($< 0.35^\circ$)	15.7	0.06° ($< 0.20^\circ$)	12.2	0.15° ($< 0.35^\circ$)	14.8
J0318.1+0252	0.05° ($< 0.16^\circ$)	1.4	0.01° ($< 0.07^\circ$)	0.55	0.04° ($< 0.14^\circ$)	1.2
J0523.3-2528	0.06° ($< 0.12^\circ$)	1.2	0.02° ($< 0.06^\circ$)	1.1	0.04° ($< 0.10^\circ$)	1.1
J0953.7-1510	0.03° ($< 0.16^\circ$)	1.4	0.01° ($< 0.07^\circ$)	1.3	0.01° ($< 0.14^\circ$)	1.5
J2039.6-5618	0.03° ($< 0.12^\circ$)	1.8	0.01° ($< 0.05^\circ$)	1.5	0.02° ($< 0.10^\circ$)	1.8
J0536.4-3347	$< 0.09^\circ$	–	$< 0.03^\circ$	–	$< 0.08^\circ$	–
J1050.4+0435	$< 0.18^\circ$	–	$< 0.10^\circ$	–	$< 0.17^\circ$	–
J1119.9-2204	$< 0.01^\circ$	–	$< 0.01^\circ$	–	$< 0.01^\circ$	–
J1120.6+0713	$< 0.01^\circ$	–	$< 0.01^\circ$	–	$< 0.01^\circ$	–
J1225.9+2953	$< 0.09^\circ$	–	$< 0.03^\circ$	–	$< 0.08^\circ$	–
J1548.4+1455	$< 0.07^\circ$	–	$< 0.02^\circ$	–	$< 0.05^\circ$	–
J1625.1-0021	$< 0.01^\circ$	–	$< 0.01^\circ$	–	$< 0.01^\circ$	–
J1653.6-0158	$< 0.07^\circ$	–	$< 0.01^\circ$	–	$< 0.04^\circ$	–
J2112.5-3044	$< 0.01^\circ$	–	$< 0.01^\circ$	–	$< 0.01^\circ$	–

Table 2.2: The results of our test for spatial extension for the 14 bright ($F_\gamma > 10^{-9}$ cm^{-2} s^{-1}) and high-latitude ($|b| > 20^\circ$) dark matter subhalo candidates with the three extension models described in the text. For 3FGL J2212.5+0703, we find significant evidence in favor of spatial extension. For the next four sources listed, the fit very modestly prefers a spatially extended distribution (at the level of $\Delta\text{TS} > 1$, for at least one choice of extension model). For these four sources, we provide the best-fit value for their extension parameter σ. The other 10 sources show no significant preference for any spatial extension. For each source, we provide the 2σ upper limit on the degree of spatial extension (corresponding to the value of σ for the first time in which $\Delta\text{TS} > 4$).

The most significant evidence for extension is from 3FGL J2212.5+0703, for which the TS increases by 15.7 when the point-like template is replaced by a tidally stripped NFW profile with a width of $\sigma = 0.19^\circ$ (the untruncated NFW and Gaussian profiles also favor extension, although at a slightly lower level). This corresponds to a local statistical significance of 4.0σ (or 3.4σ after accounting for a trials factor of 8, corresponding to the number of sources tested for extension which are also among the promising subhalo candidates from tab. 2.1). This source, 3FGL J2212.5+0703, is one of the promising high-latitude dark matter subhalo candidates identified in sec. 2.4, and is well-fit by $m_\chi \simeq 21.8 - 51.5$ GeV (for annihilations to $b\bar{b}$); see tab. 2.1. In fig. 2.7, we show the gamma-ray spectrum of 3FGL J2212.5+0703. If the significance of this extension were to increase as Fermi continues to collect more data,

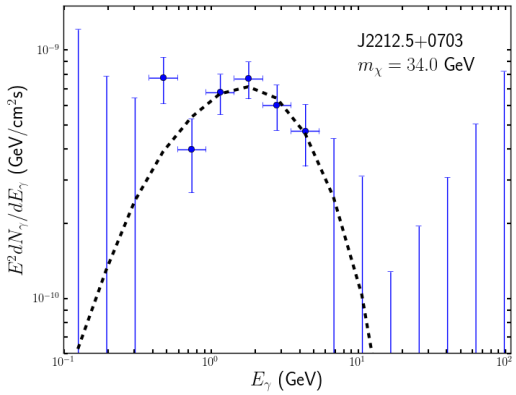

Figure 2.7: The spectrum of J2212.5+0703. The dashed curve denotes the spectral shape predicted from a 34 GeV dark matter particle that annihilates to $b\bar{b}$. Dark matter masses in the range 21.8-51.5 GeV provide a good fit to the measured spectrum.

it would help to support a dark matter subhalo interpretation for this source, over that of a pulsar or other point-like object. For 3FGL J2212.5+0703 we repeated our fit, but allowing the flux in each energy bin for each source within 10° to vary freely in the fit, and allowing the values of these parameters to float as we adjusted the spatial extension of the source under consideration (in contrast, thus far in this study we have only allowed those sources within 4° to float, and have fixed the flux for the background sources within 4° in each energy bin to their best fit values for the case of a point-like (non-extended) source template, not allowing their values to shift as extension is introduced). After allowing for this additional freedom in the fit, the preference for an extended profile increased slightly for 3FGL J2212.5+0703, to a level of $\Delta\mathrm{TS} = 18.4$.

To further investigate the morphology of the source 3FGL J2212.5+0703, we show in fig. 2.8 the map of the gamma-ray residuals in the 5°×5° region surrounding 3FGL J2212.5+0703. This represents the total photon count map, after subtracting the best-fit background model (including the diffuse and isotropic backgrounds, as well as the nearby point source models, but excluding the source model for 3FGL J2212.5+0703). This can be compared directly to the residual maps shown in fig. 2.9, which are of the region surrounding the point-like unassociated Fermi source 3FGL J1119.9-2204. The spatial extension of 3FGL J2212.5+0703

can be seen by eye when the residual maps of these two sources are compared. We also note that the profile of 3FGL J2212.5+0703 may depart from spherical symmetry, perhaps the result of a non-spherical stripping of a dark matter subhalo.

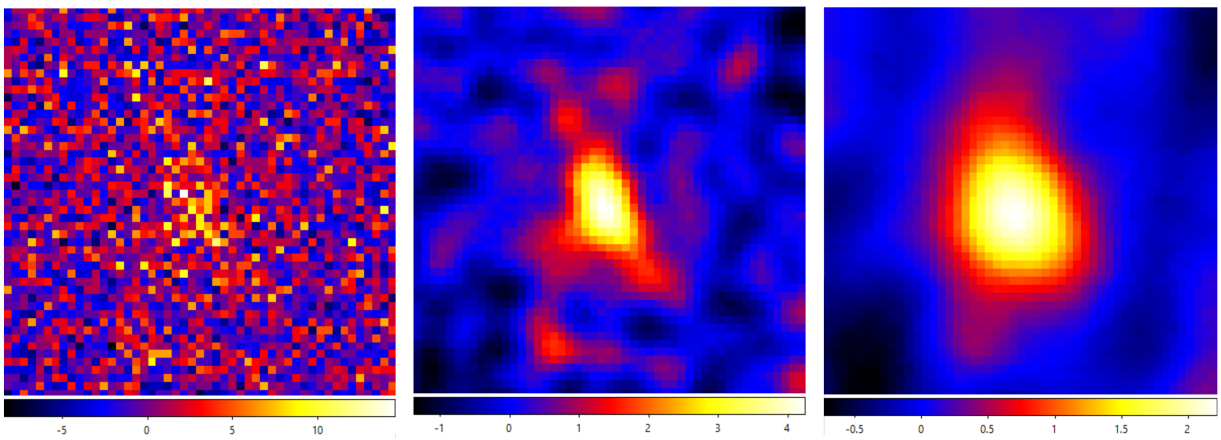

Figure 2.8: Residual maps of the 5°×5° region surrounding the dark matter subhalo candidate 3FGL J2212.5+0703. The left frame is unsmoothed, whereas the center and right frames have been smoothed with a Gaussian function with a smoothing length of 4 and 9 pixels, respectively.

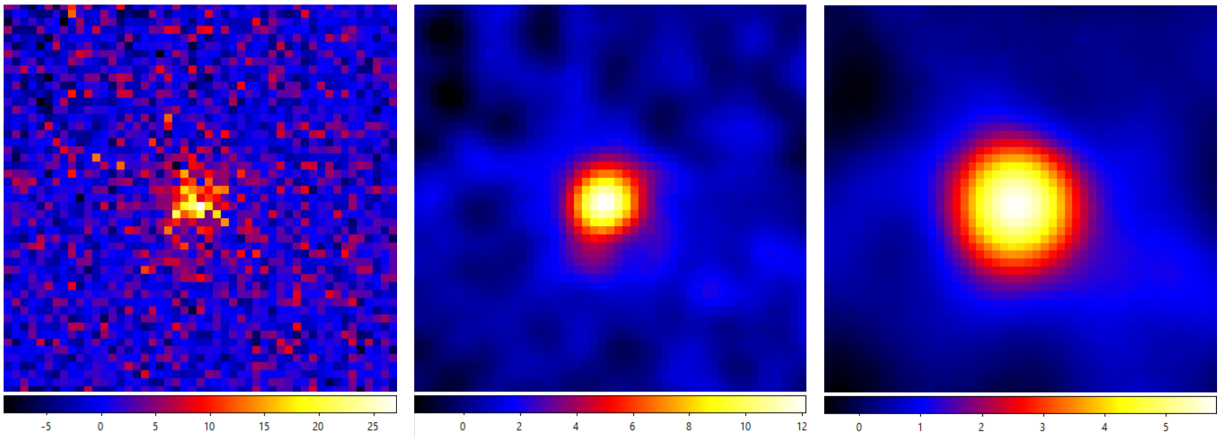

Figure 2.9: As in fig. 2.8, but for the source 3FGL J1119.9-2204, which exhibits no evidence of spatial extension. We show this as an example of a point-like Fermi source.

In addition to the unassociated sources discussed above, the 3FGL catalog contains many sources that are associated with emission observed at other wavelengths. These sources, which are very unlikely to be dark matter subhalos, provide us with an opportunity to

test our procedure for detecting spatial extension. In order to make a fair "apples-to-apples" comparison, we consider only those associated 3FGL sources that are located at high altitudes ($|b| > 20^{\circ}$) and that emit a gamma-ray flux in the same range as our 14 subhalo candidates (10^{-9} cm^{-2} s^{-1} $< F_{\gamma} < 4.23 \times 10^{-9}$ cm^{-2} s^{-1}). Of the 252 sources that meet this criteria, 229 are associated with AGN, along with a smaller number of pulsars (16), galaxies (6), and a single globular cluster.

Following the approach described above, we have tested each of these 252 sources for evidence of spatial extension. In fig. 2.10, we show the results for a small sub-sample of these sources. Of the full collection of these 252 sources, we do not find any that exhibits as much evidence for extension as 3FGL J2212.5+0703 (with the exception of 3FGL J0059.0-7242e, the Small Magellanic Cloud, which one of the known extended sources in the 3FGL catalog). Otherwise, the most significant evidence of extension was observed from 3FGL J0455.7-4617, which is associated with an AGN (PKS 0454-46).[6] This source is located at a cosmological distance ($z = 0.858$) and should not be extended. Nonetheless, the fit prefers a tidally stripped NFW (Gaussian) profile over the point-like template at the level of $\Delta\text{TS} = 2.8$ (3.3). Strangely, this source prefers a non-stripped NFW profile with a much greater significance, $\Delta\text{TS} = 19.0$. In fig. 2.11 we show the residual maps for the source 3FGL J0455.7-4617.

It is possible that the sources that we are detecting as extended are actually superpositions of two gamma-ray sources that lie along similar lines of sight. Considering a collection of N sources distributed across the $|b| > 20^{\circ}$ sky, the probability that two will lie within an angle α of each other is given by

$$\mathcal{P} = \frac{N(N-1)}{2} \frac{\pi\alpha^2}{4\pi r^2[1-\sin(20^{\circ})]} \, , \tag{2.7}$$

where $r = 360^{\circ}/(2\pi)$. If we include all unassociated high-latitude sources, then $N = 380$. Hence there is a roughly 8% chance that two of these sources are to fall within $\alpha = 0.1^{\circ}$

[6] More specifically, PKS 0454-46 is a flat spectrum radio quasar, which is a type of blazar.

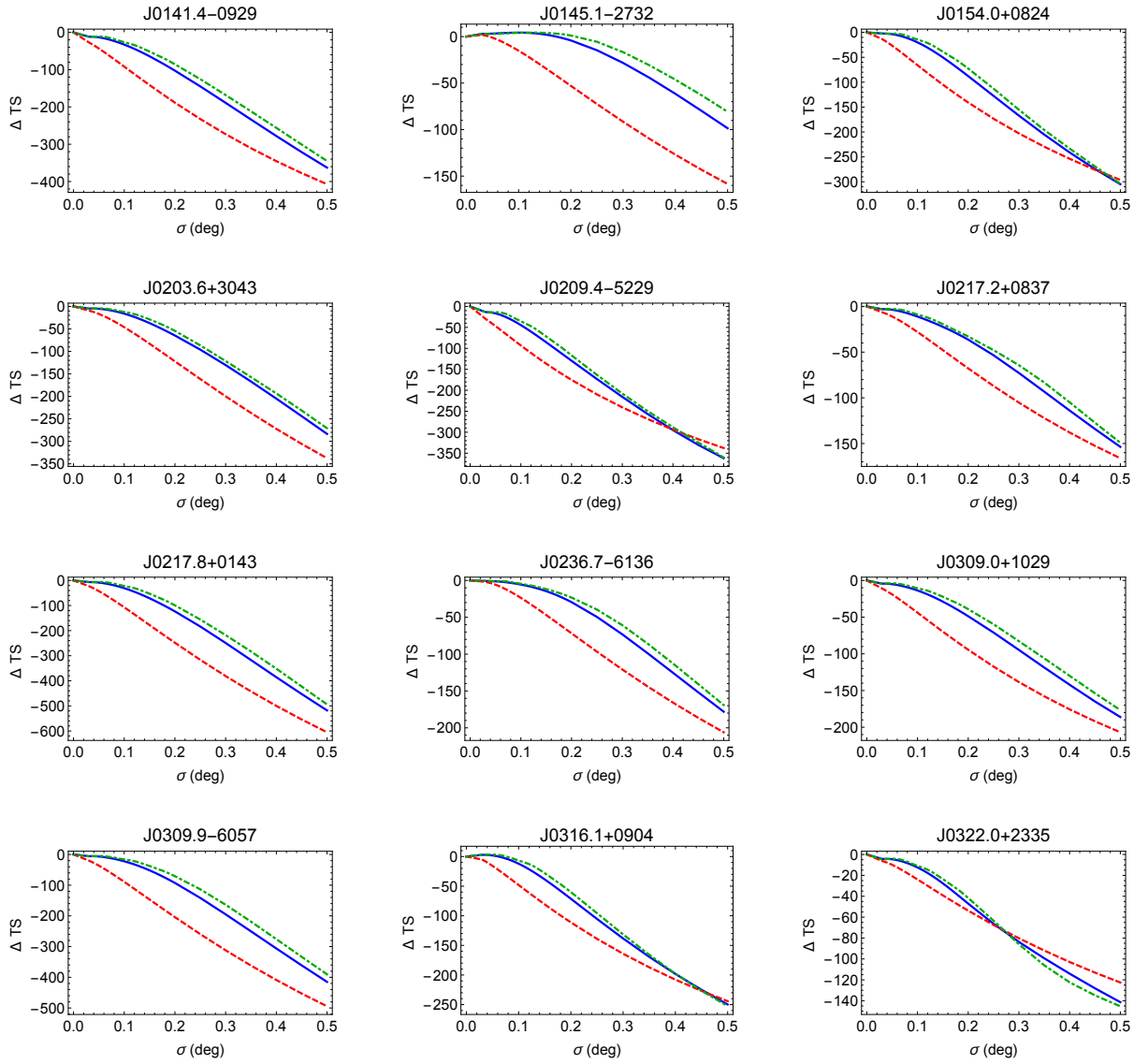

Figure 2.10: As in fig. 2.6, but for a selection of Fermi sources that have been associated and are located at high latitude ($|b| > 20°$) with a gamma-ray flux in the range of $F_\gamma = (1.0 - 4.23) \times 10^{-9}$ cm^{-2} s^{-1} ($E_\gamma > 1$ GeV).

of each other. If we require that the combined flux of the two sources be greater than that of 3FGL J2212.5+0703, then this probability drops to 1%, which is small, but not entirely negligible.

If 3FGL J2212.5+0703 and 3FGL J0455.7-4617 are actually superpositions of sources,

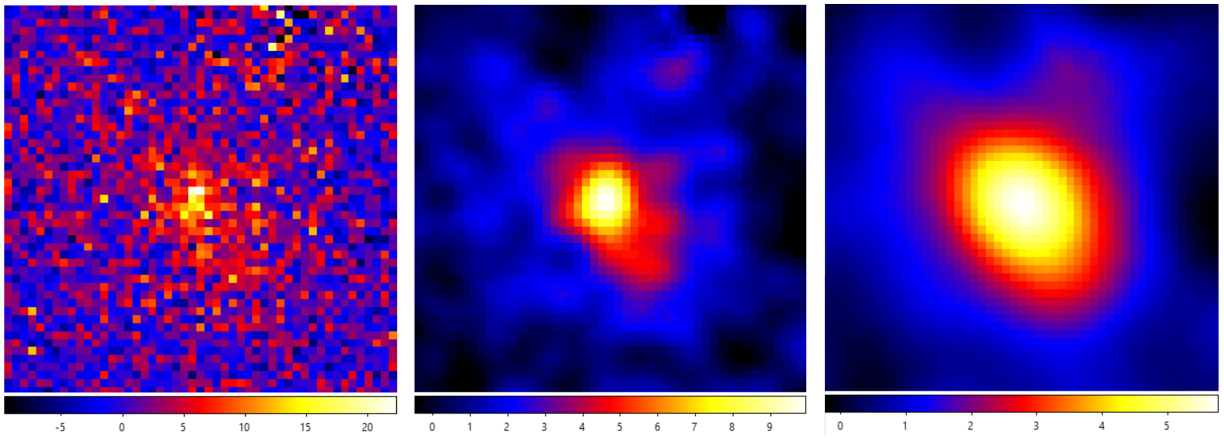

Figure 2.11: As in fig. 2.8, but for the source 3FGL J0455.7-4617, which exhibits evidence of spatial extension. Of the 252 bright, high-latitude, associated 3FGL sources that constitute our control group in this study, this source demonstrates the most significant preference for extension (ΔTS = 19.0 for an untruncated NFW profile, and surprisingly weaker evidence for tidally stipped NFW and Gaussian models, with ΔTS = 2.8 and 3.3 respectively. This source is associated with radio emission from a cosmologically distant ($z = 0.858$) AGN and is not expected to be discernibly extended.

then it is possible that one or both of these sources could be found in multi-wavelength catalogs, with only one gamma-ray source identified by Fermi. With this in mind, we have consulted the Roma-BZCAT Multi-Frequency Catalog of Blazars (BZCAT) [183], the Combined Radio All-Sky Targeted Eight-GHz Survey (CRATES) catalog [184], the Candidate Gamma-Ray Blazar Survey (CGRaBS) [185], and the Australia Telescope National Facility (ATNF) catalog [186].

Using these catalogs, two soures were found within 1° of 3FGL J2212.5+0703. BZQ J2212+0646/CRATES J221251+064604 is located approximately 0.3° away and CRATES J221408+071128 is located approximately 0.4° away. Each of these sources have radio fluxes of a few hundred mJy,[7] measured at several frequencies. In addition to the multi-wavelength source coincident with 3FGL J0455.7-4617, we also identify two CRATES sources 0.8° and 0.9° away. In the future, we plan to simulate gamma-ray sources at the location of these radio sources to determine if the extended source detection could be due to the superposition

[7] A Jansky (Jy) is a unit of radio flux density, equivalent to 10^{-26} Watts per square meter, per Hertz.

of two nearby point-like sources.

2.6 Implications of 3FGL J2212.5+0703 as a Dark Matter Subhalo

In this section, we assume that the gamma-rays from 3FGL J2212.5+0703 are in fact the result of annihilating dark matter and we consider what this observation would imply about this particular dark matter subhalo, and about the nature of the dark matter itself. We begin by recalling the gamma-ray spectrum produced in fig. 2.7. For the case of dark matter annihilating to $b\bar{b}$, the best fit spectrum is found for a dark matter mass of $m_\chi = 34.0$ GeV, and masses in the range 21.8–51.5 GeV provide a good fit. For dark matter that annihilates to light quarks (or gauge/Higgs bosons), lower (higher) masses can also provide a good fit to the measured spectrum at the 2σ ($\Delta\chi^2 = 4$) level. We also note that spectrum of 3FGL J2212.5+0703 is compatible with that observed from the Galactic Center excess (the Galactic Center excess is well-fit by dark matter annihilating to $b\bar{b}$ for $m_\chi \sim$ 36-55 GeV [127,144,145]) and the excess from the dwarf galaxy Reticulum II [131,132].

Following the work described in sec. 2.2, we calculate an analytic formula for the number of subhalos predicted to be detected by Fermi. For a 40 GeV dark matter particle annihilating to $b\bar{b}$, for example, we predict the following number of high-latitude ($|b| > 20^\circ$) subhalos that generate a gamma-ray flux above a threshold of $F_{\rm threshold}$ given by

$$N \sim 1.2 \times \left(\frac{\langle\sigma v\rangle}{10^{-26}\ {\rm cm}^3\ {\rm s}^{-1}}\right)^{1.5} \left(\frac{F_{\rm threshold}}{10^{-9}\ {\rm cm}^{-2}\ {\rm s}^{-1}}\right) \ . \tag{2.8}$$

Although there exist non-negligible uncertainties regarding the distribution of subhalo concentrations, and the degree to which their outer mass is tidally stripped, reasonable variations in these parameters change the predicted number of detectable subhalos by only a factor of a few or so, and we consider our estimate to be a reasonable prediction. For an annihilation cross section of 10^{-26} cm^3 s^{-1} (near the upper limit derived from observations of dwarf galaxies [135,167]), we expect Fermi to detect roughly one subhalo with $F_{\rm threshold} > 10^{-9}$ cm^3 s^{-1} and perhaps as many as ~ 10 with $F_{\rm threshold} > 10^{-10}$ cm^3 s^{-1}.

If 3FGL J2212.5+0703 is in fact a dark matter subhalo (and none of the other subhalo candidates are), it would suggest an annihilation cross section of $\langle \sigma v \rangle$ $(0.2-1.5) \times 10^{-26}$ cm^3 s^{-1} (90% C.L.). Of course, others of our candidate sources could also be subhalos. In particular, the four subhalo candidates 3FGL J0953.7-1510, 3FGL J1120.6+0713, 3FGL J1225.9+2953, and 3FGL J1625.1-0021 each exhibit spectral shapes that are compatible with that observed from 3FGL J2212.5+0703 (and from the Galactic Center and Reticulum II excesses). If any of these sources are in fact subhalos, it would increase our estimate for the dark matter's annihilation cross section.

Additionally, the gamma-ray flux and angular extent of 3FGL J2212.5+0703 can be used to constrain the mass and distance of the responsible subhalo. In the left frame of fig. 2.12, we plot the (pre-tidal stripping) M_{200} mass of a subhalo that produces the gamma-ray flux of 3FGL J2212.5+0703, as a function of distance. M_{200} is defined as the mass enclosed within a radius r_{200}, assuming the density is 200 times the critical density. r_{200} is related to the NFW scale radius R_s via $r_{200} = cR_s$ where c is the halo concentration [170]. Here we have assumed a dark matter mass of 34 GeV and an annihilation cross section of $\langle \sigma v \rangle = 2 \times 10^{-26}$ cm^3 s^{-1} to $b\bar{b}$.[8] From the flux alone, one cannot disentangle the mass of a subhalo from its proximity. Given the information contained in the left frame of fig. 2.12, 3FGL J2212.5+0703 could equally well be a very large subhalo (perhaps even an ultra-faint dwarf galaxy) located at a distance of ~ 10 kpc, or a solar mass clump of dark matter located not far from the us.

Although one might imagine that the angular extension of a subhalo could be used to constrain its characteristics, there is an approximate degeneracy between the size and distance which makes this measurement only mildly informative. In the right frame of fig. 2.12, we plot the discernible angular extension for a subhalo with the same flux as 3FGL J2212.5+0703 as a function of distance, again assuming a dark matter mass of 34 GeV and an annihilation cross section of $\langle \sigma v \rangle = 2 \times 10^{-26}$ cm^3 s^{-1} to $b\bar{b}$. The angular extension is defined as in [160]: 68% of the photons originate from within an angular radius equal to 82%

[8] The left frame of fig. 2.12 can be adjusted to reflect any value of the cross section by shifting the distance scale by a factor of $[\langle \sigma v \rangle / (2 \times 10^{-26}$ cm^3 s^{-1})]$^{1/2}$.

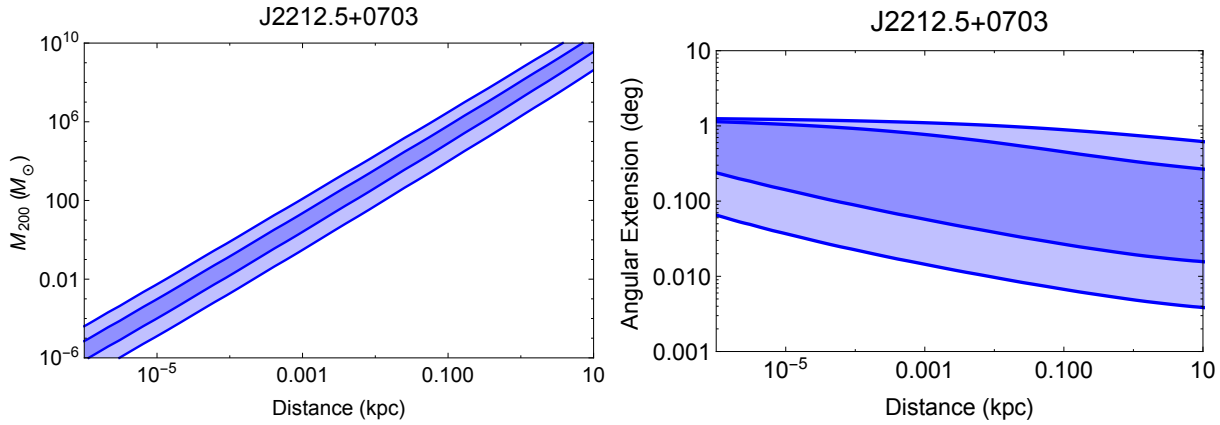

Figure 2.12: Left: The M_{200} mass (prior to tidal stripping) as a function of the distance of a subhalo that produces a gamma-ray flux equal to that observed from 3FGL J2212.5+0703. Right: The angular extension as a function of the distance of a subhalo that produces a gamma-ray flux equal to that observed from 3FGL J2212.5+0703. The inner (outer) blue band represents a 1σ (2σ) variation in the concentration and gamma-ray flux. Tidal stripping is varied between 90% and 99.5% for each of the bands. We assumed a dark matter mass of 34 GeV and an annihilation cross section of $\langle\sigma v\rangle = 2 \times 10^{-26}$ cm^3 s^{-1} to $b\bar{b}$.

of the quoted extension.

In each frame of fig. 2.12, the blue regions show results for a range of concentration, source flux, and tidal stripping assumptions. For both the inner dark blue and outer light blue bands, we have allowed the tidal stripping to vary between 90% and 99.5%. The inner (outer) blue bands allow for variations in the subhalo's concentration and the observed flux of 3FGL J2212.5+0703 by $\pm 1\sigma$ ($\pm 2\sigma$). Although the right frame of fig. 2.12 illustrates a trend in favor of less extension for more distant (and more massive, since the flux is fixed) subhalos, for the degree of extension observed from 3FGL J2212.5+0703 ($\sigma \approx 0.19°$), it is not possible to meaningfully constrain its distance.

2.7 Constraining the Dark Matter Annihilation Cross Section

In this section, we use the results of sec. 2.4 to place an upper limit on the number of bright, high-latitude dark matter subhalos, and use this to derive a constraint on the dark matter annihilation cross section. Note that this constraint is derived using all of the subhalo

candidates listed in tab. 2.1, even those that are marked as begin recently associated. We do this through the following procedure. First, for each subhalo candidate, we calculate the χ^2 of the fit for the gamma-ray spectrum predicted by a given dark matter model, and convert this into a p-value. Twice the sum of the p-values for all of the candidate sources under consideration represents the weighted number of sources. This method of calculating the number of sources uses information from all of the potential sources, as opposed to imposing a simple cut on χ^2 values, which removes some of the information in the fits. We plot the weighted number of sources in the left frame of fig. 2.13. As already seen in fig. 2.5, this result indicates that $\sim$10-15 of these sources could plausibly be subhalos of $\sim$20-50 GeV dark matter particles (they could also be pulsars, however). Dark matter particles with heavier masses ($\gtrsim$ 100 GeV), in contrast, do not provide a good fit to any of the subhalo candidate sources.

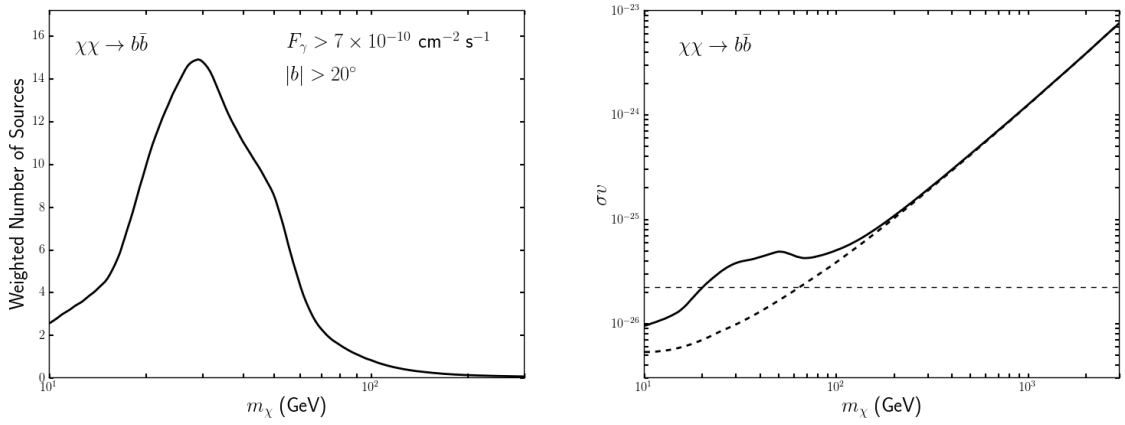

Figure 2.13: Left: The weighted number of unassociated, non-variable (variability index $<$ 80), bright ($F > 7 \times 10^{-10}$ cm^{-2}s^{-1}, $E_\gamma > 1$ GeV), high-latitude ($|b| > 20^\circ$) 3FGL sources as a function of dark matter mass (assuming annihilations to $b\bar{b}$), defined as twice the sum of the p-values for all of the candidate sources under consideration. Right: The 95% upper limit on the dark matter annihilation cross section derived from this source population. The dashed line represents the constraint that would have been derived if zero subhalo candidates had been observed. For high values of the dark matter mass, the weighted number of sources is only slightly greater than zero, and these two lines are almost identical. For lower masses, in contrast, many subhalo candidates exist and the resulting constraint is somewhat weaker.

In the right frame of fig. 2.13, we plot as a solid line the 95% upper limit on the dark matter annihilation cross section derived from this source population. This result is obtained by calculating the Poisson errors around the weighted number of sources shown in the left frame. In particular, we first calculate the 95% upper limit on the average number of subhalos $n_{\rm ul}$ detected via

$$\sum_{k=0}^{n} \frac{n_{\rm ul}^k e^{-n_{\rm ul}}}{k!} = 0.05 \ , \tag{2.9}$$

i.e., if $n_{\rm ul}$ is the average number of subhalos detected (using Poisson statistics), then there is a 5% chance to observe n or less subhalos, where n is the weighted number of subhalos calculated in the left frame of fig. 2.13 [187]. We then translate this upper limit on the average number of detected subhalos to an upper limit on the dark matter annihilation cross section $\langle \sigma v \rangle$. The dashed line in the right frame of fig. 2.13 represents the constraint that would have been derived if zero subhalo candidates had been observed. For high values of the dark matter mass, the weighted number of sources is only slightly greater than zero, and these two lines are almost identical. For lower masses, in contrast, many subhalo candidates exist and the resulting constraint is somewhat weaker.

In the left frame of fig. 2.14, we show this constraint as derived for a variety of dark matter annihilation channels ($\tau^+\tau^-$, W^+W^-, ZZ, $b\bar{b}$, $c\bar{c}$). We do not consider annihilations to e^+e^-, $\mu^+\mu^-$, as these final states are more strongly constrained by cosmic ray positron measurements [188] than by gamma-ray observations. In the right frame of this figure, we compare the constraints presented in this paper to those derived from gamma-ray observations of dwarf spheroidal galaxies [135] (see also, ref. [167]), the Galactic Center (assuming an NFW halo profile) [136], the extragalactic gamma-ray background (assuming a reference substructure model, and taking the less conservative "sensitivity reach" approach) [137] (see also, ref. [168]), and the Large Magellanic Cloud [138]. The constraints presented here are comparably stringent to those derived from these other observations, and are complementary due to the differing systematic uncertainties involved.

We also show in the right frame of fig. 2.14 the region of parameter space that is able

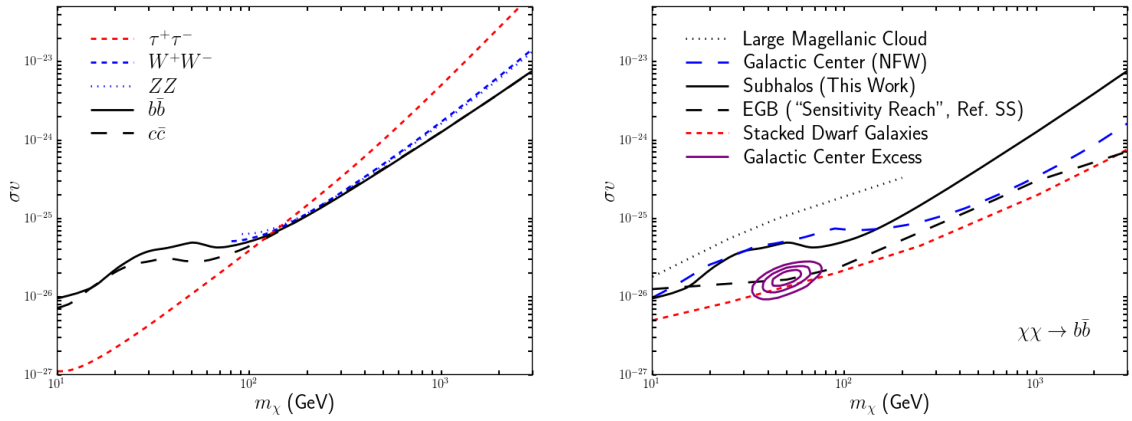

Figure 2.14: Left: The 95% upper limit on the dark matter annihilation cross section, for a variety of annihilation channels. Right: A comparison of the limit presented here to those derived from gamma-ray observations of dwarf spheroidal galaxies [135], the Galactic Center [136], the extragalactic gamma-ray background [137], and the Large Magellanic Cloud [138]. Also shown is the region of parameter space that is able to account for the gamma-ray excess observed from the region surrounding the Galactic Center [126, 139–144], as presented in refs. [127, 145] (assuming a local dark matter density of 0.4 GeV/cm^3 and a scale radius for the Milky Way's halo profile of 20 kpc).

to account for the gamma-ray excess observed from the region surrounding the Galactic Center [126, 139–144], as presented in refs. [127, 145]. This region assumes a local dark matter density of 0.4 GeV/cm^3 and a scale radius for the Milky Way's halo profile of 20 kpc. Varying these quantities within their current uncertainties can allow this region to shift upward or downward by an additional factor of a few. It is interesting to note that if the Galactic Center excess is generated by annihilating dark matter, then we expect that a few of our dark matter subhalo candidate sources should, in fact, be dark matter subhalos.

2.8 Summary and Prospects

In the standard cold dark matter paradigm, the dark matter halo of the Milky Way is predicted to contain a very large number of smaller subhalos. If the dark matter consists of weak-scale annihilating particles, the most massive and nearby of these subhalos could ap-

pear as gamma-ray sources without counterparts at other wavelengths. In this paper, we have studied the 992 unassociated gamma-ray sources contained in the Fermi Collaboration's Third Source Catalog (3FGL), in an attempt to constrain the number of these sources that could be dark matter subhalos. From this information, we have derived constraints on the dark matter annihilation cross section that are comparably stringent to those based on gamma-ray observations of dwarf spheroidal galaxies, the Galactic Center, and the extragalactic gamma-ray background.

We also present in this paper a list of 20 sources which we consider to be promising dark matter subhalo candidates. These sources are each quite bright ($F_\gamma > 7 \times 10^{-10}$ cm^{-2} s^{-1}, $E_\gamma > 1$ GeV), are located far away from the Galactic Plane ($|b| > 20^\circ$), show no signs of variability (variability index < 80), and exhibit a spectral shape that is compatible with that predicted from annihilating dark matter particles. The majority of these subhalo candidate sources are best-fit by dark matter particles with masses in the range of $\sim$20-50 GeV (assuming annihilations to $b\bar{b}$), similar to that favored to explain the previously reported Galactic Center gamma-ray excess [126, 127, 139–145]. Gamma-ray pulsars are known to exhibit similar spectra, however, making it difficult to determine whether these sources are dark matter subhalos or radio-faint gamma-ray pulsars.

We note that of the 117 high-confidence gamma-ray pulsars described in the Second Fermi-LAT Pulsar Catalog [189], 36 have pulsations that were first identified in gamma-rays (as opposed to in radio or other wavelengths). Each of these sources has been studied with deep radio observations [190–192], yielding several detections [193–195].[9] The fact that dozens of gamma-ray pulsars have not yet been detected at other wavelengths, however, leads us to expect that some of Fermi's unassociated sources could be radio-quiet pulsars, whose gamma-ray pulsations have thus far gone undetected (perhaps due to weak pulsation and/or broad pulse profiles). Deeper multi-wavelength observations and further searches for gamma-ray pulsations will be essential if we are to identify the nature of these intriguing

[9]For an updated list, see `https://confluence.slac.stanford.edu/display/GLAMCOG/Public+List+of+LAT-Detected+Gamma-Ray+Pulsars`.

sources.

We also report 3.4σ (global) evidence of spatial extension from the bright, high-latitude subhalo candidate source 3FGL J2212.5+0703. If the significance of this extension continues to increase as Fermi collects more data, and no multi-wavelength counterparts are identified, it would strengthen the case that this source could be a dark matter subhalo, rather than a pulsar or other point-like gamma-ray source. We did not find any unexpected significant extension in any of the other 252 associated or 17 unassociated sources at high latitute ($|b| > 20^{\circ}$) and in the same flux range as the bright, unassociated sources considered ($F_{\gamma} = (1.0 - 4.23) \times 10^{-9}$ cm^{-2} s^{-1} ($E_{\gamma} > 1$ GeV)—except for 3FGL J0455.7-4617. In future work we intend to simulate the radio sources close to 3FGL J2212.5+0703 and 3FGL J0455.7-4617 in gamma-rays, to see if the detected extension could be due to a superposition of these possible background sources. We also will determine the effect of the diffuse and isotropic backgrounds on observing extension from point sources by simulating many point sources in blank sky locations.

Chapter 3

NEUTRINO INTERACTING DARK MATTER

This chapter is based on my work with Seyda Ipek, David McKeen, and Ann Nelson in ref. [196].

3.1 Introduction

Structure formation involves a competition between gravity, which causes density inhomogeneities to grow, and pressure, which resists gravitational collapse. In general, in the early Universe when the temperature was extremely high, the dark matter was in thermal equilibrium with the relativistic plasma composed of photons, neutrinos, and other Standard Model (SM) particles, via non-gravitational interactions that are typically assumed to be present. After the temperature drops below the dark matter mass, the dark matter abundance eventually falls out of chemical equilibrium, fixing its (comoving) number density.

The dark matter will also fall out of kinetic equilibrium (which is based on the rate of reactions which allow momentum exchange with the plasma, as opposed to chemical equilibrium which is based on the rate of number-changing reactions). This happens at a decoupling temperature $T_{\rm d}$ which can be roughly estimated by determining when the rate for the dark matter momentum to appreciably change via scattering falls below the expansion rate of the Universe. For non-relativistic dark matter, while in kinetic equilibrium at temperature T, the dark matter has momentum of order $\sqrt{m_\chi T}$ where m_χ is its mass. After N scatterings on the components of the relativistic plasma (which carry momentum T), the change in dark matter momentum is typically about $\sqrt{N}T$. For this change to be comparable to the dark matter momentum itself implies that $N \sim m_\chi/T$. The rate for N scatterings is $\Gamma = n_r\sigma/N \sim (T\, n_r\sigma)/m_\chi$ where $n_r \propto T^3$ is the plasma (radiation)

number density and σ is the scattering cross section. The cross section for scattering in a relativistic plasma scales as $\sigma = T^2/\Lambda^4$ where Λ is the scale of the operator mediating the interaction. The decoupling temperature is found when $\Gamma = H \sim T^2/M_{\rm Pl}$ where H is the Hubble rate and $M_{\rm Pl}$ is the Planck mass. Solving for the decoupling temperature gives the scaling $T_{\rm d} \sim \Lambda(m_\chi/M_{\rm Pl})^{1/4}$. This expression captures the intuitive expectation that as the interaction strength increases (i.e. as Λ decreases), the dark matter stays in kinetic equilibrium with the plasma longer, and $T_{\rm d}$ decreases. Additionally as the mass of the dark matter particle increases, the harder it is to keep it in kinetic equilibrium, and so the its decoupling temperature will be larger.

The growth of dark matter perturbations on scales smaller than the horizon at $T > T_{\rm d}$ is suppressed by the finite pressure of the coupled dark matter-plasma gas. For $T < T_{\rm d}$, the dark matter pressure drops to zero and density perturbations on scales of order the horizon size at $T = T_{\rm d}$ and smaller can grow unimpeded. Because the (comoving) dark matter number density remains a constant, and since we know the present dark matter mass density, the lower bound on the size of unsuppressed dark matter structure formation can be expressed as a lower bound on the mass of gravitationally bound dark matter objects today, $M_{\rm cutoff}$. As we will see in sec. 3.3, this cutoff can be related to the decoupling temperature via $M_{\rm cutoff} \sim 10^8 M_\odot (\text{keV}/T_{\rm d})^3$, where $M_\odot \simeq 2 \times 10^{30}$ kg is the mass of the Sun.

Several ways to change the vanilla cold dark matter paradigm have been suggested in order to suppress the formation of structure on small scales, including: (i) the dark matter could be warmer [80, 81], (ii) the dark matter could self-interact [82–85], or (iii) the dark matter could stay in thermal equilibrium with radiation to lower temperatures than typically expected. To realize option (iii), the dark matter must interact strongly with the components of the relativistic plasma, either photons, neutrinos, or dark radiation. These interactions with the relativistic plasma allow the dark matter to feel an additional pressure that resists gravitational collapse and therefore suppresses the formation of structure. The use of stronger-than-expected interactions of dark matter with neutrinos to solve one small scale structure problem in particular, the missing satellites problem, has long been

recognized [87, 197–201].

Strong dark matter-neutrino interactions keep the dark matter in kinetic equilibrium longer, lowering $T_{\rm d}$ which increases $M_{\rm cutoff}$, offering a solution to the missing satellites problem by suppressing the formation of smaller halos. Of course, $M_{\rm cutoff}$ must be chosen to be consistent with observations of halo masses. An analysis of satellite galaxies indicates that the mass of their surrounding dark matter halos before accretion onto the Milky Way was around $M_{\rm halo} \sim 10^9 M_\odot$ [202]. Measurements of the Lyman-α absorption lines in the spectra of distant quasars due to the presence of clumps of intergalactic neutral hydrogen (the "Lyman-α forest") indicate that the halos with $M_{\rm halo} \sim 3 \times 10^8 M_\odot$ exist [203]. Similarly, dark matter substructure can be observed using gravitational lensing, with the smallest structures observed having $M_{\rm halo} \sim 1 \times 10^8 M_\odot$ [204, 205]. Since tidal disruption could cause these observed halo masses to be smaller than the original halo, and since a value for $M_{\rm cutoff} < M_{\rm halo}$ is certainly allowed, in this chapter we consider models with $M_{\rm cutoff}$ in the range $10^7 M_\odot - 10^9 M_\odot$. This range requires a decoupling temperature $T_{\rm d} \sim$ keV in order to solve the missing satellites problem. The scaling of $T_{\rm d}$ implies $(\Lambda^4 m_\chi)^{1/5} \sim 50$ MeV. Therefore, in this scenario the dark matter mass must be on the order of tens of MeV. We note that the standard weakly interacting massive particle (WIMP) cold dark matter scenario with $\Lambda \sim m_\chi \sim 100$ GeV leads to a decoupling temperature around 10 MeV and hence $M_{\rm cutoff} \ll M_\odot$ [206–208], which is too small to address the missing satellites problem.

In this chapter we consider a dark matter candidate that couples to a heavy sterile neutrino through a dark sector mediator. Dark matter-neutrino interactions are induced by neutrino mixing. We focus on the particle physics and astrophysical constraints on these interactions, and also describe in detail the effects of strong dark matter-neutrino interactions on structure formation. We will spend most of our time determining the impact of strong dark matter-neutrino interactions on the missing satellites problem, but we address the core vs. cusp and too big to fail problems briefly. The outline of this chapter is as follows. In sec. 3.2, we build a model of dark matter that interacts strongly enough with neutrinos in order to obtain a cutoff mass in the range $10^7 M_\odot - 10^9 M_\odot$ and we examine the constraints

on it. Section 3.3 contains a detailed calculation of the cutoff mass in the model. Effects on supernovae are especially interesting and we examine them in this model in sec. 3.4. In sec. 3.5 we discuss some possible tests of the model and we provide a summary and outlook in sec. 3.6.

3.2 The Dark Matter Model

3.2.1 Ingredients and basics

Interactions between neutrinos and SM gauge singlets, such as dark matter, can be safely generated through the "neutrino portal." In this scenario, couplings of the SM to dark matter (denoted by the field χ) occur through the operator $H\ell$, where H is the Higgs doublet and ℓ is a lepton doublet containing a neutrino and a charged lepton. An effective 4-Fermi interaction between neutrinos and dark matter can be generated that looks schematically like $(H\ell)^2\,\chi^2$. At the renormalizable level, this higher dimensional operator arises due to the exchange of a mediator that is either neutral or charged under the symmetry that is typically invoked to keep the dark matter stable. If the mediator is neutral, then exchange of this mediator also leads to neutrino and dark matter self-interactions. To focus primarily on dark matter-neutrino interactions, we study the case where the mediator is also charged under the dark matter stabilization symmetry.

In light of the discussion above, we introduce a complex scalar, ϕ, and a Dirac fermion, χ, which are oppositely charged under a global, conserved $\mathrm{U}(1)_\mathrm{d}$ that acts as the dark matter stabilization symmetry. The SM fields are all neutral with respect to this $\mathrm{U}(1)_\mathrm{d}$. The lighter of ϕ and χ is therefore stable and is our dark matter candidate. For definiteness, and because the opposite situation gives qualitatively the same results, we focus on the situation where the dark matter is fermionic with χ lighter than ϕ.

Additionally, we give ϕ lepton number -1 so that we can generate an effective dark matter-neutrino coupling through the operator $\phi\bar{\chi}\nu$ without breaking lepton number. The other ingredients in the model are a pair of left-handed Weyl fermions, N_1 and N_2, with

lepton number -1 and $+1$ respectively, that are SM gauge singlets, i.e. sterile neutrinos.

We assume that lepton number is conserved in interactions involving N_1 and N_2. The observed masses of the light neutrinos could be of the lepton-number violating Majorana type, arising from other lepton-number–violating interactions at a high scale, or Dirac. Although Dirac neutrino masses can easily be made consistent with our model, for definiteness we will assume the tiny observed masses are Majorana, arising e.g. through a standard seesaw scenario. Below the seesaw scale, the terms in the Lagrangian relevant for the neutrino masses are given by

$$-\mathcal{L}_{\rm m} = \frac{m_{ij}}{\langle H\rangle^2} H\ell_i H\ell_j + M N_1 N_2 + \lambda_i N_1 H \ell_i + \text{h.c.}, \tag{3.1}$$

where $i, j = e, \mu, \tau$ are lepton flavor indices and H is the Higgs doublet. Electroweak and Lorentz indices have been suppressed. m_{ij} is the effective Majorana mass matrix for the active neutrinos which can be generated at a very high scale by interactions that violate lepton number, the details of which are irrelevant for us. We assume that each of the entries in m is much smaller than M.

The interaction of the sterile neutrinos with the dark matter and mediator is given by

$$-\mathcal{L}_{\rm int} = \left(y_1 \phi^* N_1 + y_2 \phi N_2\right) \chi_L + \text{h.c.}, \tag{3.2}$$

We assume that the couplings of the right-handed component of χ can be ignored compared to those of the left-handed component—reversing or relaxing this assumption does not change any of the physics we are interested in.

After electroweak symmetry breaking, the Higgs field gets a vacuum expectation value,

$\langle H \rangle \equiv v = 174$ GeV, which leads, in the basis (ν_i, N_1^*, N_2), to the neutrino mass matrix,

$$\begin{pmatrix} m_{ij} & \lambda_j v & 0 \\ \lambda_i v & 0 & M \\ 0 & M & 0 \end{pmatrix}. \tag{3.3}$$

N_1^* pairs up with

$$\hat{\nu}_4 = \frac{M N_2 + \sum_i \lambda_i v \nu_i}{\sqrt{M^2 + \sum_i \lambda_i^2 v^2}} \tag{3.4}$$

to form a Dirac fermion $\hat{N} = (\hat{\nu}_4, N_1^*)^{\mathrm{T}}$ with mass $m_4 = \sqrt{M^2 + \sum_i \lambda_i^2 v^2}$. To avoid limits on the number of neutrino species present during the time of neutrino decoupling from measurements of the CMB [209] as well as from big bang nucleosynthesis (BBN) [210], we take $m_4 > 10$ MeV. The orthogonal linear combinations of ν_i and N_2 furnish three Majorana neutrinos with masses $m_{1,2,3}$ which are extremely small compared to m_4, at most $\mathcal{O}(0.5 \text{ eV})$. We write the relationship between the mass eigenstates and the flavor eigenstates explicitly using the unitary matrix U that diagonalizes the mass matrix,

$$\nu_i = U_{ij} \hat{\nu}_j, \tag{3.5}$$

with $i = e, \mu, \tau, N$ (defining $\nu_N \equiv N_2$) and $j = 1, 2, 3, 4$.

The mediator ϕ decays to $\bar{\chi}$ and antineutrinos through (3.2). The rate for this is

$$\Gamma_{\phi \to \bar{\nu} \bar{\chi}} = \sum_i |U_{Ni}|^2 \frac{y_2^2 m_\phi}{16\pi}, \tag{3.6}$$

where the sum runs over kinematically allowed neutrinos, and we neglect the light neutrino masses and m_χ. We will be most interested in the case where the heavy neutrino can decay

invisibly to $\chi\bar{\chi}$ plus a light neutrino through an intermediate ϕ with a rate,

$$\Gamma_{\hat{N}\to\nu\chi\bar{\chi}} = \frac{\left(y_1^2 + |U_{N4}|^2 y_2^2\right) m_4}{32\pi} \times \begin{cases} 1 & \text{if } m_\phi \ll m_4 \\ \left(1 - |U_{N4}|^2\right) \frac{y_2^2}{192\pi^2} \left(\frac{m_4}{m_\phi}\right)^4 & \text{if } m_\phi \gg m_4, \end{cases} \tag{3.7}$$

where we have ignored m_χ. As long as this is kinematically allowed ($m_4 > 2m_\chi$, since the light neutrino masses are negligible) it is the dominant decay channel for the heavy neutrino. The heavy neutrino can also decay visibly through the weak neutral current. The rate for the decay to $\nu e^+ e^-$, for example, is

$$\Gamma_{\hat{N}\to\nu e^+ e^-} = \left(1 - |U_{N4}|^2\right) \frac{G_F^2 m_4^5}{192\pi^3}. \tag{3.8}$$

In the phenomenologically interesting region $G_F m_4^2, G_F m_\phi^2 \ll 1$, so the visible decays of the heavy neutrino are highly suppressed.

We will be particularly interested in the cross section for the light neutrinos to scatter on dark matter at rest, through diagrams like that shown in fig. 3.1. Defining $\sigma_{\hat{\nu}_i\chi}$ as the cross section for the ith neutrino mass eigenstate to scatter, $\hat{\nu}_i\chi \to \sum_{j=1}^3 \hat{\nu}_j\chi$, we have

$$\sigma_{\hat{\nu}_i\chi} = \frac{|U_{Ni}|^2}{|U_{e4}|^2 + |U_{\mu 4}|^2 + |U_{\tau 4}|^2} \sigma_{\nu\chi}, \quad \sigma_{\nu\chi} = \sum_{i=1}^3 \sigma_{\hat{\nu}_i\chi}, \tag{3.9}$$

with

$$\frac{d\sigma_{\nu\chi}}{dE'_\nu} = \frac{g^4}{32\pi} m_\chi \left\{ \frac{1}{\left(m_\phi^2 - m_\chi^2 - 2m_\chi E_\nu\right)^2 + m_\phi^2 \Gamma_\phi^2} + \frac{{E'_\nu}^2 / E_\nu^2}{\left(m_\phi^2 - m_\chi^2 + 2m_\chi E'_\nu\right)^2 + m_\phi^2 \Gamma_\phi^2} \right\}. \tag{3.10}$$

In this expression, E_ν is the initial neutrino energy and E'_ν is the final neutrino energy which is in the range $E_\nu / (1 + 2E_\nu/m_\chi) < E'_\nu < E_\nu$. We have ignored the light neutrino masses,

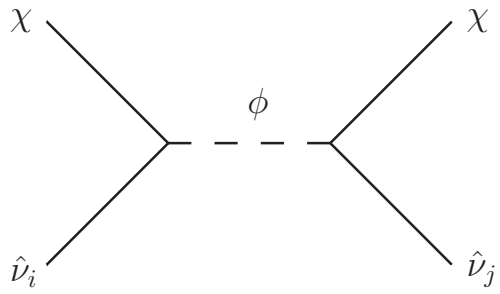

Figure 3.1: Diagram relevant for neutrino scattering on dark matter and for dark matter annihilation to neutrinos.

made use of the unitarity of U, and defined the coupling

$$g \equiv y_2 \sqrt{|U_{e4}|^2 + |U_{\mu 4}|^2 + |U_{\tau 4}|^2}. \tag{3.11}$$

Without loss of generality, we will set $g > 0$.

In the limit that the neutrino energy is small, $E_\nu \ll m_{\chi,\phi}$, the cross section becomes

$$\sigma_{\nu\chi} = \frac{g^4}{8\pi} \frac{E_\nu^2}{\left(m_\phi^2 - m_\chi^2\right)^2} = 5 \times 10^{-38}\ \mathrm{cm}^2 \left(\frac{g}{0.3}\right)^4 \left(\frac{E_\nu}{1\ \mathrm{keV}}\right)^2 \left(\frac{40\ \mathrm{MeV}}{m_\phi}\right)^4, \tag{3.12}$$

ignoring terms of order m_χ^2/m_ϕ^2 on the RHS. This form for the cross section matches on to $\sigma \sim T^2/\Lambda^4$ with $\Lambda \sim \sqrt{m_\phi^2 - m_\chi^2}/g$. As mentioned in the introduction, to have $10^7 M_\odot \lesssim M_{\mathrm{cutoff}} \lesssim 10^9 M_\odot$, we require that Λ and m_χ are $\mathcal{O}$(few $\times$ 10 MeV). In other words, we need m_χ and m_ϕ to be tens of MeV and $g \gtrsim 0.1$.

When the temperature of the Universe is larger than m_χ, the dark matter and anti-dark matter will exist in chemical equilibrium with the rest of the constituents of the plasma. As the Universe cools below m_χ, the dark matter and anti-dark matter number densities are depleted through annihilation to light neutrinos via ϕ exchange (also through diagrams like the one in fig. 3.1) which occurs with a cross section

$$\sigma_{\mathrm{ann}} v = \frac{g^4 m_\chi^2}{16\pi m_\phi^4} = 3 \times 10^{-20} \frac{\mathrm{cm}^3}{\mathrm{s}} \left(\frac{g}{0.3}\right)^4 \left(\frac{m_\chi}{20\ \mathrm{MeV}}\right)^2 \left(\frac{40\ \mathrm{MeV}}{m_\phi}\right)^4. \tag{3.13}$$

This process sets a lower limit on the dark matter mass to avoid the production of neutrinos during BBN. The requirement is that $m_\chi \gtrsim 10$ MeV [210, 211]. Additionally, for parameter values motivated by small scale structure considerations, this annihilation cross section is too large for the dark matter to be a thermal relic. We assume that its relic density is set by a primordial dark matter–anti-dark matter asymmetry. Whether this asymmetry is connected to the baryon asymmetry is beyond the scope of this work.

There are also constraints on the strength of the dark matter-neutrino interaction from measurements of the Lyman-α forest [212] as well as the CMB [213, 214], which again imply that the dark matter must have a mass greater than about 10 MeV.

To determine whether $g \gtrsim 0.1$ and $m_{\chi,\phi} \sim$ few $\times$ 10 MeV are feasible requires examining the constraints on $|U_{e4}|$, $|U_{\mu 4}|$, and $|U_{\tau 4}|$. We do this in the next section. We assume that $m_4 > 2m_\chi$, so that the heavy neutrino decays invisibly.

3.2.2 Neutrino mixing matrix elements

Below, we determine what values of the elements of the neutrino mixing matrix, U, are allowed by data from lepton and meson decays and neutrino oscillation experiments. We pay particular attention to $|U_{e4}|$, $|U_{\mu 4}|$, and $|U_{\tau 4}|$ since they directly enter the cross section relevant for keeping dark matter in thermal equilibrium with the neutrinos. The constraints on these matrix elements for the case of an additional, heavy, invisibly decaying neutrino are not well organized and not always correctly treated in the literature. We collect these constraints and show the limits on these matrix elements from our analysis in fig. 3.2. We defer discussion of constraints from supernovae to sec. 3.4.

Limits on $|U_{e4}|$, $|U_{\mu 4}|$, and $|U_{\tau 4}|$ from particle decays

We now examine the existing limits on $|U_{e4}|$, $|U_{\mu 4}|$, and $|U_{\tau 4}|$ in the case of an invisibly decaying heavy neutrino with mass above around 10 MeV that can be derived from meson and lepton decays.

We first focus on decays of a meson M to a lepton ℓ and neutrino mass eigenstate $\hat{\nu}_i$, $M^+ \to \ell^+ \hat{\nu}_i$. Since the heavy neutrino decays invisibly, all final state neutrino mass eigenstates result in the same signal, ℓ^+ and missing energy, up to a difference in the energy of the ℓ^+. The light neutrino masses can all be neglected, while the heavy neutrino mass must be retained. The decay rate to light neutrinos is

$$\Gamma_{M^+ \to \ell^+ \hat{\nu}_{1,2,3}} = \sum_{i=1}^{3} |U_{\ell i}|^2 \, \Gamma^{\rm SM}_{M^+ \to \ell^+} = \left(1 - |U_{\ell 4}|^2\right) \Gamma^{\rm SM}_{M^+ \to \ell^+} \tag{3.14}$$

and the rate to the heavy neutrino is

$$\Gamma_{M^+ \to \ell^+ \hat{\nu}_4} = |U_{\ell 4}|^2 \, \rho_{M\ell}\left(m_4\right) \Gamma^{\rm SM}_{M^+ \to \ell^+}. \tag{3.15}$$

$\Gamma^{\rm SM}_{M^+ \to \ell^+}$ is the rate for this process as calculated in the SM for a massless neutrino. $\rho_{M\ell}\left(m_4\right)$ is a factor that reflects the reduced phase space available as well as possible enhancement to helicity-suppressed decays with $\rho_{M\ell}\left(m_4 = 0\right) = 1$ and $\rho_{M\ell}\left(m_4 \geq m_M - m_\ell\right) = 0$. There are therefore two signatures of a heavy neutrino in this decay: (i) a change in the total rate for $M \to \ell$ from the SM expectation and (ii) if kinematically allowed, a peak in the ℓ energy spectrum at $(m_M^2 + m_\ell^2 - m_4^2)/2m_M$ in the M rest frame.

Decays with more than two particles in the final state, such as muon decay, leptonic τ decays, and semileptonic kaon decays, are modified analogously, with a straightforward adjustment of the phase space and the possible inclusion of a second $|U_{\ell 4}|$ if two neutrinos are in the final state. We now discuss the available data.

Peak searches in $\pi \to e\nu$ [215, 216] strongly constrain $|U_{e4}|$ while searches for peaks in $\pi \to \mu\nu$ [217], and $K \to \mu\nu$ [218, 219] similarly limit $|U_{\mu 4}|$. We show these limits in fig. 3.2.

Limits on $|U_{e4}|$ and $|U_{\mu 4}|$ can be obtained by comparing $\Gamma_{\pi \to e\nu}$ to $\Gamma_{\pi \to \mu\nu}$. Defining

$$R = \left(\frac{\Gamma_{\pi \to e\nu}}{\Gamma_{\pi \to \mu\nu}}\right)_{\rm exp} \Bigg/ \left(\frac{\Gamma_{\pi \to e\nu}}{\Gamma_{\pi \to \mu\nu}}\right)_{\rm SM} = \frac{1 + |U_{e4}|^2 \left[\rho_{\pi e}\left(m_4\right) - 1\right]}{1 + |U_{\mu 4}|^2 \left[\rho_{\pi \mu}\left(m_4\right) - 1\right]}, \tag{3.16}$$

current data [220, 221] and SM prediction [222] gives $R = 0.996 \pm 0.003$. This is particularly constraining on $|U_{e4}|$ since $\pi \to e\hat{\nu}_4$ is not as helicity-suppressed as the decay to light neutrinos. In fig. 3.2 we show the limit that R implies on $|U_{e4}|$ if we assume that $|U_{\mu 4}| = 0$ which gives a conservative limit for $m_4 < m_\pi$.

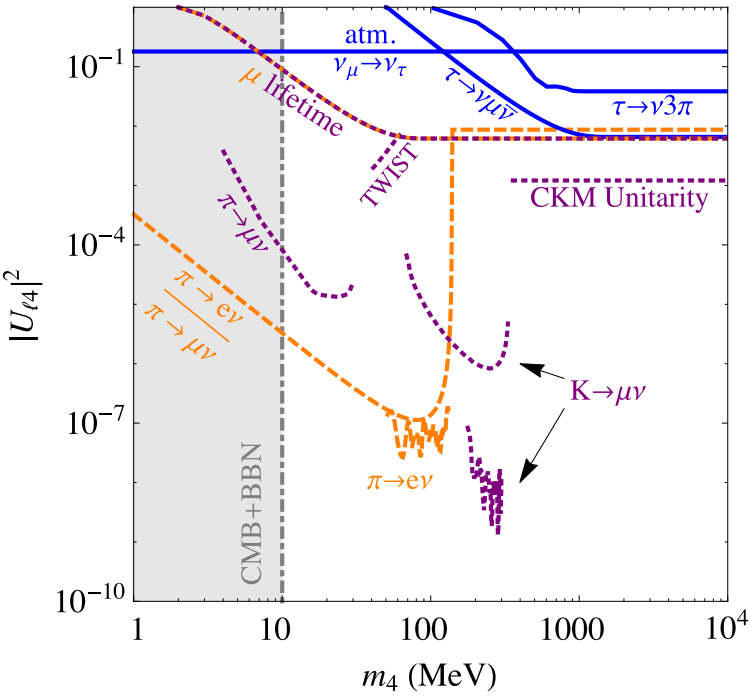

Figure 3.2: 90% C.L. upper limits on $|U_{\ell 4}|^2$, $\ell = e, \mu, \tau$, as functions of the heavy neutrino mass m_4. Limits on $|U_{e4}|^2$ (dashed, orange) come from searches in $\pi \to e\nu$ [215, 216], the ratio of $\Gamma(\pi \to e\nu)/\Gamma(\pi \to \mu\nu)$ [220–222] and the measurement of the muon lifetime [223]. $|U_{\mu 4}|^2$ limits (dotted, purple) are derived from peak searches in $\pi \to \mu\nu$ [217] and $K \to \mu\nu$ [218, 219], the muon lifetime measurement [223], the energy spectrum in muon decay (labeled "TWIST") [224, 225], and the unitarity of the measurements of the CKM matrix [226]. We have derived limits on $|U_{\tau 4}|^2$ (blue, solid) from the rate for $\tau \to \mu\nu\bar{\nu}$ and data from ref. [227] on $\tau \to \nu 3\pi$. We also show the limit on $|U_{\tau 4}|$ from atmospheric neutrino oscillations described in sec. 3.2.2 and the lower bound on m_4 from BBN and CMB measurements. Where rates depend on more than one $|U_{\ell 4}|$, we assume only one is dominant to produce each limit. See text for details.

Nonzero values of $|U_{e4}|$ and $|U_{\mu 4}|$ can also affect the relationship between the Fermi constant extracted from measurements of the muon lifetime, G_μ, and determinations using high energy data. In the on-shell renormalization scheme, for example, the Fermi constant

can be expressed in terms of the W and Z boson masses and the fine structure constant through

$$G_F = \frac{\pi\alpha}{\sqrt{2}\,(1 - m_W^2/m_Z^2)\,m_W^2\,(1 - \Delta r)}, \tag{3.17}$$

where $1 - \Delta r = 0.9636 \pm 0.0004$ encodes radiative corrections. The presence of a heavy neutrino with $m_4 > m_\mu - m_e$ changes the relationship between G_F measured in this way and G_μ via

$$G_\mu^2 = \left(1 - |U_{e4}|^2\right)\left(1 - |U_{\mu 4}|^2\right) G_F^2. \tag{3.18}$$

The expression when $m_4 < m_\mu - m_e$ is more complicated but straightforward. The very precise measurement of the muon lifetime [223] gives $G_\mu = (1.1663787 \pm 0.0000006) \times 10^{-5}$ GeV^{-2}. Using $m_W = 80.385 \pm 0.015$ GeV and $m_Z = 91.1876 \pm 0.0021$ GeV results in $G_F = (1.168 \pm 0.001) \times 10^{-5}$ GeV^{-2}. We use these values to set an upper limit on the larger of $|U_{e4}|$ or $|U_{\mu 4}|$, conservatively assuming that the smaller of the two can be neglected, in fig. 3.2. For $m_4 > m_\mu - m_e$, the limit is $|U_{e4}|$, $|U_{\mu 4}| < 7.9 \times 10^{-2}$ at 90% C. L.

For $m_4 < m_\mu - m_e$, the shape of the e^+ energy spectrum in μ^+ decay is modified. This spectrum was most accurately measured in [224] which was used to set a limit on $|U_{\mu 4}|$ in [225] for $m_4 > 40$ MeV which we also show in fig. 3.2, labeled as "TWIST."[1]

There is also a constraint on $|U_{\mu 4}|$ that can be derived using the unitarity of the quark mixing (CKM) matrix, V. V_{ud} is most accurately measured using superallowed nuclear beta decays. For m_4 larger than several MeV, the rates for these are proportional to

$$\left(1 - |U_{e4}|^2\right)|V_{ud}|^2\, G_F^2. \tag{3.19}$$

[1]The reason we only show the limit for $m_4 > 40$ MeV is that there is a gap in the limit on $|U_{\mu 4}|$ between the regions probed by $\pi \to \mu\nu$ and $K \to \mu\nu$, i.e. for 40 MeV $< m_4 <$ 80 MeV [225].

V_{ud} is extracted by dividing this by G_μ^2. Doing so gives [226]

$$\frac{|V_{ud}|}{\sqrt{1-|U_{\mu 4}|^2}} = 0.97425 \pm 0.00022. \tag{3.20}$$

A value of V_{us} can be extracted from $K_L \to \pi^- e^+ \nu$ decay. For $m_4 > m_{K^0} - m_{\pi^\pm} - m_e$, the rate for this is proportional to

$$\left(1-|U_{e4}|^2\right)|V_{us}|^2 G_F^2 \tag{3.21}$$

and again dividing by G_μ^2 results in [226]

$$\frac{|V_{us}|}{\sqrt{1-|U_{\mu 4}|^2}} = 0.2253^{+0.0015}_{-0.0013}. \tag{3.22}$$

Squaring then adding (3.21) and (3.22) and using the unitarity of the CKM matrix implies that

$$\frac{1-|V_{ub}|^2}{1-|U_{\mu 4}|^2} = 0.9999^{+0.0008}_{-0.0007}. \tag{3.23}$$

At this level $|V_{ub}|$ is negligible and can be ignored. Doing so, this translates into the constraint $|U_{\mu 4}| < 3.5 \times 10^{-2}$ at 90% C. L.

To find limits on $|U_{\tau 4}|$, we look at processes involving the τ neutrino such as τ decays or decays of D_s mesons. Existing searches using D_s decays for heavy neutrinos all look for visible decays of the heavy neutrino, so they are not sensitive to this scenario. Consequently, we focus on τ decays. In deriving our limits on $|U_{\tau 4}|$ below, we assume that $|U_{e4}|, |U_{\mu 4}| \ll |U_{\tau 4}|$. In this case, the total rate for τ to decay to a generic final state X plus missing energy is

$$\Gamma_{\tau \to X \nu} = \left[1 + |U_{\tau 4}|^2 \left(\rho_{\tau X}\left(m_4\right) - 1\right)\right] \Gamma^{\mathrm{SM}}_{\tau \to X}, \tag{3.24}$$

where, as before, $\rho_{\tau X}(m_4)$ is a kinematic factor that depends on the heavy neutrino mass.

Because leptonic τ decay rates are well-predicted and well-measured, they can offer meaningful constraints on $|U_{\tau 4}|$. We can use the measurements of the branching ratios for $\tau \to e\bar{\nu}\nu$ and $\tau \to \mu\bar{\nu}\nu$ of $17.83 \pm 0.04\%$ and $17.41 \pm 0.04\%$ respectively [226] along with the independently measured τ lifetime, $(290.17 \pm 0.62) \times 10^{-15}$ s [228], to determine the experimental rates,

$$\begin{aligned} \Gamma^{\rm exp}_{\tau\to e\bar{\nu}\nu} &= (4.04 \pm 0.09) \times 10^{-13}\ \text{GeV}, \\ \Gamma^{\rm exp}_{\tau\to \mu\bar{\nu}\nu} &= (3.95 \pm 0.09) \times 10^{-13}\ \text{GeV}. \end{aligned} \tag{3.25}$$

Using these with the SM expectations for these rates which take into account the error on m_τ [229],

$$\begin{aligned} \Gamma^{\rm SM}_{\tau\to e\bar{\nu}\nu} &= (4.031 \pm 0.001) \times 10^{-13}\ \text{GeV}, \\ \Gamma^{\rm SM}_{\tau\to \mu\bar{\nu}\nu} &= (3.920 \pm 0.001) \times 10^{-13}\ \text{GeV}, \end{aligned} \tag{3.26}$$

and the expression in (3.24) can limit $|U_{\tau 4}|$. The constraint from $\tau \to \mu$ decay, shown in fig. 3.2,[2] is stronger since the central value of the measured rate is further from the SM expectation than the $\tau \to e$ mode, although still in agreement. For $m_4 > m_\tau - m_\mu$ the 90% C. L. limit is $|U_{\tau 4}| < 8 \times 10^{-2}$ and weakens to $|U_{\tau 4}| < 0.4$ at $m_4 = 130$ MeV.

We can also set a limit on $|U_{\tau 4}|$ by looking for changes in the differential rates for τ decays to multiparticle final states. This procedure was undertaken by the ALEPH collaboration [227] to place an upper limit of 18.2 MeV at 95% C. L. on the mass of the τ neutrino using $\tau \to \nu 3\pi$ and $\tau \to \nu 5\pi$ decays. We use the data for the $\tau \to \nu 3\pi$ rate as a function of the three pion invariant mass from [227], modeling the $\tau \to \nu 3\pi$ decay as occurring through the chain $\tau \to \nu a_1 \to \nu\pi\rho \to \nu 3\pi$ to set a limit on $|U_{\tau 4}|$ varying m_4, also shown in fig. 3.2.

[2] Our limits on $|U_{\tau 4}|$ for a heavy neutrino that decays invisibly differ substantially from those in [230] which also considered shifts in leptonic τ decays. The main reason for this is that we consider a unitary neutrino mixing matrix whereas [230] does not [effectively making the replacement $\rho_{\tau X}(m_4) \to \rho_{\tau X}(m_4) + 1$ in (3.24)] with the consequence that our limits weaken as the heavy neutrino mass is decreased. This is to be expected for a unitary mixing matrix since the heavy neutrino becomes indistinguishable from the light neutrinos as it is made lighter. Additionally, since the presence of a heavy neutrino in the final state also affects the other decay modes, we limit the change in the leptonic *rate* itself using the branching ratio and the independent determination of the τ lifetime. In contrast [230] limited shifts of the branching ratio effectively assuming the total width was unchanged.

This limit is less strong than what we derived from $\tau \to \mu$ decays, partially due to the fact that properly modeling the 3π rate is nontrivial. Properly modeling the 5π decay mode is even more difficult but could offer an improvement in the limit due to the reduced phase space available which enhances the effects of a massive neutrino.

As mentioned above, solutions to small scale structure problems imply that $g = y_2\sqrt{\sum_\ell |U_{\ell 4}|^2} \sim 0.3$. Given the constraints outlined above, and without increasing y_2 to nonpertubative values, this is only possible to achieve with $|U_{\tau 4}| \gtrsim 0.1$. In this case $m_4 \lesssim 300$ MeV and $|U_{e4}|$, $|U_{\mu 4}| \ll |U_{\tau 4}|$. In the rest of the paper, we therefore simplify our analysis by making the approximation that $\lambda_{e,\mu} = 0$ in (3.1). In that case, $|U_{e4}| = |U_{\mu 4}| = 0$ and $U_{\tau 4} \equiv \sin\theta_\tau$ with $\theta_\tau = \tan^{-1}(-\lambda_\tau v/M)$. The light Majorana neutrinos are linear combinations of ν_e, ν_μ and $\nu_{\tau N} \equiv \cos\theta_\tau \nu_\tau - \sin\theta_\tau N_2$ while the heavy Dirac neutrino has mass $m_4 = M/\cos\theta_\tau$ and contains $\hat{\nu}_4 = \cos\theta_\tau N_2 + \sin\theta_\tau \nu_\tau$ and N_1^*.[3]

[3]The reason that we did not choose to add just a single Weyl sterile neutrino earlier is that in such a scenario, after integrating the sterile neutrino out, the light neutrino mass matrix element m_{ij} receives contributions proportional to the product of mixing angles $\theta_i\theta_j M$, where M is the sterile neutrino mass and the mixing angle between active neutrino i and the sterile neutrino is again $\theta_i \sim \lambda_i v/M$. Obtaining a mixing angle large enough to be interesting in this case requires a sterile neutrino that is too light to avoid cosmological constraints.

Constraints from neutrino oscillation experiments

In the limit that U_{e4} and $U_{\mu 4}$ are zero, we can parameterize the 4×4 matrix U using only four angles, θ_τ as defined above, θ_{12}, θ_{13}, and θ_{23},

$$U = \begin{pmatrix} 1 & 0 & 0 & 0 \\ 0 & 1 & 0 & 0 \\ 0 & 0 & c_\theta & s_\theta \\ 0 & 0 & -s_\theta & c_\theta \end{pmatrix} \begin{pmatrix} 1 & 0 & 0 & 0 \\ 0 & c_{23} & s_{23} & 0 \\ 0 & -s_{23} & c_{23} & 0 \\ 0 & 0 & 0 & 1 \end{pmatrix} \begin{pmatrix} c_{13} & 0 & s_{13} & 0 \\ 0 & 1 & 0 & 0 \\ -s_{13} & 0 & c_{13} & 0 \\ 0 & 0 & 0 & 1 \end{pmatrix} \begin{pmatrix} c_{12} & s_{12} & 0 & 0 \\ -s_{12} & c_{12} & 0 & 0 \\ 0 & 0 & 1 & 0 \\ 0 & 0 & 0 & 1 \end{pmatrix}$$

$$= \begin{pmatrix} c_{12}c_{13} & c_{13}s_{12} & s_{13} & 0 \\ -c_{23}s_{12} - c_{12}s_{13}s_{23} & c_{12}c_{23} - s_{12}s_{13}s_{23} & c_{13}s_{23} & 0 \\ -c_\theta\left(c_{12}c_{23}s_{13} - s_{12}s_{23}\right) & -c_\theta\left(c_{23}s_{12}s_{13} + c_{12}s_{23}\right) & c_\theta c_{13}c_{23} & s_\theta \\ s_\theta\left(c_{12}c_{23}s_{13} - s_{12}s_{23}\right) & s_\theta\left(c_{23}s_{12}s_{13} + c_{12}s_{23}\right) & -s_\theta c_{13}c_{23} & c_\theta \end{pmatrix}, \tag{3.27}$$

with $c_\theta \equiv \cos\theta_\tau$, $s_\theta \equiv \sin\theta_\tau$ and $c_{ij} \equiv \cos\theta_{ij}$, $s_{ij} \equiv \sin\theta_{ij}$. For simplicity, we have ignored possible CP-violating phases in the mixing matrix.

Although we have four flavors of neutrino, our analysis of existing constraints differs from existing sterile neutrino analyses because the fourth mass eigenstate is assumed to be heavier than several MeV, in order to avoid cosmological constraints from the CMB [209] and BBN [210]. As discussed above, the heavy fourth mass eigenstate is mostly comprised of sterile and tau flavors, in order to satisfy laboratory and precision electroweak constraints on electron and muon neutrino mixing with a neutral heavy lepton. Current terrestrial experiments produce either μ or e flavor neutrinos at the source, and so can only produce a linear combination of the three light mass eigenstates. Since the light mass eigenstates are comprised of all four flavors, e, μ, τ, and sterile N_2, the presence of the sterile component could affect neutrino oscillation experiments. Oscillations via the heavy neutrino are independent of the particular value of its mass since they correspond to a length

$$L = \frac{4\pi p}{\Delta m^2} \simeq \frac{4\pi p}{m_4^2} \lesssim 2.5 \times 10^{-12}\ \text{cm}\left(\frac{p}{\text{MeV}}\right), \tag{3.28}$$

where p is the momentum of the neutrinos in question, using the lower bound on the heavy neutrino mass of about 10 MeV. This length scale is far smaller than the $\sim$ km length scales relevant for neutrino experiments, therefore, the light mass differences must be given by the solar and atmospheric mass splittings as usual [231],

$$\Delta m^2_{12} = \Delta m^2_{\odot} \simeq 7.5 \times 10^{-5}\ \text{eV}^2, \quad \left|\Delta m^2_{13}\right| = \Delta m^2_{\text{atm}} \simeq 2.5 \times 10^{-3}\ \text{eV}^2, \tag{3.29}$$

where $\Delta m^2_{ij} \equiv m^2_i - m^2_j$.

We begin by noting that our assumption that U_{e4} and $U_{\mu 4}$ are negligible allows us to determine θ_{12}, θ_{13}, and θ_{23} using terrestrial neutrino experiments which are insensitive to θ_τ. Combining these measurements with solar neutrino experiments allows for possible sensitivity to θ_τ. We describe this procedure below.

In principle, one needs to account for the effect of the different interaction with matter of the sterile neutrinos [232, 233], which can be included via a potential V_{nc} in the flavor basis for the active neutrino flavors of

$$V_{\text{nc}} = -\frac{G_F}{\sqrt{2}} n_n \tag{3.30}$$

where n_n is the neutron density, with the opposite sign for antineutrinos. In matter with equal numbers of protons and neutrons and density of 2.7 g/cm^3, a length scale of 4000 km can be derived from $1/V_{\text{nc}}$, which gives an estimate of the distance scale required for matter interactions to have an important effect in the analysis of neutrino oscillations in the Earth's crust [234]. Currently, the strongest constraints on the active neutrino mixing parameters derive from experiments which are not at long enough baseline to be highly sensitive to the matter effects. However, as we point out below, a strong limit on θ_τ may be extracted from the IceCube and Super-Kamionkande experiments, due the difference in matter effects between sterile and active neutrinos as they travel through the Earth.

The best determination of U_{e3} is by the reactor experiment Daya Bay [235], which measures electron antineutrino disappearance over a distance of 1.6 km. The value of $U_{\mu 3}$ may be determined by measurements of muon neutrino and antineutrino disappearance by the

K2K [236] and MINOS experiments [237], with baselines of 250 km and 730 km, respectively. U_{e2} can be determined by the long baseline reactor experiment KamLAND [238] which has a baseline average of 180 km. Because matter effects are not highly significant at these baselines, the extraction of U_{e3}, $U_{\mu 3}$, and U_{e2} is little affected by the possible presence of a sterile component in the third mass eigenstate. These measurements of U_{e3}, $U_{\mu 3}$, and U_{e2} can be combined to give determinations of θ_{12}, θ_{13}, and θ_{23} that are independent of θ_τ, and these angles must be close to the values given by the usual three neutrino fits to data [231],

$$\theta_{12} \sim 32^\circ,\ \theta_{13} \sim 8^\circ,\ \theta_{23} \sim 40^\circ. \tag{3.31}$$

Turning now to solar neutrinos, we note that electron neutrino disappearance is mainly governed by the flavor composition of the second mass eigenstate, since we may neglect the small angle θ_{13}. High energy solar electron neutrinos are produced in the core of the sun, primarily via ^{8}B decays, and have a large effective mass from the matter interactions, larger than $\sqrt{\Delta m^2_{12}}$ but smaller than $\sqrt{|\Delta m^2_{23}|}$. These electron neutrinos are approximately an energy eigenstate of the effective Hamiltonian which includes matter interactions. Adiabatic evolution of the electron neutrinos as they exit the core causes them to exit the sun primarily as the second mass eigenstate in vacuum. Neglecting θ_{13}, the fraction of this mass eigenstate which is detected as electron neutrino is $|s_{12}|^2$, while the fraction $|c_{12}s_{23}\sin\theta_\tau|^2$ is undetectable sterile. Hence, high energy charged current electron neutrino detection from solar neutrino experiments and the solar neutral current flux [239] can be used to constrain θ_τ when combined with either the KamLAND determination of θ_{12} or with the theoretical calculation of the ^{8}B flux. Because the KamLAND experiment, while very constraining of $\sqrt{\Delta m^2_{12}}$, is not as sensitive to U_{e2}, the theoretical calculation of the ^{8}B flux currently gives the best precision on this determination. Experimentally, a combination of electron scattering and neutral current measurements are used to calibrate the flux [240, 241] and the sterile neutrino component could affect this. Since the ^{8}B flux is theoretically known to about the 15% level currently [242], we obtain a limit of $|\sin\theta_\tau| \lesssim 0.6$. This agrees with analyses of

the combined solar data and KamLAND that has shown that the probability of electron neutrino disappearance into sterile neutrinos could be substantial [243, 244].

Strong limits on θ_τ come from the change in matter effects due to mixing with the sterile neutrino. As mentioned above, the light eigenstates are made up of ν_e, ν_μ, and $\nu_{\tau N}$. In the presence of nonzero θ_τ, $\nu_{\tau N}$ has diminished weak interactions compared to ν_μ, with a potential given by $V_{\tau N} = V_{\rm nc}\cos^2\theta_\tau$. A recent search by Super-Kamiokande [245] used atmospheric neutrinos to look for $\mu \to$ sterile transitions. Because of the lack of matter effects for the sterile neutrinos, this can manifest as a change in the distribution of muon neutrino zenith angle in the detector from the standard $\mu \to \tau$ transition scenario. At 90% C.L., the limit is $|U_{\tau 4}| = |\sin\theta_\tau| < 0.42$. Similar effects were searched for in data from IceCube and DeepCore, using the language of neutrino nonstandard interactions (NSI) [246]. In NSI studies, the difference in weak interaction strength between the light flavor eigenstate $\nu_{\tau N}$ and that of ν_τ is parameterized by $\epsilon_{\tau\tau}$ with

$$\epsilon_{\tau\tau} = \frac{1}{6}\left(\frac{V_{\tau N}}{V_{\rm nc}} - 1\right) = \frac{\sin^2\theta_\tau}{6}. \tag{3.32}$$

In ref. [246], a 90% C.L. of $\epsilon_{\tau\tau} < 0.03$ from azimuthal distributions of neutrinos was found. This also translates into $|U_{\tau 4}| < 0.42$. We show this limit along with those from τ decays in fig. 3.2.

3.2.3 New couplings to the Z and Higgs

At one loop, through the diagram shown on the left in fig. 3.3, an effective coupling of dark matter to the Z boson is generated. In the limit that $m_4 \gg m_\phi$, this effective interaction is

$$\mathcal{L}_{Z\bar{\chi}\chi} = -\frac{g_{\rm w}}{\cos\theta_{\rm w}}\left(\frac{y_2 \sin 2\theta_\tau}{8\pi}\right)^2 Z_\mu \bar{\chi}_L \gamma^\mu \chi_L, \tag{3.33}$$

where $g_{\rm w}$ is the weak coupling strength and $\theta_{\rm w}$ is the weak mixing angle. This operator contributes to the invisible decay width of the Z (the rate for $Z \to$ neutrinos is unchanged

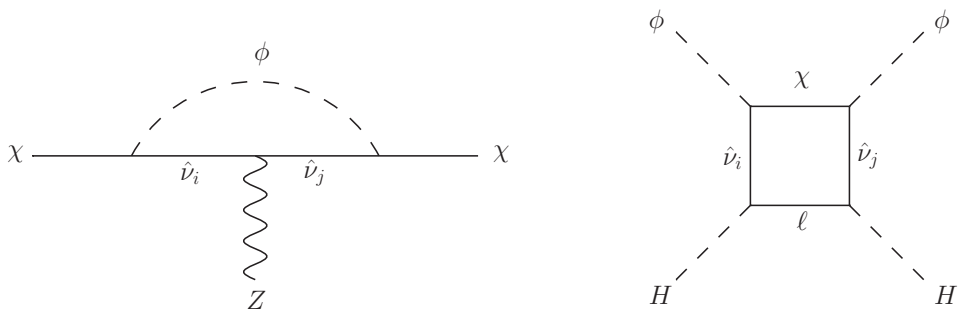

Figure 3.3: Left: one loop diagram which gives rise to an effective χ-$\bar{\chi}$-Z coupling. Right: diagram that contributes to the $|\phi|^2 |H|^2$ operator.

due to the unitarity of U for $m_4 \ll m_Z/2$[4]). The good agreement between the SM expectation for this rate and experiment offers a potential constraint on the model. The rate for $Z \to \chi\bar{\chi}$ through this operator is

$$\Gamma_{Z\to\chi\bar{\chi}} = 4.2 \times 10^{-4} \left(y_2 \sin 2\theta_\tau\right)^4 \text{ MeV}. \tag{3.34}$$

The 95% C. L. upper limit on extra contributions to the Z invisible width is 2.0 MeV [248]. This translates to a weak limit of $|y_2 \sin 2\theta_\tau| < 8.3$.

This effective $Z_\mu \bar{\chi}_L \gamma^\mu \chi_L$ interaction can lead to the scattering of dark matter on normal matter. For phenomenologically interesting values of the parameters, however, this scattering is highly suppressed: taking $y_2 = 1$ and $\theta_\tau = 0.3$, the cross section is about $10^{-7} - 10^{-6}$ times that of neutrino scattering. Because this cross section is so small, using proton beam dumps to produce the heavy neutrino, though production of $D_s \to \tau\nu_\tau$ (as used in searches for visibly decaying heavy neutrinos [249–251]), which decays to dark matter that scatters in a detector (see, e.g. [252–255]) is not promising.

We now consider interactions involving the Higgs. The operators proportional to λ_i in (3.1) will lead to contributions to the invisible width of the Higgs boson after electroweak

[4]A global fit of electroweak precision data shows a slight preference for nonzero values of $U_{\tau 4}$ if $m_4 \gtrsim 45$ GeV due to a decrease in the invisible Z width [247].

symmetry breaking, through $h \to N_1 \nu_i$. Since we ignore $\lambda_{e,\mu}$ and take $m_4 \ll m_h = 125$ GeV, the rate for this decay is

$$\Gamma_{h\to\text{inv.}} = \frac{\lambda_\tau^2}{16\pi} m_h. \tag{3.35}$$

The invisible branching ratio of the Higgs is presently limited to about 25% [256], which translates into $|\lambda_\tau| \lesssim 2 \times 10^{-2}$. This is not constraining on the model since $|\lambda_\tau| = (m_4/v)|\sin\theta_\tau|$ is less than 2×10^{-3} if $m_4 < 300$ MeV.

At one loop, as seen on the right in fig. 3.3, a logarithmically-divergent dimension-4 operator involving the scalar ϕ and the Higgs doublet is generated,

$$\mathcal{L}_{\phi H} = \lambda_{\phi H} |\phi|^2 |H|^2, \tag{3.36}$$

with

$$\lambda_{\phi H} \sim \left(\frac{y_1 \lambda_\tau}{2\pi}\right)^2 \log\left(\frac{\Lambda^2}{M^2}\right) = \frac{g^2}{4\pi^2}\left(\frac{y_1}{y_2}\right)^2 \left(\frac{m_4}{v}\right)^2 \log\left(\frac{\Lambda^2}{M^2}\right), \tag{3.37}$$

where Λ is the scale of the physics that enters to cut this contribution off. After electroweak symmetry breaking, this gives a contribution to the mass of ϕ given by $\delta m_\phi^2 = \lambda_{\phi H} v^2$. This contribution defines a lower bound on m_ϕ; obtaining a mass below this value requires some fine-tuning of this contribution against the bare value of the mass. Noting that $M \simeq m_4$ and choosing $\Lambda = 1$ TeV,

$$\delta m_\phi^2 \sim (10\text{ MeV})^2 \left(\frac{g}{0.3}\right)^2 \left(\frac{y_1/y_2}{0.5}\right)^2 \left(\frac{m_4}{100\text{ MeV}}\right)^2 \left[\log\left(\frac{1\text{ TeV}}{m_4}\right) \Big/ 10\right]. \tag{3.38}$$

Therefore, ϕ can have a mass in the tens of MeV range for a heavy neutrino with mass of $\mathcal{O}(100\text{ MeV})$ without running into any fine-tuning problems, even for a cutoff at the TeV scale.

3.3 Solving the Missing Satellites Problem

As discussed earlier, dark matter-neutrino interactions will suppress the growth of small scale dark matter density perturbations in the early Universe, helping to alleviate the missing satellites problem. This suppression of small scale structure occurs below the maximum of two different length scales for washing out structure. These two length scales have different physical origins and will be discussed in detail in this section. Since the dark matter density is known, this maximum length scale corresponds to a mass cutoff scale, $M_{\rm cutoff}$; the formation of structures with mass $< M_{\rm cutoff}$ is suppressed. These cutoff scales have been examined previously in the literature [87, 197, 198, 201, 206, 207, 257], but we reproduce them here for completeness. We also explicitly show the role of $g_{\rm eff}$ (the effective number of relativistic, bosonic degrees of freedom) in the following equations, in order to clarify discrepancies in the literature.

The first scale for washing out small scale structure is set at early times when the dark matter is in thermal equilibrium with the relativistic plasma. Since the dark matter is strongly coupled to the neutrinos at this time, it participates in acoustic oscillations along with the rest of the plasma. These oscillations wash out primordial density perturbations in the dark matter fluid. After this initial smoothing of dark matter perturbations, the Universe continues to expand and cool. Once $T \lesssim m_\chi$, the expansion of the Universe will cause the plasma density to decrease enough such that the annihilation and production scattering processes keeping dark matter in chemical equilibrium with the plasma will freeze out, ending dark matter number-changing processes. However, dark matter-neutrino elastic scattering can keep the dark matter in kinetic equilibrium even after chemical decoupling. The dark matter eventually will fall out of kinetic equilibrium once the dark matter-neutrino elastic scattering rate drops below the Hubble expansion rate of the Universe. This time when elastic scattering ceases is called kinetic decoupling. After this, the dark matter simply free-streams and washes out further small scale structure, setting another scale below which structure formation is suppressed.

In the following we discuss how dark matter-neutrino interactions can lead to a value of $M_{\rm cutoff}$ in the range of $10^7 M_\odot - 10^9 M_\odot$ which is large enough to solve the missing satellites problem. We will determine the range of interesting dark matter-neutrino coupling, g, and dark matter and mediator masses, m_χ and m_ϕ, which can achieve these cutoff mass scales.

3.3.1 Kinetic decoupling condition

Kinetic decoupling occurs when the rate for dark matter-neutrino collisions to change the dark matter momentum, $\gamma(T)$, becomes small compared to the Hubble parameter, $H(T)$. Hence the decoupling temperature, $T_{\rm d}$, can be estimated by solving

$$\gamma(T_d) = H(T_d), \tag{3.39}$$

where

$$\gamma(T) = \frac{1}{3 m_\chi T} \int_0^\infty \frac{d^3p}{(2\pi)^3} f(p/T)(1 - f(p/T)) \int_{-4p^2}^0 dt(-t) \frac{d\sigma_{\nu\chi}}{dt}. \tag{3.40}$$

Here $f(p/T) = (e^{p/T} + 1)^{-1}$ is the Fermi-Dirac distribution function describing neutrinos in the massless limit and t is the usual Mandelstam variable. This kinetic decoupling equation comes from an approximate solution to the Boltzmann equation, see [258]. An exact, though more complicated, analytical form is also available [259]. As we will soon show, in order to solve the missing satellites problem, the dark matter and neutrinos must remain in kinetic equilibrium until $T \simeq 1$ keV, which occurs after the neutrinos decouple from the photons at $T \simeq 1$ MeV. This means that the terms on the LHS of (3.39) which have to do with the neutrino-dark matter fluid, should be evaluated at the neutrino temperature, which differs from the photon temperature via $T_\nu = (4/11)^{1/3} T_\gamma$. In what follows all temperatures are photon temperatures and the factor of $(4/11)^{1/3}$ has been included when necessary.

We solve for $T_{\rm d}$ using the approximate form of the total dark matter-neutrino cross section for $E_\nu \ll m_\chi,\ m_\phi$. This is a good approximation near decoupling since at this point

$E_\nu \sim T \ll m_\chi,\ m_\phi$. Hence

$$\frac{d\sigma_{\nu\chi}}{dt} = \frac{g^4}{32\pi\left(m_\phi^2 - m_\chi^2\right)^2}. \tag{3.41}$$

Using this in (3.39), the remaining integrals can be done analytically and the decoupling temperature is given by

$$\begin{aligned} T_{\rm d} &= \left(\frac{5082}{31\pi\sqrt{5\pi}}\right)^{1/4} \left(\frac{g_{\rm eff}(T_d)^{1/8}}{M_{\rm Pl}^{1/4}}\right) \left(\frac{m_\chi^{1/4}\sqrt{m_\phi^2 - m_\chi^2}}{g}\right) \\ &= 1.6 \text{ keV } \left(\frac{g_{\rm eff}(T_{\rm d})}{3.36}\right)^{1/8} \left(\frac{m_\chi}{20 \text{ MeV}}\right)^{1/4} \left(\frac{\sqrt{m_\phi^2 - m_\chi^2}}{35 \text{ MeV}}\right) \left(\frac{g}{0.3}\right)^{-1}, \end{aligned} \tag{3.42}$$

where $g_{\rm eff}(T)$ is the effective number of relativistic, bosonic degrees of freedom at temperature T. This expression for the decoupling temperature contains the correct parametric dependence derived using simple arguments in the introduction. Note that we used the expression for the Hubble parameter during the radiation dominated period (valid down to $T \simeq 1$ eV) given by

$$H = \sqrt{\frac{4\pi^3 g_{\rm eff}(T)}{45 M_{\rm Pl}^2}} T^2. \tag{3.43}$$

3.3.2 The cutoff mass scale

There are two main processes that erase primordial density fluctuations in the dark matter fluid on small scales: (i) acoustic oscillations in the coupled, relativistic plasma of the early universe up until the time of kinetic decoupling, and (ii) free streaming of dark matter after kinetic decoupling. The larger of the two scales set by these processes determines $M_{\rm cutoff}$.

While dark matter remains in thermal equilibrium with the relativistic plasma, it is involved in the acoustic oscillations of the plasma since it couples to the neutrinos. This results in damping and oscillations in the dark matter power spectrum that appear on the scale of the horizon at kinetic decoupling, $H_{\rm d}^{-1} = a_{\rm d}\eta_{\rm d}$, where $\eta_{\rm d} = \int_0^{t_{\rm d}} dt/a(t)$ is the comoving distance a photon can travel from the beginning of the Universe until the time of kinetic

decoupling [207]. Here $a(t)$ denotes the scale factor in a Friedmann-Robertson-Walker metric and $a_{\rm d}$ is the scale factor at the time of kinetic decoupling. This smallest distance scale corresponds to a dark matter halo mass cutoff given by

$$M_{\rm ao} = \rho_\chi(T_{\rm d})\frac{4\pi}{3}(a_{\rm d}\eta_{\rm d})^3, \tag{3.44}$$

where $\rho_\chi(T)$ is the dark matter energy density (equal to its mass density for $T < T_{\rm d} \ll m_\chi$) at temperature T. Since the mass enclosed in a given volume remains the same even as that volume expands, $M_{\rm ao}$ can also be expressed in terms of the dark matter density and scale factor today as

$$M_{\rm ao} = \rho_\chi(T_0)\frac{4\pi}{3}(a_0\eta_{\rm d})^3. \tag{3.45}$$

Assuming entropy in a comoving volume is conserved from $T_{\rm d}$ until today, this becomes

$$M_{\rm ao} = 2\times 10^8 M_\odot \left(\frac{g_{\rm eff}(T_{\rm d})}{3.36}\right)^{-1/2}\left(\frac{T_{\rm d}}{\rm keV}\right)^{-3}, \tag{3.46}$$

where we used $H_0 = 67$ km/s/Mpc, $\Omega_\chi = 0.27$, $g_{\rm eff}(T_0) = 3.36$ and $T_0 = 2.7$ K.

After kinetic decoupling, the dark matter free-streams, washing out structure on scales smaller than $\ell_{\rm eq} = \pi a_{\rm eq}\int_{t_{\rm d}}^{t_{\rm eq}} dt(v_{\rm phys}/a(t))$ at the time of matter-radiation equality [206, 207]. Here $a_{\rm eq}$ is the scale factor at matter-radiation equality, $v_{\rm phys} = v/a(t)$ is the velocity of the dark matter particles, and v is their constant comoving velocity. This scale describes the distance that dark matter free-streams from $T_{\rm d}$ to $T_{\rm eq} \simeq 1$ eV. Up until $T_{\rm eq}$ this scale grows as $\ln T$ and the growth after $T_{\rm eq}$, proportional to $T^{-1/3}$, has been neglected. Evaluating ℓ today we find

$$\ell_0 = \left(\frac{a_0}{a_{\rm d}}\right)\left(\frac{v}{a_{\rm d}}\right)\frac{\pi}{H_{\rm d}}\ln\left[\frac{g_{\rm eff}(T_{\rm d})^{1/3}T_{\rm d}}{g_{\rm eff}(T_{\rm eq})^{1/3}T_{\rm eq}}\right]. \tag{3.47}$$

Approximating the dark matter velocity at the time of decoupling as $v/a_{\rm d} = \sqrt{(4/11)^{1/3}T_{\rm d}/m_\chi}$,

the cutoff mass scale due to dark matter free-streaming is given by

$$\begin{aligned} M_{\rm fs} &= \rho_\chi(T_0)\frac{4\pi}{3}\ell_0^3 \\ &= 3\times 10^5 M_\odot \left(\frac{g_{\rm eff}(T_{\rm d})}{3.36}\right)^{-1/2}\left(\frac{m_\chi}{20\ {\rm MeV}}\right)^{-3/2}\left(\frac{T_{\rm d}}{\rm keV}\right)^{-3/2} \\ &\qquad \times\left\{1+\ln\left[\left(\frac{g_{\rm eff}(T_{\rm d})}{3.36}\right)\left(\frac{T_{\rm d}}{\rm keV}\right)\right]/6.0\right\}^3 . \end{aligned} \tag{3.48}$$

The smallest mass object formed by dark matter is the largest of $M_{\rm ao}$ and $M_{\rm fs}$. Comparing (3.46) and (3.48), we see that in order to obtain values of $M_{\rm cutoff}$ in the range $10^7 - 10^9 M_\odot$ with $m_{\chi,\phi} \sim$ few $\times$ 10 MeV, $T_{\rm d} \sim$ keV is needed and acoustic oscillations set the cutoff scale. Hence, combining (3.42) and (3.46), we have that

$$M_{\rm cutoff} = 4\times 10^7\ M_\odot \left(\frac{g_{\rm eff}(T_{\rm d})}{3.36}\right)^{-7/8}\left(\frac{g}{0.3}\right)^3\left(\frac{m_\chi}{20\ {\rm MeV}}\right)^{-3/4}\left(\frac{\sqrt{m_\phi^2-m_\chi^2}}{35\ {\rm MeV}}\right)^{-3} . \tag{3.49}$$

The left panel of fig. 3.4 shows the cutoff scale varying m_χ and m_ϕ. We take $g = 0.42$ to be as large as allowed by limits on $|U_{\tau 4}|$ from τ decays and neutrino oscillation experiments with $y_2 = 1$. On the right panel we display the coupling g required to obtain $M_{\rm cutoff} = 10^7 M_\odot$, $10^8 M_\odot$, and $10^9 M_\odot$ as a function of m_χ for $m_\phi = 20$ and 40 MeV. We set $y_2 = 1$ and show the resulting upper limit on $g = y_2\,|U_{\tau 4}|$ from the limit $|U_{\tau 4}| < 0.42$ as found in sec. 3.2.2.

Finally, we note that the effect of dark matter-photon interactions on the nonlinear structure formation of satellite galaxies in a Milky Way sized galaxy has been simulated in [86]. The effects of dark matter-photon interactions on structure formation should be very similar to the effects of dark matter-neutrino interactions since they both suppress structure formation on small scales due to acoustic oscillations. They find that for a constant dark matter-photon cross section, $\sigma_{{\rm DM}-\gamma} \gtrsim 7\times 10^{-35}$ cm^2 for $m_\chi = 20$ MeV is ruled out at the 2-sigma level since the dark matter-photon interactions would wash out too much structure to be consistent with the number of satellite galaxies that we observe in the Milky Way. In our scenario, the dark matter-neutrino cross section is not a constant, but at

the time of kinetic decoupling when the value of the dark matter-neutrino cross section is most important for affecting small scale structure, we have that for typical parameters, $\sigma \simeq g^4(3T_\mathrm{d})^2/(8\pi(m_\phi^2 - m_\chi^2)^2) \simeq 2 \times 10^{-36}$ cm^2, which is within the bounds of ref. [86], but still large enough to significantly decrease structure formation on small scales.

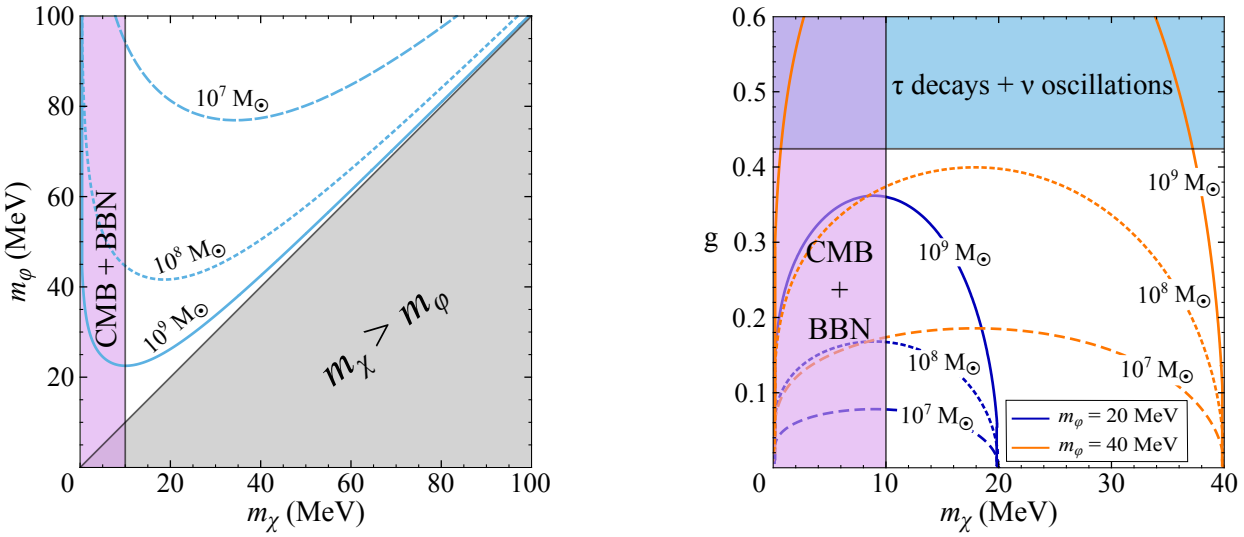

Figure 3.4: Left: Values of m_ϕ required for $M_\mathrm{cutoff} = 10^7 M_\odot$ (dashed), $10^8 M_\odot$ (dotted), and $10^9 M_\odot$ (solid) as functions of m_χ. To fix $g = y_2 |U_{\tau 4}|$, we set $y_2 = 1$ and take the largest value of $|U_{\tau 4}|$ allowed by τ decays and neutrino oscillation experiments, 0.42, as shown in fig. 3.2. The gray shaded region on the bottom-right corresponds to the unphysical situation where the mediator is lighter than the dark matter. Right: the coupling g required for $M_\mathrm{cutoff} = 10^7 M_\odot$, $10^8 M_\odot$, and $10^9 M_\odot$ varying the dark matter mass for $m_\phi = 20$ and 40 MeV. The upper limit on $g = y_2 |U_{\tau 4}|$ of 0.42 (c.f. sec. 3.2.2) assuming $y_2 = 1$ is also shown. In both plots we show the lower limit on the dark matter mass from observations of the CMB and BBN.

We also note that in simulations of a model in which dark matter interacts with dark radiation [260], small galaxies form later and have lower central densities than in standard cold dark matter. These generic results should also hold for a model of dark matter-neutrino interactions.

3.4 Implications for Supernovae

Supernovae (SNe), being abundant sources of neutrinos, can offer interesting information about strong dark matter-neutrino interactions. In this section we examine the effects of such interactions on the properties of SNe neutrinos. We also comment on how the addition of strong dark matter-neutrino interactions to SNe feedback affects, but does not alleviate, the "core vs. cusp" and "too big to fail" problems.

3.4.1 Neutrino emission and cooling

In the standard picture of core collapse SNe, the three flavors of neutrinos and antineutrinos are produced in the supernova (SN) at temperatures around 30 MeV, mainly via nucleon bremsstrahlung and electron neutrino-antineutrino annihilation. Outside of the first neutronization burst of electron neutrinos, the neutrinos remain trapped in the dense core of the collapsing star for ~ 0.2 s at which point they free-stream out of the star over a time period of ~ 10 s, carrying away the binding energy of the remaining proto-neutron star $\sim 3 \times 10^{53}$ erg. For recent reviews see e.g., [261, 262].

Dark matter candidates with $m_\chi \lesssim 100$ MeV are light enough to be thermally produced in SNe. If these dark matter candidates are weakly interacting, then they can be constrained since the presence of this dark matter could help cool the proto-neutron star, producing a neutrino signal that is in conflict with the observations from SN 1987A. In our scenario, dark matter (with a mass $\gtrsim 10$ MeV) will also be produced in the SN. However, due to the strong dark matter-neutrino interactions, this dark matter will thermalize with the neutrino gas and maintain a thermal distribution out to large radii until the temperature of the neutrinos falls below the dark matter mass, suppressing dark matter production.

Neutrinos begin to free-stream away from the SN when the density of the stellar material drops, which occurs where the matter temperature is ~ 5 MeV $< m_\chi$. At this point, dark matter production is suppressed, but the coupled dark matter-neutrino gas from the core will still diffuse out of the star, cooling the star on timescales set by the speed of sound in the dark

matter-neutrino fluid. In this sense, strong dark matter-neutrino interactions are similar to strong neutrino self-interactions in SNe since they both involve the emission of a strongly-coupled gas, and hence strong dark matter-neutrino interactions will not significantly affect the cooling time for SNe [213, 263]. Thus it is likely that this neutrino-interacting dark matter will not come into conflict with the observation of neutrino cooling from SN 1987A.

In ref. [264] a similar scenario of relatively strong dark matter-nucleon and dark matter-neutrino interactions inside SNe was considered. In this case, the dark matter thermalized with the stellar material and bound the neutrinos to the star out to larger radii and lower temperatures (a result similar to what would be expected from simply increasing the strength of neutrino interactions with regular matter). This would lead to an overall decrease in the energies of the emitted neutrinos and an increase in the cooling time, resulting in a rough bound of $m_\chi \gtrsim 10$ MeV in order to be consistent with the neutrino observations from SN 1987A. However, for the case of dark matter that only interacts with neutrinos, it is natural to expect that the constraint on m_χ will be weakened since the dark matter does not have strong interactions with the stellar material and is not trapped in the core of the star. A precise study of the emission of neutrinos is beyond the scope of this work and will be explored in a future paper [265].

Finally, refs. [213, 266] find that the constraints on neutrino-interacting dark matter from SNe come not from cooling, but from SN neutrinos scattering off the dark matter and out of the line of sight of our detectors. They place a bound on the dark matter-neutrino cross section of $\sigma_{\hat{\nu}_i\chi} \lesssim 10^{-25}$ cm^2 (m_χ/MeV) by requiring that the neutrino mean free path be larger than the Earth-SN distance for a nearby SN. In the next section, we will find that our neutrino-dark matter cross section abides by this constraint except near resonance, producing a feature in the neutrino spectra which should be observable in the next galactic SN.

3.4.2 Observation of a nearby supernova

An interesting consequence of strong dark matter-neutrino interactions is the scattering of SN neutrinos off dark matter on their way to Earth. The parameters implied by the missing

satellite problem make this particularly intriguing because the resonant neutrino energy for scattering, $E_{\rm res} = (m_\phi^2 - m_\chi^2)/2m_\chi$, is in the range of energies produced in SNe since both χ and ϕ have masses that are tens of MeV.

Consider a light neutrino mass eigenstate i that was emitted from a SN. As it travels from the SN to Earth, scattering on dark matter can deflect it, decreasing the flux that is observed,

$$\text{Flux}\,(\hat{\nu}_i)_{\rm Earth} = \text{Flux}\,(\hat{\nu}_i)_{\rm SN}\, e^{-\Gamma_i d}, \tag{3.50}$$

where

$$\Gamma_i = \sigma_{\hat{\nu}_i\chi} \times \frac{1}{d}\int_0^d dx\, n_\chi(x). \tag{3.51}$$

As defined in (3.9), $\sigma_{\hat{\nu}_i\chi}$ is the cross section for $\hat{\nu}_i$ to scatter on dark matter at rest, d is the distance between the SN and Earth, and $n_\chi(x)$ is the dark matter number density along the line of sight. Using (3.9), we can isolate the mass eigenstate dependence,

$$\Gamma_i = \frac{|U_{Ni}|^2}{|U_{e4}|^2 + |U_{\mu 4}|^2 + |U_{\tau 4}|^2}\Gamma, \tag{3.52}$$

with

$$\Gamma = \sigma_{\nu\chi} \times \frac{1}{d}\int_0^d dx\, n_\chi\,(x)\,. \tag{3.53}$$

To get a rough idea of what distance scale this attenuation occurs on, we set $n_\chi(x)$ to a constant value, with a magnitude equal to the local dark matter density, which is typical on galactic scales. That is, we take $n_\chi(x) = \bar{n}_\chi = (0.3\ \text{GeV}/m_\chi)\ \text{cm}^{-3}$. Then $1/\Gamma = 1/\sigma_{\nu\chi}\bar{n}_\chi$ defines a length scale over which neutrino scattering off dark matter is important. This length scale can be comparable to galaxy sizes for neutrinos with energy close to the resonance

energy, $E_{\rm res}$. At this energy the cross section is, for $m_\phi \gg m_\chi$,

$$\sigma_{\nu\chi} \simeq \frac{4\pi}{m_\phi^2} = 3 \times 10^{-24}\ {\rm cm}^2 \left(\frac{40\ {\rm MeV}}{m_\phi}\right)^2, \tag{3.54}$$

where we have also assumed that $m_\phi < m_4$ so that $\Gamma_\phi = g^2 m_\phi/16\pi$. This cross section leads to an attenuation length

$$\frac{1}{\Gamma} \simeq 7\ {\rm kpc} \left(\frac{m_\phi}{40\ {\rm MeV}}\right)^2 \left(\frac{m_\chi}{20\ {\rm MeV}}\right). \tag{3.55}$$

The cross section is this large only in a region of width $\mathcal{O}({\rm MeV})$ around $E_{\rm res}$. Off resonance, the cross section drops quite rapidly below this. (It is necessary for some of the SN neutrinos to have $\sigma_{\nu\chi} \lesssim 10^{-25}\ {\rm cm}^2$, otherwise we would not have seen any neutrinos from SN1987A [213, 266].) Therefore, our dark matter-neutrino interactions manifest as a dip in the spectrum of neutrinos from a SN at a neutrino energy given by $E_{\rm res} = (m_\phi^2 - m_\chi^2)/2m_\chi$.

The mixing matrix U determines the relative attenuation of each eigenstate. For simplicity, in the tribimaximal approximation which is a good rough description of the neutrino mixing pattern, $\sin\theta_{12} = 1/\sqrt{3}$, $\sin\theta_{23} = 1/\sqrt{2}$, and $\theta_{13} = 0$, so the attenuation scales for the three light eigenstates are

$$\frac{1}{\Gamma_1} \simeq \frac{6}{\Gamma}, \quad \frac{1}{\Gamma_2} \simeq \frac{3}{\Gamma}, \quad \frac{1}{\Gamma_3} \simeq \frac{2}{\Gamma}. \tag{3.56}$$

Because of this hierarchy, the fraction of $\hat{\nu}_1$ neutrinos is increased due to scattering on dark matter. As for the flavor composition of the neutrinos, because $\hat{\nu}_1$ has a larger component of ν_e than $\hat{\nu}_2$ or $\hat{\nu}_3$, the fraction of electron neutrinos detected from a SN is likewise increased. Thus, an increase in the electron neutrino fraction at $E_{\rm res}$ is also a telltale sign of strong dark matter-neutrino interactions.

Beyond affecting the signals from nearby SNe, neutrino-dark matter interactions can leave an imprint in the diffuse SN background (DSNB). This was studied in detail in [267] in the context of an effective interaction between (scalar) dark matter and neutrinos. For

parameters relevant for our scenario, the spectral distortion at $E_{\rm res}$ could be observable at proposed next generation experiments like Hyper-Kamiokande.[5]

3.4.3 The "core vs. cusp" and "too big to fail problems"

SNe can also figure prominently in potential solutions to the "core vs. cusp" problem. This problem arises from the discrepancy in the dark matter density profile near the centers of galaxies between standard cold dark matter simulations, which predict cusps, and observations, which favor cores. Some simulations [48–52] and analytic models [53, 54] that include feedback from SNe on the dark matter indicate that this can modify the shape of dark matter profiles near the centers of galaxies, hence solving the core vs. cusp problem. The energy transferred from SNe to the interstellar medium modifies the gravitational potential felt by the dark matter, allowing the dark matter to move away from the center of the galaxy, creating a more cored profile. In some simulations, taking reasonable values for the SN rate, gravitationally transferring on the order of $10^{50} - 10^{51}$ ergs per SN to the dark matter is sufficient to turn a cusped halo into a cored one [48, 52].

Additionally, SN feedback can address the "too big to fail problem" in which simulations predict that the Milky Way satellite galaxies should be more massive than they are observed to be. SN feedback has been shown to reduce the dark matter density in the center of galaxies, alleviating the too big to fail problem [62]. In [52], N-body simulations including SN feedback showed that indeed the too big to fail problem could be solved by the gravitational effect of SN feedback moving dark matter from the center region of galaxies out to larger radii.

It has also been suggested that SN feedback may not be sufficient to address these small scale structure problems [55, 63]. Maximally, around 1% of the supernova energy can be transferred to dark matter gravitationally, causing the dark matter to move away from the center of galaxies via the method described above. The other 99% of the SN energy is

[5] In a similar vein (although unconnected to SNe), neutrinos with energies of $10^2 - 10^3$ TeV have been explored as probes of new neutrino interactions [268]. Because of the suppression of the scattering cross section at high energies, $\sigma_{\nu\chi} \propto 1/E_\nu$, and the small dark matter density relevant for neutrinos traveling cosmological distances, $\rho_\chi \sim 1.5$ keV/cm^3, this is unimportant in our scenario.

released in the form of neutrinos. In the case of strong dark matter-neutrino interactions, the neutrinos released by a SN can transfer energy to dark matter by elastic scattering. This increases the transfer of energy from SNe to dark matter and potentially makes SN feedback more effective at solving the core vs. cusp and too big to fail problems.

Simple estimates show that the energy transfer from SNe to dark matter through this mechanism is of the right order of magnitude to solve the core vs. cusp problem. However, since the scattering length of the neutrinos is a few kpcs or larger, as seen in sec. 3.4.2, each neutrino emitted by a SN in the inner region of a galaxy scatters at most an $\mathcal{O}(1)$ number of times as it leaves the galaxy. In, for example, a bright dwarf galaxy like Fornax, it is estimated that about 10^5 SNe have occurred [55], each of which emitted about 10^{58} neutrinos so that maximally around 10^{63} dark matter particles will gain energy from SNe neutrinos through scattering. This should be compared to the roughly 10^{68} dark matter particles in Fornax, given a galactic mass of $10^9 M_\odot$ and a 20 MeV dark matter mass. Therefore, the energy from SN neutrinos is only distributed to a small fraction of the dark matter and cannot help SN feedback turn a core into a cusp. Accounting for neutrinos from stars that do not become SNe could have an effect on the core vs. cusp problem and will be studied in future work [265].

3.5 Future tests

As we have described, to achieve a cutoff on dark matter structures of $M_{\rm cutoff} \sim 10^8 M_\odot$ requires $|U_{\tau 4}| \gtrsim 0.1$. One promising test of strong dark matter-neutrino interactions is to improve the searches that are sensitive to $|U_{\tau 4}|$. We discuss prospects for this improvement below.

3.5.1 τ decays

For $m_4 > 100$ MeV the strongest constraint on $|U_{\tau 4}|$ comes from τ decays, in particular our estimate using changes to $\Gamma_{\tau \to \mu \nu \bar{\nu}}$. However, the measurements of the branching ratio for $\tau \to \mu$ were not searches for heavy neutrinos and could be subject to systematic biases in ac-

ceptance estimates that assume a vanishing neutrino mass. The best dedicated experimental search for a heavy component to ν_τ used LEP data, based on about 10^5 $\tau^+\tau^-$ pairs, looking at hadronic three- and five-prong decays [227]. We strongly suggest that new experimental searches be undertaken to search for a massive (greater than 10 MeV) neutrino component of ν_τ. The B-factories have each collected about 10^4 times more τ pairs and Belle II will improve on that by an order of magnitude. Therefore the statistical errors in such a search could conceivably improve by ~ 100. Using several decay channels is a good strategy since multi-prong hadronic final states are more sensitive to the reduced phase space available but leptonic decays are subject to less theoretical uncertainty. Although the search in ref. [227] was systematics limited, if the systematic errors for new dedicated searches can be controlled to the level of the statistical ones, an improvement of the sensitivity to $|U_{\tau 4}|$ by a factor of 10 would be possible, exploring a large amount of parameter space favored by solutions to the missing satellite problem. Improving these searches would be a highly desirable test of dark matter-neutrino interactions.

We also briefly mention here that the value of $|V_{us}|$ extracted using τ decays to strange mesons is smaller than that obtained by other methods [269]. In particular, the central value obtained using the ratio $\Gamma_{\tau\to K\nu}/\Gamma_{\tau\to\pi\nu}$ is about 1% below the value from $|V_{ud}|$ and CKM unitarity (assuming $U_{\mu 4} = 0$). The value using the inclusive strange rate is even smaller, about 4% smaller than the CKM unitarity value. While not statistically significant, these points are intriguing and could be signs of a heavy neutrino component to ν_τ since final states involving kaons have less phase space available (which is suggested by the inclusive, multibody final states leading to a smaller $|V_{us}|$). The value of $|U_{\tau 4}|$ required to align the central values of $|V_{us}|$ from $\Gamma_{\tau\to K\nu}/\Gamma_{\tau\to\pi\nu}$ and CKM unitarity is in tension with the estimate of the limit from $\tau \to \mu$ decay derived in sec. 3.2.2 but, as mentioned above, there could be an unaccounted for systematic bias in this estimate. If the discrepancy in $|V_{us}|$ measurements becomes significant, it could be another hint of the existence of an $\mathcal{O}(100$ MeV) component to the τ neutrino.

3.5.2 Matter effects on neutrino oscillations

For m_4 below 100 MeV, the strongest limit on $|U_{\tau 4}|$ is due to matter effects in atmospheric neutrino oscillations. The lack of weak interactions of the sterile neutrino leads to a difference in the matter effects between ν_μ and the linear combination of ν_τ and sterile that makes up the light neutrinos. Limits on $|U_{\tau 4}|$ have been derived from analyzing the zenith angle distribution of muon neutrinos at Super-K [245] and in IceCube and (low energy) DeepCore data in the language of neutrino non-standard interactions (NSIs) [246]. The Super-K limit on $|U_{\tau 4}|$ is statistics limited and will be improved with more data. An analysis of the PINGU upgrade of IceCube indicates that it will be able to place a 90% C. L. upper limit on the NSI parameter $\epsilon_{\tau\tau}$ of 1.7×10^{-2} [270]. This will improve the reach on $|U_{\tau 4}|$ to about 0.3. Furthermore, a year of full DeepCore data will allow $\epsilon_{\tau\tau}$ to be probed at 90% C. L. to 6×10^{-3} [246] which will allow values of $|U_{\tau 4}| > 0.2$ to be tested. This is a very promising test of the model.

3.5.3 U_{e4} and $U_{\mu 4}$

In addition to a nonzero $U_{\tau 4}$ we might expect, at some level, that U_{e4} and $U_{\mu 4}$ are also not vanishing in this model. While it is technically natural for U_{e4} and $U_{\mu 4}$ to be extremely suppressed compared to $U_{\tau 4}$ (radiative contributions to $U_{e4}, U_{\mu 4}$ are necessarily generated but are proportional to the light neutrino masses and are therefore tiny), it is not a requirement that the sterile-active neutrino coupling only violate L_τ. (We use L_ℓ to label the global U(1) associated with lepton flavor ℓ.) In most of this paper, for simplicity and in light of the phenomenological requirement that $U_{\tau 4} \gg U_{e4}, U_{\mu 4}$, we have ignored U_{e4} and $U_{\mu 4}$ but it is possible that they are nonzero. In fact, it is easy to contemplate a model in which the hierarchy $U_{\tau 4} \gg U_{e4}, U_{\mu 4}$ is enforced with $U_{e4}, U_{\mu 4} \neq 0$ by imposing a symmetry that satisfies minimal flavor violation (MFV). In an MFV scenario, we would expect that λ_i in (3.1) are proportional to the lepton Yukawas so that, in addition, $U_{\mu 4} \gg U_{e4}$.

If we take the reasonable view that in this model U_{e4} and $U_{\mu 4}$ are not strictly zero, we

could potentially expect to see a signal in the observables that we used to constrain U_{e4} and $U_{\mu 4}$ in sec. 3.2.2. Furthermore, we might also expect signals in lepton-flavor–violating (LFV) processes such as $\tau \to \mu\gamma$, $\tau \to e\gamma$, $\mu \to e\gamma$, or $\mu \to e$ conversion. The fact that this model includes a neutrino with a mass above 10 MeV adds additional motivation to search for LFV—a relatively large m_4 reduces the GIM-suppression of such processes. The decay $\tau \to \mu\gamma$ could be particularly interesting in an MFV context, while the effort to greatly improve the reach in sensitivity to $\mu \to e\gamma$ and $\mu \to e$ conversion makes these processes interesting as well.

Lastly, a nonzero value of $U_{\mu 4}$ would also open up the possibility of observing this model in $\nu_\mu \to \nu_\tau$ oscillations at the proposed short baseline experiment MINSIS [271]. MINSIS proposes to use the NUMI beamline at Fermilab with a kton-scale emulsion cloud chamber detector, capable of observing τ neutrinos, situated 1 km away. Early studies indicate that, for $|U_{\tau 4}|^2 = 0.1$, sensitivity to $|U_{\mu 4}|^2$ above roughly 10^{-6} is possible [271].

3.6 Summary and Prospects

The paradigm of cold dark matter does an excellent job of describing a wide range of data on the scales of galaxy clusters or larger. However, there appear to be persistent discrepancies between predictions in the cold dark matter paradigm and observations at smaller scales.

In this chapter, have focused on one of these problems, that of missing satellites. This problem can be solved by introducing strong interactions between neutrinos and dark matter which keep the dark matter in thermal equilibrium with the relativistic matter in the early Universe to lower temperatures than typically expected. This washes out structures with masses below a particular scale $M_{\rm cutoff}$. If $M_{\rm cutoff}$ is chosen to be in the range $10^7 - 10^9 M_\odot$, then the expectation for the number of satellite galaxies of a Milky Way sized galaxy can be brought into agreement with observations, solving the missing satellites problem. A cutoff of this size requires a large dark matter-neutrino scattering cross section. This can be realized in a renormalizable theory if the dark matter has a mass that is tens of MeV and is coupled to a sterile neutrino that mixes with the active neutrinos. The strength of the mixing that is

required combined with both cosmological and particle physics data implies that the sterile neutrino mixes most with ν_τ and leads to a heavy neutrino that is mostly sterile but also has a sizable ν_τ component.

There are a number of signatures of this scenario, both for astrophysical and particle physics experiments. Strong dark matter-neutrino interactions are particularly interesting for supernovae. The mass scale implied by a solution to the missing satellites problem indicates that a future observation of neutrinos from a nearby supernova could show an imprint of dark matter-neutrino scattering. This scenario can also be tested at neutrino oscillation experiments, due to the the change in matter effects from the presence of a sterile neutrino. τ decays are also a promising area to search for the signs of neutrino-dark matter interactions. Improvements of the searches for a massive component of ν_τ would be a useful way of probing this model. Lastly, lepton-flavor–violating processes are well motivated by this scenario. The reach of searches for these processes will be greatly improved in the near future, opening up the opportunity for the discovery of dark matter-neutrino interactions.

Chapter 4

DARK MATTER IN NEUTRON STARS

This chapter is based on my work with Ann Nelson and Sanjay Reddy in ref. [272].

4.1 Introduction

Dark matter-nucleon interactions are most straightforwardly examined using direct detection experiments. However, dark matter-nucleon interactions can also be probed by considering astrophysical observations. For example, in early work in refs. [273, 274], it was argued that dark matter (or any hypothetical weakly interacting particle) that interacted with nucleons could be accreted by stars. The accreted dark matter could then alter thermal transport in stars, reducing neutrino emission and solving the solar neutrino problem. The first time neutron star accretion of dark matter was used to constrain dark matter-nucleon interactions was in ref. [275], and in the past few years there has been a renewed interest in using neutron stars to place constraints on dark matter, see for exmaple, refs. [276–288] (and after the publication of our paper, [289–295]). One constraint comes from neutron star accretion of a particular kind of dark matter which can collapse to form a dark matter black hole that then destroys the star. Observationally, the oldest neutrons stars are around 10 billion years old [296], hence the dark matter parameter space which allows for neutron star destruction in less than 10 billion years can be ruled out.

In this chapter, we only consider bosonic dark matter since, due to the absence of Fermi pressure, it becomes gravitationally unstable for fewer accumulated particles than fermionic dark matter, resulting in stronger constraints. We also focus on asymmetric dark matter (for recent reviews see [297, 298]), in which there is an initial asymmetry between particles and antiparticles so that today only particles remain and dark matter annihilation (and

hence heating) in the neutron star can be ignored. Co-annihilation of dark matter with other particles in the neutron star was considered in [288] and will be neglected in our analysis. By calculating the time for dark matter accretion, thermalization, and black hole formation in neutron stars for the case of asymmetric, bosonic dark matter, otherwise model-independent constraints can be placed on dark matter-nucleon interactions. Here we show that an improved treatment of particle kinematics and many-body effects, including Pauli-blocking, superfluidity, and superconductivity, can have a significant effect on the dark matter thermalization time, potentially changing the final dark matter constraint. We also show that in some phases of high density matter, such as color superconducting quark matter, thermalization times can be surprisingly large.

We now review the dark matter accumulation process as previously discussed by many others (e.g. refs. [281, 284]). There are number of steps involved. First, because of its gravitational interactions, dark matter is accreted by the neutron star. We can estimate the velocity v of the incident dark matter particle at the surface of the neutron star by using classical energy conservation:

$$\gamma(v) = \gamma(v_\infty) + \frac{2GM}{R} \ , \tag{4.1}$$

where $\gamma(v) = (1 - v^2)^{-1}$ and v_∞ is the dark matter particle's velocity infinitely far from the neutron star. We will take $v_\infty = 10^{-3}$ and for a typical neutron star, $M = 1.4 M_\odot = 2.8 \times 10^{30}$ kg and $R = 10$ km. Using these standard values, we find $v \simeq 0.7$. Hence the energy that a typical dark matter particle has at the surface of a neutron star is $E \simeq 1.4 m_\chi$. Note that the incident dark matter energy is set by its mass and that typical dark matter particles are at most semi-relativistic. Due to their hypothesized interactions with nucleons, these incident dark matter particles will scatter with particles inside the neutron star, lose energy, and become bound to the star.

As the dark matter scatters inside the neutron star, it will thermalize with the star. Since the incident dark matter particle is at most semi-relativistic, and it must lose energy in order

to be captured by the neutron star, it is safe to assume that the typical dark matter particle is non-relativistic during the latter collisions that determine its thermalization time. As the dark matter thermalizes, it collects within a sphere of radius $r_{\rm th}$ which satisfies

$$\frac{GM(r_{\rm th})m_\chi}{r_{\rm th}} \approx \frac{3}{2}T \ , \tag{4.2}$$

where $M(r_{\rm th})$ is the mass of the neutron star enclosed within a radius $r_{\rm th}$ and T is the temperature of the neutron star. We can estimate this by considering a neutron star with a constant core density $\rho_{\rm c} = 0.5$ GeV/fm^3 and we find [280]

$$r_{\rm th} \approx 2.2 \text{ m } \left(\frac{T}{10^5 \text{ K}}\right)^{1/2} \left(\frac{\text{GeV}}{m_\chi}\right)^{1/2} \ . \tag{4.3}$$

This tiny sphere of dark matter at the center of the neutron star can begin to self-gravitate and collapse into a black hole. Gravitational collapse is accelerated if the captured dark matter forms a Bose-Einstein condensate inside the star [282, 299]. Once the black hole is formed, it must be massive enough to avoid evaporation due to Hawking radiation and then it may consume the neutron star.[1]

In previous work [281, 284], two calculations to constrain the dark matter-neutron cross section as a function of dark matter mass are done: 1) a thermalization time calculation: $\tau_{\rm th} = 10^{10}$ years, in which $\tau_{\rm th}$ is the time necessary for dark matter thermalization with the neutron star and 2) an accretion time calculation: $\tau_{\rm acc} = 10^{10}$ years, in which $\tau_{\rm acc}$ is the time needed for the neutron star to accrete enough dark matter to form a black hole which will destroy the star (assuming thermalization occurs in a negligible amount of time). The second calculation typically sets the final constraint, and the first is used to find regions where the second constraint is not valid. In this chapter we will consider only the first thermalization calculation and will argue that a proper consideration of many-body effects

[1] The observational signatures of a neutron star collapsing into a black hole is still an interesting, open question.

inside the neutron star can alter previous calculations of the thermalization time, potentially changing the final dark matter constraint.

This rest of this chapter is organized as follows. In sec. 4.2, we discuss the effective theory for our dark matter model. We examine the case of mixed sneutrino dark matter as an example of an asymmetric, bosonic dark matter candidate that can be constrained by black hole formation in neutron stars in sec. 4.3. In sec. 4.4, we define the thermalization time, compare our results to those previously obtained, and introduce new, relevant types of matter that the dark matter can interact with inside the neutron star. We conclude in section 4.5.

4.2 Dark Matter Model

We consider a model in which dark matter is a complex scalar which couples to regular matter by exchanging a heavy spin one boson. The effective Lagrangian for the interaction between dark matter and the fermions (nucleons, electrons, etc.) that are found in neutron stars is then given by

$$\mathcal{L}_{\rm int} = \tilde{G}\ell_\mu \left(j_V^\mu + \alpha j_A^\mu\right) \ , \tag{4.4}$$

where $\ell_\mu = \partial_\mu\chi^\dagger\chi - \chi^\dagger\partial_\mu\chi$ is the dark matter current, $j_V^\mu = \bar{\psi}\gamma^\mu\psi$ and $j_A^\mu = \bar{\psi}\gamma^\mu\gamma_5\psi$ are the vector and axial-vector currents for the fermions, and α is the coupling of j_A^μ to the mediator divided by the coupling of j_V^μ to the mediator.[2] For simplicity, we take α to be the standard model value for fermions coupling to the Z^0 boson. $\tilde{G}$ is the coupling constant after the heavy mediator has been integrated out. In general,

$$\tilde{G} = \frac{g_\chi g_\psi^V}{M_H^2} \ , \tag{4.5}$$

[2]Unless forbidden by some symmetry, this effective theory also includes dark matter self-interactions. These have been shown to affect the critical number of dark matter particles needed for black hole formation [287,288], but are not relevant for thermalization time calculations and hence will not be discussed further here.

where M_H is the mass of the heavy mediator particle, g_χ is the coupling of the mediator to ℓ^μ, and g_ψ^V is the coupling of the mediator to j_V^μ.

In order for this effective theory to capture the relevant physics, the magnitude of the four-momentum transfer squared q^2 in the dark matter-fermion scattering processes must be much less than M_H^2 . Based on the arguments in the previous section we know that the initial dark matter energy is at most $1.4m_\chi$ and hence the maximum q^2 that the dark matter can give up is $|q_\chi^2|^{\max} \approx 4m_\chi^2$. Since the fermions inside the neutron star are highly degenerate, scattering events in which the dark matter gains energy and momentum from them are rare and have typical $\sqrt{q^2} \sim T \sim 9$ eV $<< m_\chi$ for the dark matter masses we are considering. (We will always take $m_\chi \gtrsim 1$ keV as it was shown in ref. [282] that for $m_\chi \lesssim 1$ keV, the captured and thermalized dark matter can escape the neutron star.) Hence as long as $m_\chi << M_H$, then $q^2 << M_H^2$ and our effective theory is valid. For this reason we will take $m_\chi < 5$ GeV, consistent with the assumption that the heavy vector mediator is either a standard model Z^0 or $W^\pm$ pair, or a heavy, undiscovered particle.

4.3 Light Mixed Sneutrino Dark Matter

Light dark matter candidates (with $m_\chi < 5$ GeV) such as mixed sneutrinos would typically be classified as warm dark matter, but they can also be produced non-thermally via the Affleck-Dine mechanism, making these light particles valid dark matter candidates. The Affleck-Dine mechanism was originally associated with baryogensis [93] but it can be applied to any scalar field that can have a large vev and whose interactions are negligible. In a cosmological context, the end result of this mechanism is to non-thermally produce a large number of nearly zero-momentum particles—exactly what is needed for cold dark matter.

To see this explicitly, consider the Lagrangian density for a complex scalar field χ with mass m_χ in curved space time with metric g,

$$\mathcal{L} = \sqrt{-\det\, g}\left(|\partial_\mu \chi|^2 - m_\chi^2|\chi|^2 - V_{\rm int}(\chi)\right) \ . \tag{4.6}$$

In the following we neglect the interaction terms, i.e. we take $V_{\text{int}} \to 0$, and we assume that inflation smooths out any spatial dependence in our field so that $\chi \approx \chi(t)$. Working under the assumption that the Universe is flat, isotropic, and homogeneous, we use the FRW metric with scale factor $a(t)$ (c.f. (1.1)). Thus the classical equation of motion for our field is

$$\ddot{\chi} + 3H(t)\dot{\chi} + m_\chi^2 \chi = 0 \ , \tag{4.7}$$

where dots indicate time derivatives and $H(t) = \dot{a}/a$ is the Hubble parameter.

This is a damped harmonic oscillator equation, so that for $H(t) >> m_\chi$ (which occurs early in the Universe) χ is overdamped and hence is frozen at its initial vev, $\chi(t) = \chi_0$. For late times with $m_\chi >> H(t)$, χ oscillates (only in time) with its natural frequency m_χ and we find that the energy density of the field ρ_χ is proportional to χ_0 and scales like a^{-3} just like the energy density for highly non-relativistic matter [93]:

$$\rho \propto m_\chi^2 \chi_0^2 \left(\frac{1}{a}\right)^3 \ . \tag{4.8}$$

For very non-relativistic dark matter, $\rho_\chi = m_\chi n_\chi$, where n_χ is the number density of dark matter particles, thus we also have that $n_\chi \propto m_\chi \chi_0^2 / a^3$ so that for the proper choice of the initial vev χ_0, we can match the number density of χ particles today to what we observe for dark matter, i.e.

$$n(t_0) = \frac{1}{m_\chi} \left(\frac{3H_0^2 M_{\text{Pl}}^2}{8\pi}\right) \Omega_c \ , \tag{4.9}$$

where t_0 is the time today, M_{Pl} is the gravitational constant, H_0 is the Hubble parameter today, and $\Omega_c \approx 0.26$ [35]. We also note that the dark matter masses considered in this chapter are large enough so that in order to match the energy density today, the vev χ_0 is small enough such that dark matter is present (beginning roughly at the time that satisfies $H(t) = m_\chi$) before matter domination, as required by observations of the CMB.

It is easy to explain why interaction terms for χ are negligible, as well as why a macroscopically large vev can form during the early Universe if χ can be non-zero along a flat

direction in the scalar potential. Such flat directions are common in supersymmetric theories; for example, it is possible to find flat directions with combinations of squarks, sleptons, and Higgs fields in the Minimal Supersymmetric Standard Model [300].

Now that we have argued that Affleck-Dine produced, mixed sneutrinos can make up the dark matter, we will address the mixed sneutrino coupling to ordinary matter. Specifically we take the mixed sneutrino dark matter candidate to be the lightest mass eigenstate of some linear combination of active sneutrinos $\tilde{\nu}$ and an additional sterile sneutrino $\tilde{N}$. Such mixed sneutrino dark matter is discussed, for example, in refs. [301–304]. This dark matter particle carries lepton number of $+1$ and based on the initial vev for the dark matter field, there can be an initial asymmetry between the number of dark matter particles and antiparticles, making dark matter annihilation negligible today. Since the dark matter field, χ, is a superposition of $\tilde{\nu}$ and $\tilde{N}$ we can write

$$\tilde{\nu} = \psi \cos\theta + \chi \sin\theta \ , \tag{4.10}$$

$$\tilde{N} = -\psi \sin\theta + \chi \cos\theta \ , \tag{4.11}$$

where ψ is the heavier mass eigenstate. Note that for $\sin\theta \lesssim 0.27$, m_χ is unconstrained by the invisible Z^0 width [305].

$\tilde{N}$ is a weak isosinglet with only gravitational interactions and $\tilde{\nu}$ is in a weak doublet. We take the dominant interactions of χ to be with the weak gauge bosons (its coupling to ψ is kinematically suppressed and we take its couplings from the superpotential to be negligible). We can find χ's weak interactions with gauge bosons from its gauge invariant kinetic terms

$$\mathcal{L}_{\rm kin} = -D^\mu \tilde{\nu}^\dagger D_\mu \tilde{\nu} - D^\mu \tilde{N}^\dagger D_\mu \tilde{N} \ , \tag{4.12}$$

where $D_\mu \tilde{\nu} = \partial_\mu \tilde{\nu} - i(g_1 B_\mu Y + g_2 A^a_\mu T^a)\tilde{\nu}$ and $D_\mu \tilde{N} = \partial_\mu \tilde{N}$. $Y = I/2$ is the hypercharge generator and the $T^a = \sigma^a/2$ are the $SU(2)_L$ generators. The relation of the A^a_μ and B_μ

gauge bosons to the standard model photon A_μ, the Z^0, and the $W^\pm$ bosons is

$$\begin{aligned} A^1_\mu &= \tfrac{1}{\sqrt{2}}(W^-_\mu + W^+_\mu) \ , \\ A^2_\mu &= \tfrac{1}{\sqrt{2}i}(W^-_\mu - W^+_\mu) \ , \\ A^3_\mu &= Z^0_\mu \cos\theta_w + A_\mu \sin\theta_w \ , \\ B_\mu &= A_\mu \cos\theta_w - Z^0_\mu \sin\theta_w \ , \end{aligned} \tag{4.13}$$

where $\tan\theta_w = \frac{g_1}{g_2}$ and $e = g_2 \sin\theta_w$. e is the magnitude of the electron charge and θ_w is the weak mixing angle. Replacing $\tilde{N}$ and $\tilde{\nu}$ with χ and ψ, we find that the interaction Lagrangian for χ is given by

$$\begin{aligned} \mathcal{L}_{int} =& \frac{i\sin^2\theta}{2}\sqrt{g_1^2+g_2^2}Z^0_\mu\left[\partial^\mu\chi^\dagger\chi - \chi^\dagger\partial^\mu\chi\right] \\ &- \frac{\sin^2\theta}{2}g_2^2\chi^\dagger W^+_\mu W^{-\mu}\chi - \frac{\sin^2\theta}{4}(g_1^2+g_2^2)\chi^\dagger Z^0_\mu Z^{0\mu}\chi \ . \end{aligned} \tag{4.14}$$

If the the four-momentum transfer squared in a dark matter-$Z^0/W^\pm$ interaction is less than a few GeV, then the first term in the above interaction Lagrangian is dominant. We may integrate out the Z^0 in the remaining term, giving us the generic effective Lagrangian form that we had in (4.4). In this case, the effective coupling constant is given by

$$\tilde{G} = \frac{e^2 c_V \sin^2\theta}{2M_Z^2 \sin^2\theta_w \cos^2\theta_w} \ , \tag{4.15}$$

where $c_V = \frac{1}{4}$ for a neutron and $c_V = -\frac{1}{4} + \sin^2\theta_w$ for an electron.

4.4 Thermalization Time Calculation and Results

4.4.1 The Thermalization Time

We now return to our generic dark matter model of sec. 4.2 and proceed with a calculation of the thermalization time. For scattering between dark matter and fermions, let $k^\mu = (E^\chi_k, \vec{k})$ be the initial dark matter four-momentum, $k'^\mu = (E^\chi_{k'}, \vec{k'})$ be the final dark matter four-

momentum, $p^\mu = (E_p^f, \vec{p})$ be the initial fermion four-momentum, and $p'^\mu = (E_{p'}^f, \vec{p'})$ be the final fermion four-momentum. We define the thermalization time as the average time it takes for an incident dark matter particle to start participating in collisions in which the average energy transfer is less than the temperature of the neutron star, i.e. $\langle q_0 \rangle \lesssim T$ where q_0 is the zeroth component of the four-momentum transfer $q_\mu = k_\mu - k'_\mu$. We will assume that the dark matter particles are confined to the neutron star interior.[3] Since we are considering the oldest, coldest neutron stars, we take $T = 10^5$ K ≈ 9 eV.

To derive a formula for the thermalization time, we will make use of the dark matter scattering rate Γ. Using Fermi's Golden Rule, the scattering rate for dark matter scattering with a medium of spin 1/2 fermions is given by

$$\Gamma = 2 \int \frac{d^3p}{(2\pi)^3} \int \frac{d^3k'}{(2\pi)^3 2E_{k'}^\chi} \int \frac{d^3p'}{(2\pi)^3 2E_{p'}^f} (2\pi)^4 \delta^4(p^\mu + k^\mu - p'^\mu - k'^\mu) \times \frac{\langle |\mathcal{M}|^2 \rangle}{2E_p^f 2E_k^\chi} n_F(E_p^f) \left(1 - n_F(E_{p'}^f)\right) \left(1 + n_B(E_{k'}^\chi)\right) , \tag{4.16}$$

where $\mathcal{M}$ is the amplitude for the scattering process, n_F is the fermion distibution function (Fermi-Dirac for non-interacting fermions), and n_B is the dark matter distribution function (Bose-Einstein for non-interacting bosonic dark matter). For simplicity, we will neglect the Bose enhancement factor for the final dark matter state since the distribution function for the dark matter particles is a complicated function of time due to the accumulation of dark matter. Note that this means that (4.16) as is, is actually a lower bound on the scattering rate.

The tree level squared amplitude is averaged over initial and summed over final fermion

[3] While dark matter particles which have just become bound to the neutron star may have an orbit that goes outside the star [281], unless dark matter is extremely light ($m_\chi \lesssim 1$ keV), the dark matter particles are confined to the neutron star interior for later stages of cooling.

spins and is given by

$$\langle|\mathcal{M}|^2\rangle = 2\tilde{G}^2\left\{(1+\alpha^2)\left[2\left(p'\cdot(k+k')\right)\left(p\cdot(k+k')\right)-(p'\cdot p)(k+k')\cdot(k+k')\right]\right. \\ \left. +\,(1-\alpha^2)\left[m_f^2(k+k')\cdot(k+k')\right]\right\}\ , \tag{4.17}$$

where we have used the notation $a\cdot b\equiv a^\mu b_\mu$ with the mostly minus metric and m_f is the fermion mass which could be the neutron or the electron mass, m_n or m_e respectively.

If we instead use finite temperature formalism, the scattering rate can also be expressed as [306–308]

$$\Gamma = -2\tilde{G}^2\frac{1}{1-e^{-q_0/T}}\int\frac{d^3k'}{(2\pi)^3}\frac{\mathrm{Im}[\mathcal{L}^{\mu\nu}\Pi^R_{\mu\nu}]}{2E^\chi_k 2E^\chi_{k'}}\ , \tag{4.18}$$

where $\mathcal{L}_{\mu\nu}$ contains the dark matter currents and $\Pi^R_{\mu\nu}$ is the fermion retarded polarization tensor. For non-interacting fermions, these are given by

$$\mathcal{L}_{\mu\nu} = (k+k')_\mu(k+k')_\nu\ , \tag{4.19}$$

$$\mathrm{Im}\left[\Pi^R_{\mu\nu}\right] = \mathrm{Im}\Bigg[-i\tanh\left(\frac{q_0}{2T}\right) \\ \times\int\frac{d^4p}{(2\pi)^4}Tr[G(p)(\gamma_\mu+\alpha\gamma_\mu\gamma_5)G(p+q)(\gamma_\nu+\alpha\gamma_\nu\gamma_5)]\Bigg]\ , \tag{4.20}$$

where $G(p)$ is the free fermion propagator at finite temperature and density. The form for this polarization tensor has been worked out in detail in refs. [308] and [309] and we use their results in our calculations.[4]

The polarization tensor $\Pi^R_{\mu\nu}$ characterizes the medium response to the dark matter probe. The fermion propagators contain the Pauli blocking factors (c.f. the factor of $n_F(E^f_p)(1-n_F(E^f_{p'}))$ in (4.16)) which restrict the fermion phase space due to the Pauli exclusion principle, i.e. the incident fermion that interacts with the dark matter particle must come from

[4]If using the derivation in ref. [308], note that some of the equations had typos [310]. In particular, eq. (69) should be $e_- = -\beta\frac{\tilde{q_0}}{2}+\frac{q}{2}\sqrt{\beta^2+4\frac{M_2^{*2}}{q^2-\tilde{q_0}^2}}$, eq. (78) should be $I_1 = T^2 z\left(\frac{\mu_2-U_2}{T}-\frac{z}{2}-\frac{\xi_2}{z}+\frac{e_-\xi_1}{zT}\right)$, and eq. (79) should read $I_2 = T^3 z\left(\frac{(\mu_2-U_2)^2}{T^2}-z\frac{\mu_2-U_2}{T}+\frac{\pi^3}{3}+\frac{z^2}{3}+2\frac{\xi_3}{z}+2\frac{e_-\xi_2}{Tz}+\frac{e_-^2\xi_1}{T^2 z}\right)$.

the initial fermion distribution and the scattered fermion must occupy phase space that is not already filled by the initial fermion distribution. The polarization tensor also contains information about the in-medium fermion-fermion interactions since $\Pi^R_{\mu\nu}$ is a fermion current-current correlation function which includes a sum over all possible intermediate states.

Given an expression for the scattering rate (either (4.16) or (4.18)), we can now define a discretized version of the thermalization time $\tau_{\rm th}$ based on the physical reasoning that the average thermalization time is simply the sum of the average times for subsequent dark matter collisions until the average energy transfer per collision is less than the temperature of the neutron star. Thus we may write

$$\tau_{\rm th} = \frac{1}{\Gamma(E_0)} + \frac{1}{\Gamma(E_1)} + \frac{1}{\Gamma(E_2)} + \ldots + \frac{1}{\Gamma(E_n)} \ , \tag{4.21}$$

where E_0 is the initial dark matter energy, which we will always estimate to be $1.05 m_\chi$ (note that this assumes a $\sim 40\%$ decrease in initial dark matter velocity due to prior collisions necessary for dark matter capture) and E_i for $i > 0$ is the average final energy of a dark matter particle after a collision in which it had initial energy E_{i-1}. The final energy E_i is determined by calculating the scattering rate for a dark matter particle with initial energy E_{i-1} weighted by the final dark matter energy, and dividing by the unweighted scattering rate for a dark matter particle with initial energy E_{i-1}, i.e.

$$\langle E_i(E_{i-1}) \rangle = \frac{\int d\Gamma(E_{i-1}) E^\chi_{k'}}{\int d\Gamma(E_{i-1})} \ . \tag{4.22}$$

The summation in (4.21) ends once $\langle E_n - E_{n+1} \rangle < T$ and we expect that this generally results in $E_n \approx T$. Expression (4.21) is used for all of our numerical work.

We also define an approximate, continuous version of the thermalization time as

$$\tau_{\rm th} = -\int_{E_0}^{E_n} \frac{dE_i}{\int d\Gamma(E_i)(E_i - E_f)} \ . \tag{4.23}$$

We use (4.23) for our analytic results, where instead of finding E_n as described above, E_n is

fit to a value that well-approximates the numerical result.

Now that the thermalization time is well defined, we can calculate the dark matter thermalization time inside a neutron star. This includes dark matter scattering with the usual components of a neutron star: a liquid of neutrons, protons, and electrons, a neutron superfluid, and a proton superconductor. It also includes dark matter scattering with the matter in the core of the neutron star—possibly hyperons, pion or kaon condensates, or a quark gluon plasma, etc. For a review of the constituents of a neutron star see refs. [311–314]. The majority of the neutron star (roughly 85%) is made up of neutrons, so we will first consider dark matter thermalization by scattering with neutrons, in both the normal phase (a Fermi gas) and the superfluid phase.

4.4.2 Scattering with a Fermi Gas of Neutrons

Nucleon-nucleon scattering data indicate that the neutron-neutron interaction can be either attractive or repulsive depending on the spin and spatial angular momentum of the neutrons and on the neutron density [315]. At sufficiently low temperature, attractive interactions can lead to superfluidity and dramatically alter the low-lying excitation spectrum, and hence the dark matter scattering mechanism. We address this in detail in the next section. Here, to calculate dark matter-neutron scattering, we will ignore nuclear interactions and approximate the neutrons as a dense, non-interacting Fermi gas. This will provide a baseline result since Fermi-liquid theory demonstrates that corrections due to strong interactions in the normal Fermi gas phase do not qualitatively change the nature of scattering or the kinematics [316]. Additionally, from earlier work relating to neutrino scattering in dense, normal neutron star matter [317], we expect that the dark matter scattering rates off neutrons in the Fermi gas approximation are sufficient to provide a reliable order of magnitude estimate.

The fiducial calculation is done for neutrons at saturation density ($n_0 \approx 0.16$ fm^{-3}) which corresponds to a non-relativistic neutron chemical potential of $\mu_n \approx 0.056$ GeV. This implies that neutrons at saturation density are to a good approximation, non-relativistic. Deep in the core, neutrons become mildly relativistic, but these relativistic corrections are modest.

We calculate the thermalization time and then enforce $\tau_{\rm th} = 10^{10}$ years, which constrains $\tilde{G}$ as a function of m_χ. We then use this constrained coupling constant in the formula for the dark matter-fermion cross section in the limit in which both the dark matter and fermion momenta tend to zero[5]:

$$\sigma_{\chi f} = \frac{\tilde{G}^2}{\pi} \frac{m_f^2 m_\chi^2}{(m_f + m_\chi)^2} \ . \tag{4.24}$$

This gives the dark matter-fermion cross section as a function of dark matter mass alone, with the constraint that dark matter thermalization takes longer than 10^{10} years.

For non-interacting neutrons it is simplest to use (4.16) for the scattering rate in the calculation of the thermalization time. Expression (4.16) was used for numerical calculations and an approximate analytic result was obtained as follows. For thermalization time scatterings it is a good approximation that both the neutrons and dark matter are non-relativistic, so neglecting all momentum dependence in the amplitude (4.17) and rewriting the scattering rate we find

$$\Gamma \approx \tilde{G}^2 \int \frac{d^3k'}{(2\pi)^3} S(q_0, q) \ , \tag{4.25}$$

where $q_\mu = (q_0, \vec{q}) = k_\mu - k'_\mu$ is the four-momentum transfer and $q = |\vec{q}|$. $S(q_0, q)$ is the neutron response function, here taking the form

$$S(q_0, q) = 2 \int \frac{d^3p}{(2\pi)^3} \int \frac{d^3p'}{(2\pi)^3} (2\pi)^4 \delta^4(p^\mu + k^\mu - p'^\mu - k'^\mu) n_F(E_p^n) \left(1 - n_F(E_{p'}^n)\right) \ , \tag{4.26}$$

where $n_F(E) = [1 + e^{(E-\mu)/T}]^{-1}$ is the Fermi-Dirac distribution function. In the limit of completely degenerate neutron matter ($\mu_n/T \sim 6.5 \times 10^6$ so the neutrons really are quite degenerate) and for $q << m_n$, we have [308]:

$$S(q_0, q) \approx \frac{m_n^2 T}{\pi q} \left(\frac{z}{1 - e^{-z}} \right) \Theta(q v_F - |q_0|) \ , \tag{4.27}$$

[5]We do this to provide a dark matter-nucleon cross section constraint which is comparable to direct detection experiments which constrain the dark matter-nucleon cross section for non-relativistic dark matter and nucleons. The typical dark matter momentum is $\sim 10^{-3}$ in the solar vicinity, so any velocity dependence in $\sigma_{\chi f}$ (as observed by direct detection experiments) is greatly suppressed.

where $z = q_0/T$, Θ is the Heaviside step function, and $v_F = p_F/m_n \approx 0.35$ is the neutron Fermi velocity.

Note that the step function is just enforcing non-relativistic, low momentum transfer neutron kinematics, i.e. that $|q_0| < v_F q$. That this inequality holds can be seen simply from

$$q_0 = E^n_{p'} - E^n_p = \sqrt{m_n^2 - (\vec{p}+\vec{q})^2} - \sqrt{m_n^2 + p^2} = \frac{pq\cos\theta}{E^n_p} + \mathcal{O}\left(\frac{q^2}{E_n}\right) , \tag{4.28}$$

where θ is the angle between $\vec{p}$ and $\vec{q}$. These neutron kinematics must be consistent with the same non-relativistic, low momentum transfer dark matter kinematics ($|q_0| < v_\chi q$) and since $v_\chi \leq 1/3$ almost always, the dark matter kinematics constrain the phase space more, and the neutron step function in (4.27) can simply be set to 1. These kinematics are shown in fig. 4.1.

Using (4.27) in (4.25), setting e^{-z} to zero as the thermalization time definition always has $q_0 > T$, and completing the angular integrals gives

$$d\Gamma \approx \frac{\tilde{G}^2 m_n^2}{4\pi^3} k'^2 q_0 \left(\frac{k + k' - |k'-k|}{kk'}\right) dk' . \tag{4.29}$$

Since the neutrons are approximated as completely degenerate, dark matter cannot lose energy to them, hence $k' \leq k$, and using $q_0 = k^2/(2m_\chi) - k'^2/(2m_\chi)$, we find

$$d\Gamma \approx \frac{\tilde{G}^2 m_n^2}{2\pi^3 k} k'^2 \left(\frac{k^2}{2m_\chi} - \frac{k'^2}{2m_\chi}\right) dk' . \tag{4.30}$$

We can now use this to calculate the denominator in (4.23)

$$\int d\Gamma(E_i)(E_i - E_f) = \int d\Gamma(E^\chi_k)(E^\chi_k - E^\chi_{k'}) \approx \frac{\tilde{G}^2 m_n^2}{2\pi^3 k} \int_0^k k'^2 \left(\frac{k^2}{2m_\chi} - \frac{k'^2}{2m_\chi}\right)^2 dk' . \tag{4.31}$$

Integration gives

$$\int d\Gamma(E_i)(E_i - E_f) \approx \frac{\tilde{G}^2 m_n^2}{105\pi^3 m_\chi^2} k^6 . \tag{4.32}$$

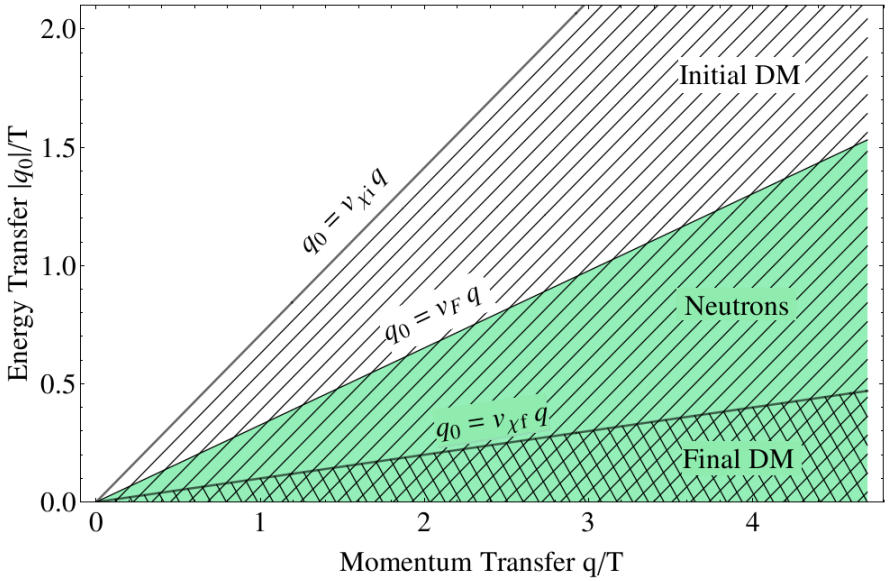

Figure 4.1: Plot of the magnitude of the momentum transfer as a function of energy transfer, both in units of T, for momentum transfers much less than the mass and momentum of the particle involved. The shaded areas show kinematically allowed regions. The positively sloped lined region is for initial dark matter (with $v_{\chi i} = 0.7$), the green, shaded region is for neutrons, and the negatively sloped lined region is for final dark matter (with $v_{\chi f} << v_{\chi i}$ after the dark matter has lost energy to the neutrons). Dark matter-neutron scattering can take place in the kinematic regions where the dark matter-only and neutron-only kinematic regions overlap.

Using this in (4.23) we find

$$\tau_{\rm th} \approx \frac{105\pi^3 m_\chi}{4\tilde{G}^2 m_n^2}\left(\frac{1}{k_n^4} - \frac{1}{k_0^4}\right) \ . \tag{4.33}$$

Setting $k_0 = m_\chi/3$, using $k_n = \sqrt{4m_\chi T}$ to match to numerical calculations, and enforcing $\tau_{\rm th} \geq 10^{10}$ years gives the final result for $\tilde{G}(m_\chi)$. Our numerical and analytic results are shown in fig. 4.2 along with previous results for comparison.[6] Note that the result shown

[6]With regards to the dark matter energy densities used in fig. 4.2, many pulsars have been observed in globular clusters [318] which can have dark matter densities as large as $\rho_\chi \sim 800$ GeV/cm^3 (or perhaps larger) as predicted for the globular cluster M4 [319]. However the presence of such large dark matter densities in globular clusters is uncertain—see also ref. [320].

from ref. [284] is their full analytic result and not the approximation that they plot in their figures.

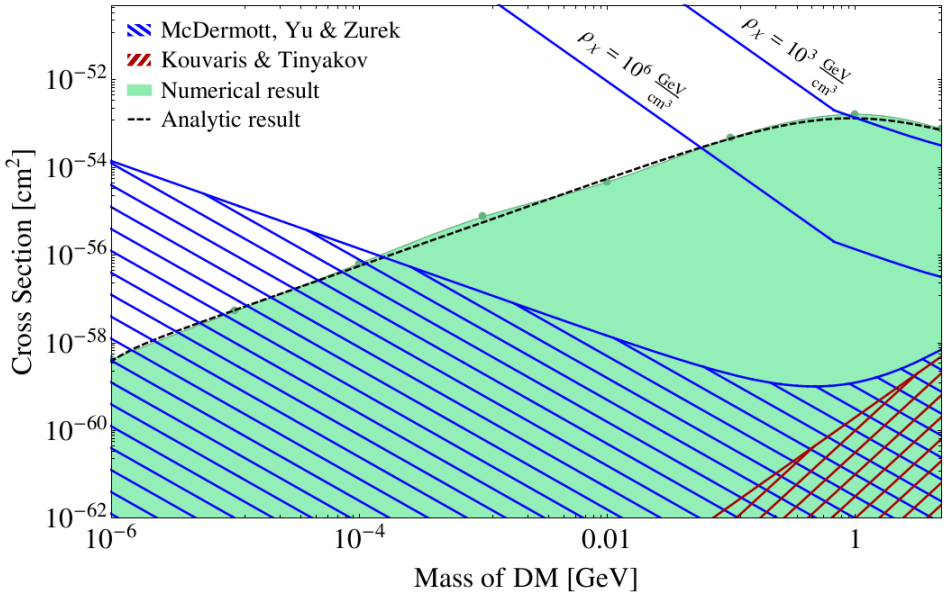

Figure 4.2: Plot of the constraints on the dark matter-neutron cross section for dark matter interacting with a Fermi gas of neutrons from enforcing that $\tau_{\rm th} \geq 10^{10}$ years. Shaded regions are allowed (where dark matter takes longer than 10^{10} years to thermalize). The solid green region is our result, the blue lined region is from ref. [284], and the red cross-hatched region is from ref. [280] (which is valid only for $m_\chi \gtrsim m_n$). Lines labeled with different values of ρ_χ (the dark matter density around a neutron star) indicate upper bounds on the allowed dark matter-neutron cross section due to neutron stars accreting enough dark matter to form a black hole as computed in ref. [284] in the absence of dark matter self-interactions.

In order to compare our thermalization time results with analytic expressions from previous literature ([280, 284]), we neglect k_0^{-4} with respect to k_n^{-4} in (4.33) and insert (4.24) into the expression to obtain

$$\tau_{\rm th} \approx \frac{105\pi^2}{16 m_n \sigma_{\chi n} T^2} \frac{\gamma}{(1+\gamma)^2} \ , \tag{4.34}$$

where $\gamma \equiv m_\chi / m_n$. To get a feel for typical scales, this can be recast as

$$\tau_{\rm th} \approx 3750 \text{ yrs } \frac{\gamma}{(1+\gamma)^2} \left(\frac{2 \times 10^{-45} \text{ cm}^2}{\sigma_{\chi n}} \right) \left(\frac{10^5 \text{ K}}{T} \right)^2 \ , \tag{4.35}$$

which can be longer than previous calculations by several orders of magnitude.

From fig. 4.2 one can see that the results obtained here differ appreciably from those in previous works—in particular some regions of dark matter parameter space that were disallowed in ref. [284] are allowed from this calculation due to an increase in thermalization times. This is because the proper inclusion of kinematics and Pauli blocking are essential for calculating the low energy and momentum transfer scattering processes that lead to thermalization. In the past Pauli blocking has been included only roughly, and related kinematic effects have been neglected. We note that the change in the behavior of these cross sections around $m_\chi = m_n$ is attributable in our case to the dependence of $\sigma_{\chi n}$ on the dark matter-nucleon reduced mass. In the case of ref. [284], the turnover is due to the assumption that typical momentum exchanges in dark matter-nucleon collisions will be proportional to m_r, which is an expectation based on non-relativistic collisions that does not properly take into account complications from scattering off a degenerate gas. If instead we neglect the m_χ dependence in our cross section, then the dependence of $\tau_{\rm th}$ on m_χ can be seen from (4.33) with $k_0 = m_\chi/3$ and $k_n = \sqrt{4m_\chi T}$. Suprisingly, we find that for a cross section independent of m_χ, the thermalization time increases as m_χ decreases. However, this is just a manifestation of the fact that lighter dark matter must reach a smaller momentum ($\sim \sqrt{m_\chi T}$) to be considered thermal, and it is these low momentum transfer collisions that take the longest to happen.

To estimate the contribution of Pauli blocking and kinematic constraints to our calculations we define an effective suppression factor $\xi_{\rm eff}$, given by

$$\xi_{\rm eff} = \frac{\Gamma}{n_n \sigma_{\chi n} v} \ , \tag{4.36}$$

where $n_n \sigma_{\chi n} v$ is the classical expression for the scattering rate, $n_n = p_F^3/(3\pi^2)$ is the number density of the neutrons, $\sigma_{\chi n}$ is the cross section given in (4.24) for dark matter-neutron scattering, and v is the magnitude of the relative velocity between the incident dark matter and incident neutron. Γ (4.16) is the actual scattering rate which is an integrated version of

$n\sigma v$. Using (4.24), (4.30) after integrating over k', and using a thermal $k = \sqrt{6m_\chi T}$ for the incident dark matter momentum, we find

$$\xi_{\text{eff}} \approx \frac{18T^2(m_\chi + m_n)^2}{5p_F^3 m_\chi \left|\sqrt{\frac{6T}{m_\chi}} - \frac{k_F}{m_n}\right|} \ . \tag{4.37}$$

In fig. 4.3 we compare our suppression factor to the Pauli blocking suppression factor used in ref. [284]. Figure 4.3 shows that the inclusion of Pauli blocking and kinematic effects

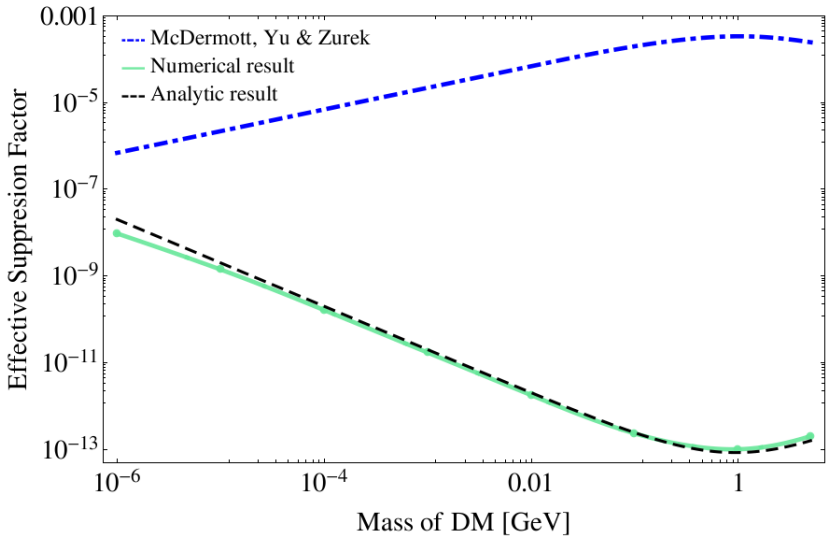

Figure 4.3: Comparison of effective suppression factors in the dark matter-neutron scattering rate for roughly thermal dark matter ($E = 3T$) and a non-interacting Fermi gas of neutrons.

in the properly integrated scattering rate, as well as the inclusion of dark matter mass dependence in the cross section, makes a difference. In what we have considered so far, these scattering kinematics and Pauli blocking are unique to dark matter scattering with a non-interacting, non-relativistic Fermi gas and will change once interactions between the fermions are included, especially in the case of attractive interactions which can give rise to superfluidity or superconductivity. We discuss these effects next.

4.4.3 Scattering with Superfluid Neutrons

Given an interacting Fermi gas, from BCS theory it is known that attractive interactions at the Fermi surface leads to the formation of Cooper pairs at low temperature and results in a phase transition to either a superfluid or superconducting state [316]. In this superfluid or superconducting state, there is a non-zero ground state expectation value (or condensate) of Cooper pairs which produces a gap in the fermion excitation spectrum and a Goldstone boson due to the spontaneous breaking of the $U(1)$ symmetry associated with fermion number [316, 321].

For neutrons in the core of the neutron star the dominant attractive interaction is in the p-wave channel and is expected to lead to the formation of spin-triplet Cooper pairs [314]. Model calculations predict that the energy gap $\Delta_{^3\mathrm{P}_2}$ is roughly $0.01 - 0.1$ MeV, though this remains somewhat uncertain [322]. The condensate of these Cooper pairs is expected to be spatially anisotropic and Goldstone bosons associated with the breaking of rotational invariance arise in addition to the Goldstone boson from the spontaneous breaking of fermion number [323]. Since in our model, dark matter couples only to the neutron density in the non-relativistic limit (in (4.19), $\mathcal{L}_{\mu\nu} \to 4m_\chi^2 \delta_{\mu 0}\delta_{\nu 0}$), the only relevant excitation at energies small compared to the gap is the Goldstone boson, or superfluid phonon, associated the breaking of the $U(1)$ fermion number symmetry.

The superfluid phonon manifests as spikes in the density-density neutron response function ($\sim \mathrm{Im}[\Pi^R_{00}]$, c.f. (4.20)) at $|q_0| = c_s q$, where c_s is the speed of the superfluid phonon in the nuclear medium. Based on this, we can make an ansatz for the neutron response function:

$$S(q_0, q) = A\delta(q_0 - c_s q) + B\delta(q_0 + c_s q) \ , \tag{4.38}$$

where A and B are normalization constants which can be fixed by enforcing the principle of detailed balance and the f-sum rule [324]

$$S(q_0, q) = e^{q_0/T} S(-q_0, q) \quad \text{and} \quad \frac{1}{2\pi}\int_{-\infty}^{\infty} dq_0 q_0 (1 - e^{-q_0/T}) S(q_0, q) = \frac{q^2}{m_n} n_n \ . \tag{4.39}$$

This gives

$$S(q_0, q) = \frac{\pi n_n q}{m_n c_s} \left[\frac{\delta(q_0 - c_s q)}{1 - e^{-q_0/T}} + \frac{\delta(q_0 + c_s q)}{e^{-q_0/T} - 1} \right] . \tag{4.40}$$

In our calculations we will only use the part of $S \propto \delta(q_0 - c_s q)$ which allows the dark matter to lose energy. The term $\propto \delta(q_0 + c_s q)$ is also suppressed for thermalization scatterings with $|q_0| > T$. We take

$$S(q_0, q) \approx \frac{\pi n_n q}{m_n c_s} \left[\frac{\delta(q_0 - c_s q)}{1 - e^{-q_0/T}} \right] . \tag{4.41}$$

Note that this response function only characterizes dark matter emission of a single phonon. Multi-phonon processes are highly suppressed and will be discussed in sec. 4.4.5. This response function can be used in place of the neutron part of the scattering rate in (4.16) and then the dark matter thermalization time in a neutron superfluid can be computed. In doing so, we varied c_s between $0.5 v_F/\sqrt{3}$ and $3 v_F/\sqrt{3}$. The value $v_F/\sqrt{3}$ is the leading order speed of the superfluid phonon [325]. In general $c_s = \sqrt{\partial P/\partial \rho}$, where P is the pressure in the nuclear medium and ρ is the energy density; c_s is expected to vary inside the neutron star due to phonon interactions and as a function of density.

We find in general that dark matter particles will only scatter with the neutron superfluid once or twice, leaving the dark matter with too much energy to be considered thermal. This result is due to the highly restricted kinematics of the neutron superfluid, as illustrated in fig. 4.4. Since the single phonon mode can only respond with $q_0 = c_s q$, once the dark matter particle loses enough energy such that $v_\chi < c_s$, the neutron superfluid and dark matter kinematics are no longer compatible and no further scattering can occur.

Since dark matter cannot thermalize by single phonon emission in the neutron superfluid, the dark matter particle must scatter with something else inside the neutron star in order to thermalize. In addition to suppressed multi-phonon scattering, the other options are scattering with protons or electrons. The protons are likely to be in a superconducting state with Cooper-paired protons and a massless, coupled proton and electron mode [326]. These paired protons have a gapped energy spectrum and hence, as in the case of superfluid neutrons, do not contribute much to dark matter thermalization. The massless proton-

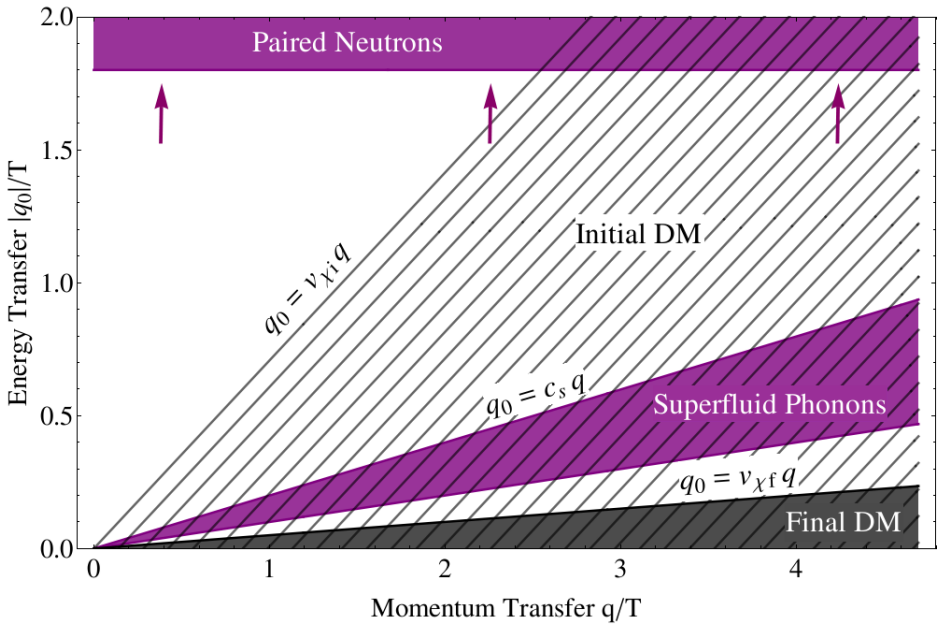

Figure 4.4: Plot of dark matter and neutron superfluid kinematically allowed regions. The neutron superfluid region includes a kinematic region for the phonon mode as well as one for neutron-pair interactions which begins at $q_0/T \sim 10^3$ on this scale. If dark matter is travelling at a speed larger than the speed of the superfluid phonon, the dark matter and neutron superfluid kinematic regions overlap and scattering can occur. However after dark matter scatters and loses energy, its speed decreases and the dark matter and neutron superfluid kinematic regions no longer overlap and no more scattering can occur.

electron mode has kinematics similar to that of the neutron superfluid phonon mode, and so it also does not allow dark matter to thermalize. This only leaves the electrons to thermalize the dark matter.

4.4.4 Scattering with a Fermi Gas of Electrons

Electrons in a neutron star have a vanishingly small critical temperature for pairing, so the low-energy spectrum of particle-hole excitations is un-gapped and well described by that of a non-interacting Fermi gas. Thus electron-dark matter scattering can be treated in the same way as neutron-dark matter scattering in sec. 4.4.2. Roughly 7% of the number density a neutron star is made up of electrons, and for neutrons at saturation density, electrons have

a chemical potential of $\mu_e \approx 0.12$ GeV, indicating that the electrons are highly relativistic with a Fermi velocity $v_F \approx 1$. Since dark matter is non-relativistic, its dominant coupling is to the electron density (similar to the neutron scattering case) but the kinematics differs qualitatively from the neutron case because $v_F \approx 1$ meaning dark matter-electron scattering is never kinematically suppressed by electron kinematics inside the neutron star.

The electron response function to leading order in the velocity of the dark matter particle is given by

$$S(q_0, q) = \int \frac{d^3p}{(2\pi)^3} \int \frac{d^3p'}{(2\pi)^3} \Big[(2\pi)^4 \delta^4(p^\mu + k^\mu - p'^\mu - k'^\mu)(1 + \cos\theta) \times n_F(E_p^n) \left(1 - n_F(E_{p'}^n)\right) \Big] , \tag{4.42}$$

where $n_F(E) = [1 + e^{(E-\mu)/T}]^{-1}$ is the electron Fermi-Dirac distribution function and θ is the angle between $\vec{p}$ and $\vec{p}'$. In fig. 4.5 we show the numerical results obtained from setting $\tau \geq 10^{10}$ years (using (4.18),(4.21), and (4.24)) for the low energy dark matter-electron cross section as a function of dark matter mass. The dark matter-neutron cross section results are plotted for comparison. Interestingly, if dark matter couples with equal strength to neutrons and electrons (i.e. if $\tilde{G}$ is fixed), then we find that thermalization times for dark matter scattering with electrons are roughly 50% of thermalization times for dark matter scattering with neutrons, so regardless of the presence of a superfluid, dark matter-electron scattering would be the most efficient process for dark matter thermalization.

4.4.5 Scattering in Exotic Neutron Star Cores

So far we have considered dark matter thermalization with electrons and also neutrons, both in the normal phase and in the superfluid phase. However, the phase structure of matter in the neutron star core remains uncertain [313]. In this section we study two specific phases of high density matter in order to explore their influence on dark matter thermalization. At asymptotically large densities where the strange quark mass can be considered small and

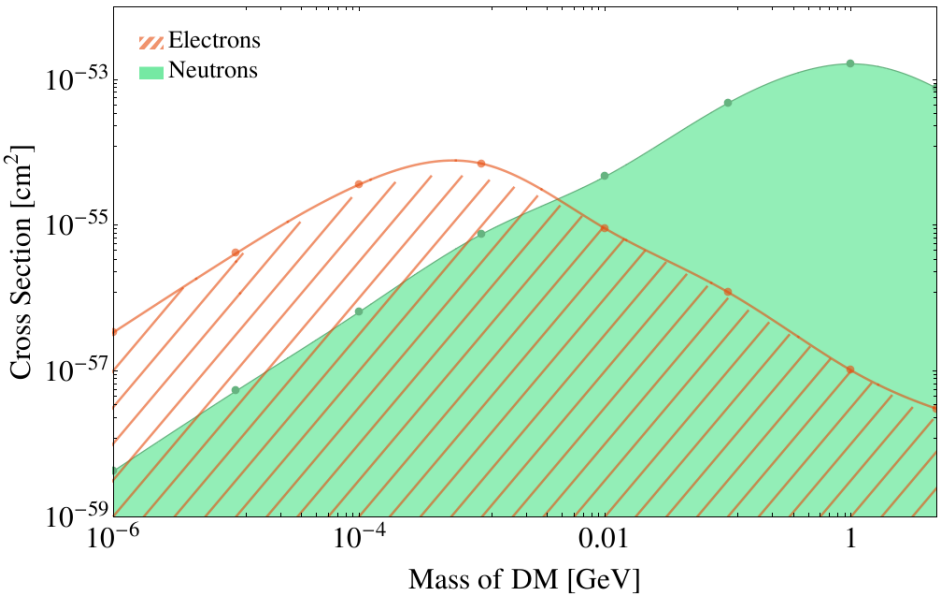

Figure 4.5: Plot of the low energy dark matter-neutron and dark matter-electron cross sections as a function of dark matter mass. Shaded areas are regions where dark matter thermalization takes longer than 10^{10} years.

perturbation theory is applicable, it is now well established on theoretical grounds that the ground state of quark matter is the color flavor locked (CFL) phase in which the $SU(3)_C \times SU(3)_L \times SU(3)_R \times U(1)_B$ approximate symmetry of QCD is spontaneously broken down to its vector subgroup $SU(3)_{C+L+R}$ due to the formation of a condensate of di-quark pairs [327,328]. This is a color superconducting phase in which all nine (3 flavors $\times$ 3 colors) light quarks form Cooper pairs and there is a gap in the particle-hole excitation spectrum.

At densities of relevance to neutron stars, the strange quark mass is dynamically important, perturbation theory fails, and whether the CFL phase is present at these densities remains an open question. If it were present, the CFL phase could additionally contain a condensate of K^0 mesons [329, 330]. Both the CFL and the CFLK^0 phases are characterized by similar low energy properties at temperatures of relevance to old neutron stars. They are both devoid of electrons and the only relevant low energy degrees of freedom are the massless Goldstone bosons associated with the breaking of global symmetries in the ground

state [327, 328]. There is one massless phonon mode, sometimes called the h boson, due to the breaking of the $U(1)_B$ symmetry in the CFL phase and two massless phonon modes in the CFLK^0 phase, one due to the breaking of $U(1)_B$ (called h) and another due to the breaking of the hypercharge symmetry by the K^0 condensate (called K_1). The velocity of the h mode in the relativistic limit is approximately given by $c_h \simeq 1/\sqrt{3}$ and the velocity of the K_1 is $c_{K_1} \simeq \sin\theta/\sqrt{3+9\cos^2\theta}$ where $\sin\theta$ is proportional to the number density of the kaon condensate [330].

Earlier we found that the gap in the nucleon spectrum due to pairing implied that dark matter thermalization would proceed via superfluid phonon emission processes as long as $v_\chi > c_s$, where c_s was the speed of the Goldstone mode in the nuclear medium. For $v_\chi < c_s$, this process is kinematically forbidden and electron scattering dominates. In the CFL and CFLK^0 phases, electrons are absent and relevant dark matter thermalization processes can only involve the massless Goldstone bosons. As in the superfluid nuclear phase, thermalization in the CFL and CFLK^0 phases proceeds by the phonon emission process shown in the second diagram in fig. 4.6 (akin to the Cherenkov radiation of fast particles) as long as $v_\chi > c_h$ if dark matter couples to the baryon number current and $v_\chi > c_{K_1}$ if it also couples to the hypercharge current.

When $v_\chi < c_h$, dark matter thermalization cannot proceed by phonon emission and the dominant thermalization process is the two phonon process shown by the third diagram in fig. 4.6. Here, the initial state phonon is thermal with energy $p_0 = c_h p \sim T$, and the intermediate phonon is off-shell. For simplicity we will consider dark matter that couples only to the baryon number. In this case, the low energy effective Lagrangian has the form $\mathcal{L}_{\text{eff}} = \tilde{G} f_h l^0(\partial_0\phi - c_h\partial_i\phi)$ where ϕ is half of the overall phase of the condensate that breaks the $U(1)_B$ symmetry and $f_h \simeq \mu_q$ where $\mu_q \simeq 400$ MeV is the quark chemical potential in the neutron star core [331]. Then the amplitude for the dark matter + phonon $\rightarrow$ dark matter + phonon process can be approximated by

$$\mathcal{M} \approx -4i\frac{\tilde{G}c_3 m_\chi^2}{f_h}\,\frac{q_0^2 p_0 p_0'}{c_h^2 q^2}\ , \tag{4.43}$$

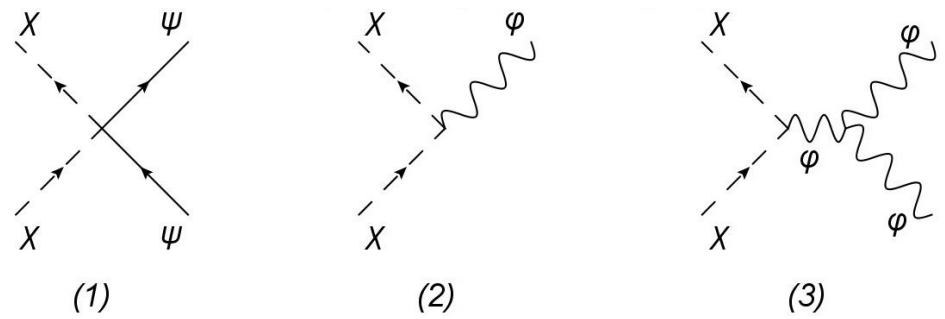

Figure 4.6: Scattering processes which contribute to dark matter thermalization inside a neutron star. χ denotes dark matter, ψ is a neutron or electron, and ϕ is a superfluid phonon. (1) shows dark matter scattering with a non-interacting neutron or electron, (2) is dark matter scattering by emission of a single phonon, and (3) shows dark matter scattering with a thermal phonon.

where c_3 is the dimensionless constant that sets the strength of the leading order three phonon vertex $\simeq c_3\ (\partial_0\phi)^3/f_h^2$ in the low energy theory, q_0 is the energy of the intermediate phonon, q is the magnitude of the momentum of the intermediate phonon, and p_0 and p_0' are the initial and final phonon energies respectively. We used an approximate form of the phonon propagator $\sim (q_0^2 - c_h^2 q^2)^{-1} \approx -(c_h^2 q^2)^{-1}$, since the relevant phonon kinematics are off-shell with $|q_0| < c_h q$.

Using (4.43), the scattering rate can be calculated for arbitrary initial dark matter velocities and to first order in v_χ/c_h. Taking typical values for our parameters: $p_0 \sim T$, $p_0' \sim T$, $q_0 \sim \frac{v_\chi}{c_h} T$, and $q \sim T/c_h$, we find that the dimensional estimate (ignoring factors of 2 and π) for the dark matter-phonon scattering rate is given by

$$\Gamma \approx \left(\frac{\tilde{G} c_3}{f_h}\right)^2 \frac{v_\chi^3 T^7}{c_h^6}\ . \tag{4.44}$$

Using $c_h \sim 1/\sqrt{3}$, $c_3 \sim 1$ and $v_\chi \sim 1/3$ in (4.44) for a single dark matter-phonon scattering process, and estimating $\tau \approx 1/\Gamma$, we find that the dark matter thermalization time is

approximately

$$\tau \approx 9 \times 10^{38} \text{ yrs } \left(\frac{\text{GeV}^2}{\tilde{G}}\right)^2 \left(\frac{10^5 \text{ K}}{T}\right)^7 , \tag{4.45}$$

indicating that the dark matter scattering rate is too low to allow for thermalization even for the oldest neutron stars with ages $\sim 10^{10}$ years if the core contains either the CFL or CFLK^0 phase.

4.5 Summary

We considered a relatively generic dark matter model in which the dark matter particle was an asymmetric, complex scalar that coupled to regular matter via some heavy vector boson, with the regular matter vector and axial-vector couplings to the heavy mediator taken to be those to the Z^0 boson. As an example of such dark matter, we discussed the case of asymmetric, mixed sneutrino dark matter. We calculated dark matter thermalization times inside of a neutron star for dark matter scattering with electrons, neutrons in the normal phase, neutrons in the superfluid phase, and color superconducting quark matter.

We found several important results. Properly including kinematics, Pauli-blocking, and dark matter mass dependence in the cross section, resulted in dark matter thermalization times that were qualitatively different from past results. We also pointed out that previously neglected dark matter-electron scattering in ordinary neutron star cores is actually quite important. We found dark matter-electron scattering to be a more efficent dark matter thermalization mechanism than dark matter-neutron scattering when the neutrons are in a non-superfluid state (for a fixed $\tilde{G}$) and it is the *only* relevant dark matter thermalization mechanism when the neutrons form a superfluid and the protons form a superconductor. Finally, the presence of exotic neutron star cores with color superconducting quark matter and no electrons give rise dark matter thermalization times larger than the age of the Universe which protects neutron stars from their possible destruction as a result of dark matter accretion. An interesting consequence of this is that if asymmetric, bosonic dark matter is discovered (and we find no lacking number of very old neutron stars), it motivates the exis-

tence of exotic neutron star cores which can protect neutron stars from an untimely death by a dark matter black hole.

Chapter 5
CONCLUSIONS

Even though the first proposal of dark matter was a century ago, we still have yet to understand the nature of dark matter. There have been enormous theoretical and experimental efforts to further our understanding, which has helped to rule out large areas of dark matter parameter space. However, as we saw in chp. 3, even some types of extremely strong dark matter interactions with standard model particles are still viable.

In this thesis we discussed three theories of non-gravitational interactions of dark matter which can be studied using particle astrophysics: WIMP-motivated dark matter annihilations into standard model particles in subhalos, dark matter-neutrino interactions which can address the missing satellite problem, and asymmetric dark matter-nucleon interactions in neutron stars. Many other ideas about dark matter exist and the coming years will be exciting as numerical simulations of the ΛCDM model continue to improve and more accurately include the effects of baryonic feedback, and as more sensitive experimental results continue to be produced.

To name a few, the results of the second run of the LHC at 14 TeV, the results from the upgraded, generation-2 dark matter direct detection experiments XENON 1T, LZ, SuperCDMS, and ADMX-Gen2, potential dwarf galaxy discoveries by DES, astrophysical antideuteron measurements from GAPS, dark matter maps from LSST, sensitive neutrino measurements from Hyper-K, IceCube, and DUNE, continually improved data sets from the Fermi Large Area Telescope, and high energy gamma-ray observations from GAMMA-400 (as well as many other sources of data) will all contribute to furthering our understanding of dark matter.

BIBLIOGRAPHY

[1] J. Einasto, *Dark Matter*, *ArXiv e-prints* (Jan., 2009) [arXiv:0901.0632].

[2] J. Einasto, *Dark Matter*, *Baltic Astronomy* **20** (2011) 231–240, [arXiv:1109.5580].

[3] K. Kuijken and G. Gilmore, *The mass distribution in the galactic disc – ii. determination of the surface mass density of the galactic disc near the sun*, *Monthly Notices of the Royal Astronomical Society* **239** (1989), no. 2 605–649, [http://mnras.oxfordjournals.org/content/239/2/605.full.pdf+html].

[4] G. Gilmore, R. F. G. Wyse, and K. Kuijken, *Kinematics, chemistry, and structure of the Galaxy*, **27** (1989) 555–627.

[5] J. I. Read, *The local dark matter density*, *Journal of Physics G Nuclear Physics* **41** (June, 2014) 063101, [arXiv:1404.1938].

[6] J. Bovy and S. Tremaine, *On the Local Dark Matter Density*, **756** (Sept., 2012) 89, [arXiv:1205.4033].

[7] F. Zwicky, *Die Rotverschiebung von extragalaktischen Nebeln*, *Helvetica Physica Acta* **6** (1933) 110–127.

[8] F. D. Kahn and L. Woltjer, *Intergalactic Matter and the Galaxy.*, **130** (Nov., 1959) 705.

[9] M. Schmidt, *A model of the distribution of mass in the Galactic System*, **13** (June, 1956) 15.

[10] H. W. Babcock, *The rotation of the Andromeda Nebula*, *Lick Observatory Bulletin* **19** (1939) 41–51.

[11] J. H. Oort, *Some Problems Concerning the Structure and Dynamics of the Galactic System and the Elliptical Nebulae NGC 3115 and 4494.*, **91** (Apr., 1940) 273.

[12] V. C. Rubin and W. K. Ford, Jr., *Rotation of the Andromeda Nebula from a Spectroscopic Survey of Emission Regions*, **159** (Feb., 1970) 379.

[13] M. S. Roberts and R. N. Whitehurst, *The rotation curve and geometry of M31 at large galactocentric distances.*, **201** (Oct., 1975) 327–346.

[14] M. S. Roberts and A. H. Rots, *Comparison of Rotation Curves of Different Galaxy Types*, **26** (Aug., 1973) 483–485.

[15] D. H. Rogstad and G. S. Shostak, *Gross Properties of Five Scd Galaxies as Determined from 21-CENTIMETER Observations*, **176** (Sept., 1972) 315.

[16] M. S. Roberts, *The Rotation Curve of Galaxies*, in *Dynamics of the Solar Systems* (A. Hayli, ed.), vol. 69 of *IAU Symposium*, p. 331, 1975.

[17] V. C. Rubin, N. Thonnard, and W. K. Ford, Jr., *Extended rotation curves of high-luminosity spiral galaxies. IV - Systematic dynamical properties, SA through SC*, **225** (Nov., 1978) L107–L111.

[18] A. Davidsen, S. Bowyer, and W. Welch, *Observational Evidence that the Coma Cluster is not Bound by Ionized Intracluster Gas*, **186** (Dec., 1973) L119.

[19] D. J. Hegyi and K. A. Olive, *Can galactic halos be made of baryons?*, *Physics Letters B* **126** (1983), no. 1–2 28 – 32.

[20] B. V. Komberg and I. D. Novikov, *Nature of the halos of spiral galaxies*, *Soviet Astronomy Letters* **1** (Apr., 1975) 47.

[21] **MACHO** Collaboration, C. Alcock et al., *The MACHO project: Microlensing results from 5.7 years of LMC observations*, *Astrophys.J.* **542** (2000) 281–307, [astro-ph/0001272].

[22] **EROS-2** Collaboration, P. Tisserand et al., *Limits on the Macho Content of the Galactic Halo from the EROS-2 Survey of the Magellanic Clouds*, *Astron. Astrophys.* **469** (2007) 387–404, [astro-ph/0607207].

[23] Y. N. Parijskij, *Search for Primordial Perturbations of the Universe: Observations with RATAN-600 Radio Telescope*, in *Large Scale Structures in the Universe* (M. S. Longair and J. Einasto, eds.), vol. 79 of *IAU Symposium*, p. 315, 1978.

[24] A. G. Doroshkevich, M. Y. Khlopov, R. A. Sunyaev, A. S. Szalay, and Y. B. Zeldovich, *Cosmological impact of the neutrino rest mass*, *Annals of the New York Academy of Sciences* **375** (1981), no. 1 32–42.

[25] I. B. Zeldovich, J. Einasto, and S. Shandarin, *Giant voids in the universe*, *Nature* **300** (1982) 407–413.

[26] S. D. M. White, C. S. Frenk, and M. Davis, *Clustering in a neutrino-dominated universe*, **274** (Nov., 1983) L1–L5.

[27] G. R. Blumenthal, *Formation of galaxies and large-scale structure with cold dark matter*, *NATURE* **311** (1984) 11.

[28] M. Milgrom, *A modification of the Newtonian dynamics as a possible alternative to the hidden mass hypothesis*, **270** (July, 1983) 365–370.

[29] J. Bekenstein and M. Milgrom, *Does the missing mass problem signal the breakdown of Newtonian gravity?*, **286** (Nov., 1984) 7–14.

[30] B. Famaey and S. McGaugh, *Challenges for λcdm and mond*, in *Journal of Physics: Conference Series*, vol. 437, p. 012001, IOP Publishing, 2013.

[31] L. S. The and S. D. M. White, *Modified Newtonian dynamics and the Coma cluster*, **95** (June, 1988) 1642–1646.

[32] R. Ibata, A. Sollima, C. Nipoti, M. Bellazzini, S. C. Chapman, and E. Dalessandro, *Polytropic model fits to the globular cluster ngc 2419 in modified newtonian dynamics*, *The Astrophysical Journal* **743** (2011), no. 1 43.

[33] J. D. Bekenstein, *Relativistic gravitation theory for the modified newtonian dynamics paradigm*, *Phys. Rev. D* **70** (Oct, 2004) 083509.

[34] C. Skordis, D. F. Mota, P. G. Ferreira, and C. Bœhm, *Large scale structure in bekenstein's theory of relativistic modified newtonian dynamics*, *Phys. Rev. Lett.* **96** (Jan, 2006) 011301.

[35] **Planck** Collaboration, P. Ade et al., *Planck 2015 results. XIII. Cosmological parameters*, `arXiv:1502.0158`.

[36] D. Clowe, M. Bradac, A. H. Gonzalez, M. Markevitch, S. W. Randall, et al., *A direct empirical proof of the existence of dark matter*, *Astrophys.J.* **648** (2006) L109–L113, [`astro-ph/0608407`].

[37] Eisenstein et al., *Detection of the baryon acoustic peak in the large-scale correlation function of sdss luminous red galaxies*, *The Astrophysical Journal* **633** (2005), no. 2 560.

[38] D. Harvey, R. Massey, T. Kitching, A. Taylor, and E. Tittley, *The non-gravitational interactions of dark matter in colliding galaxy clusters*, *Science* **347** (2015), no. 6229 1462–1465, [arXiv:1503.0767].

[39] B. D. Fields, *The Primordial Lithium Problem*, *Annual Review of Nuclear and Particle Science* **61** (Nov., 2011) 47–68, [arXiv:1203.3551].

[40] S. Weinberg, *Cosmology*. Oxford University Press Inc., New York, 2008.

[41] S. Ryan, T. Beers, K. A. Olive, B. Fields, and J. Norris, *Primordial lithium and big bang nucleosynthesis*, astro-ph/9905211.

[42] L. Sbordone et al., *The metal-poor end of the spite plateau-i. stellar parameters, metallicities, and lithium abundances*, *Astronomy & astrophysics* **522** (2010) A26.

[43] A. Coc, J.-P. Uzan, and E. Vangioni, *Standard Big-Bang Nucleosynthesis after Planck*, arXiv:1307.6955.

[44] D. H. Weinberg, J. S. Bullock, F. Governato, R. K. de Naray, and A. H. G. Peter, *Cold dark matter: controversies on small scales*, arXiv:1306.0913.

[45] A. Brooks, *Re-Examining Astrophysical Constraints on the Dark Matter Model*, *Annalen Phys.* **526** (2014), no. 7-8 294–308, [arXiv:1407.7544].

[46] J. F. Navarro, C. S. Frenk, and S. D. White, *A Universal density profile from hierarchical clustering*, *Astrophys. J.* **490** (1997) 493–508, [astro-ph/9611107].

[47] S.-H. Oh, W. de Blok, E. Brinks, F. Walter, and J. Kennicutt, Robert C., *Dark and luminous matter in THINGS dwarf galaxies*, *Astron. J.* **141** (2011) 193, [arXiv:1011.0899].

[48] F. Governato, C. Brook, L. Mayer, A. Brooks, G. Rhee, et al., *At the heart of the matter: the origin of bulgeless dwarf galaxies and Dark Matter cores*, *Nature* **463** (2010) 203–206, [arXiv:0911.2237].

[49] F. Governato, A. Zolotov, A. Pontzen, C. Christensen, S. Oh, et al., *Cuspy No More: How Outflows Affect the Central Dark Matter and Baryon Distribution in Lambda CDM Galaxies*, *Mon. Not. Roy. Astron. Soc.* **422** (2012) 1231–1240, [arXiv:1202.0554].

[50] R. Teyssier, A. Pontzen, Y. Dubois, and J. Read, *Cusp-core transformations in dwarf galaxies: observational predictions*, arXiv:1206.4895.

[51] A. Zolotov, A. M. Brooks, B. Willman, F. Governato, A. Pontzen, et al., *Baryons Matter: Why Luminous Satellite Galaxies Have Reduced Central Masses*, *Astrophys. J.* **761** (2012) 71, [arXiv:1207.0007].

[52] P. Madau, S. Shen, and F. Governato, *Dark Matter Heating and Early Core Formation in Dwarf Galaxies*, *Astrophys. J.* **789** (2014) L17, [arXiv:1405.2577].

[53] A. Pontzen and F. Governato, *How supernova feedback turns dark matter cusps into cores*, *Mon. Not. Roy. Astron. Soc.* **421** (2012) 3464, [arXiv:1106.0499].

[54] J. Penarrubia, A. Pontzen, M. G. Walker, and S. E. Koposov, *The coupling between the core/cusp and missing satellite problems*, *Astrophys. J.* **759** (2012) L42, [arXiv:1207.2772].

[55] S. Garrison-Kimmel, M. Rocha, M. Boylan-Kolchin, J. Bullock, and J. Lally, *Can Feedback Solve the Too Big to Fail Problem?*, arXiv:1301.3137.

[56] M. A. Breddels, C. Vera-Ciro, and A. Helmi, *Matching the dark matter profiles of dSph galaxies with those of simulated satellites: a two parameter comparison*, *ArXiv e-prints* (July, 2015) [arXiv:1507.0399].

[57] A. A. Klypin, A. V. Kravtsov, O. Valenzuela, and F. Prada, *Where are the missing Galactic satellites?*, *Astrophys. J.* **522** (1999) 82–92, [astro-ph/9901240].

[58] B. Moore, S. Ghigna, F. Governato, G. Lake, T. R. Quinn, et al., *Dark matter substructure within galactic halos*, *Astrophys. J.* **524** (1999) L19–L22, [astro-ph/9907411].

[59] J. S. Bullock, *Notes on the Missing Satellites Problem*, *ArXiv e-prints* (Sept., 2010) [arXiv:1009.4505].

[60] E. J. Tollerud, J. S. Bullock, L. E. Strigari, and B. Willman, *Hundreds of Milky Way Satellites? Luminosity Bias in the Satellite Luminosity Function*, *Astrophys.J.* **688** (2008) 277–289, [arXiv:0806.4381].

[61] A. S. Font, A. J. Benson, R. G. Bower, C. F. Frenk, A. P. Cooper, et al., *The population of Milky Way satellites in the ΛCDM cosmology*, *Mon. Not. Roy. Astron. Soc.* **417** (2011) 1260, [arXiv:1103.0024].

[62] G. Ogiya and A. Burkert, *Re-examining the Too-Big-To-Fail Problem for Dark Matter Haloes with Central Density Cores*, *ArXiv e-prints* (Aug., 2014) [arXiv:1408.6444].

[63] M. Boylan-Kolchin, J. S. Bullock, and M. Kaplinghat, *The Milky Way's bright satellites as an apparent failure of LCDM*, *Mon. Not. Roy. Astron. Soc.* **422** (2012) 1203–1218, [arXiv:1111.2048].

[64] J. F. Navarro and W. Benz, *Dynamics of cooling gas in galactic dark halos*, **380** (Oct., 1991) 320–329.

[65] J. F. Navarro and S. D. White, *Simulations of dissipative galaxy formation in hierarchically clustering universes–ii. dynamics of the baryonic component in galactic haloes*, *Monthly Notices of the Royal Astronomical Society* **267** (1994), no. 2 401–412.

[66] S. J. Kautsch, E. K. Grebel, F. D. Barazza, and I. Gallagher, John S., *A catalog of edge-on disk galaxies: from galaxies with a bulge to superthin galaxies*, *Astron.Astrophys.* **445** (2006) 765, [astro-ph/0509294].

[67] J. Kormendy, N. Drory, R. Bender, and M. E. Cornell, *Bulgeless Giant Galaxies Challenge Our Picture of Galaxy Formation by Hierarchical Clustering*, **723** (Nov., 2010) 54–80, [arXiv:1009.3015].

[68] F. Piontek and M. Steinmetz, *The modelling of feedback processes in cosmological simulations of disc galaxy formation*, **410** (Feb., 2011) 2625–2642, [arXiv:0909.4156].

[69] F. Governato, C. Brook, L. Mayer, A. Brooks, G. Rhee, J. Wadsley, P. Jonsson, B. Willman, G. Stinson, T. Quinn, et al., *Bulgeless dwarf galaxies and dark matter cores from supernova-driven outflows.*, *Nature* **463** (2010), no. 7278 203–206.

[70] C. B. Brook, F. Governato, R. Roškar, G. Stinson, A. M. Brooks, J. Wadsley, T. Quinn, B. K. Gibson, O. Snaith, K. Pilkington, E. House, and A. Pontzen, *Hierarchical formation of bulgeless galaxies: why outflows have low angular momentum*, **415** (Aug., 2011) 1051–1060, [arXiv:1010.1004].

[71] M. Metz, P. Kroupa, and H. Jerjen, *The spatial distribution of the Milky Way and Andromeda satellite galaxies*, *Mon.Not.Roy.Astron.Soc.* **374** (2007) 1125–1145, [astro-ph/0610933].

[72] R. A. Ibata, G. F. Lewis, A. R. Conn, M. J. Irwin, A. W. McConnachie, et al., *A Vast Thin Plane of Co-rotating Dwarf Galaxies Orbiting the Andromeda Galaxy*, *Nature* **493** (2013) 62–65, [arXiv:1301.0446].

[73] M. S. Pawlowski and S. S. McGaugh, *Co-orbiting planes of sub-halos are similarly unlikely around paired and isolated hosts*, *The Astrophysical Journal Letters* **789** (2014), no. 1 L24.

[74] M. S. Pawlowski, B. Famaey, H. Jerjen, D. Merritt, P. Kroupa, et al., *Co-orbiting satellite galaxy structures are still in conflict with the distribution of primordial dwarf galaxies*, *Mon.Not.Roy.Astron.Soc.* **442** (2014), no. 3 2362–2380, [arXiv:1406.1799].

[75] M. Cautun, S. Bose, C. S. Frenk, Q. Guo, J. Han, W. A. Hellwing, T. Sawala, and W. Wang, *Planes of satellite galaxies: when exceptions are the rule*, *ArXiv e-prints* (June, 2015) [arXiv:1506.0415].

[76] T. Buck, A. V. Macci'o, and A. A. Dutton, *Evidence for Early Filamentary Accretion from the Andromeda Galaxy's Thin Plane of Satellites*, *ArXiv e-prints* (Apr., 2015) [arXiv:1504.0519].

[77] G. Efstathiou, *H0 Revisited*, *Mon.Not.Roy.Astron.Soc.* **440** (2014), no. 2 1138–1152, [arXiv:1311.3461].

[78] **Planck** Collaboration, P. Ade et al., *Planck 2013 results. XX. Cosmology from Sunyaev–Zeldovich cluster counts*, *Astron.Astrophys.* **571** (2014) A20, [arXiv:1303.5080].

[79] O. Erken, P. Sikivie, H. Tam, and Q. Yang, *Axion Dark Matter and Cosmological Parameters*, *Phys.Rev.Lett.* **108** (2012) 061304, [arXiv:1104.4507].

[80] S. Dodelson and L. M. Widrow, *Sterile neutrinos as dark matter*, *Phys. Rev. Lett.* **72** (1994) 17–20, [hep-ph/9303287].

[81] S. Colombi, S. Dodelson, and L. M. Widrow, *Large scale structure tests of warm dark matter*, *Astrophys. J.* **458** (1996) 1, [astro-ph/9505029].

[82] D. N. Spergel and P. J. Steinhardt, *Observational evidence for selfinteracting cold dark matter*, *Phys. Rev. Lett.* **84** (2000) 3760–3763, [astro-ph/9909386].

[83] S. Tulin, H.-B. Yu, and K. M. Zurek, *Resonant Dark Forces and Small Scale Structure*, *Phys. Rev. Lett.* **110** (2013), no. 11 111301, [arXiv:1210.0900].

[84] S. Tulin, H.-B. Yu, and K. M. Zurek, *Beyond Collisionless Dark Matter: Particle Physics Dynamics for Dark Matter Halo Structure*, *Phys. Rev. D* **87** (2013), no. 11 115007, [arXiv:1302.3898].

[85] M. Kaplinghat, S. Tulin, and H.-B. Yu, *Self-interacting Dark Matter Benchmarks*, arXiv:1308.0618.

[86] C. Boehm, J. Schewtschenko, R. Wilkinson, C. Baugh, and S. Pascoli, *Using the Milky Way satellites to study interactions between cold dark matter and radiation*, *Mon. Not. Roy. Astron. Soc.* **445** (2014) L31–L35, [arXiv:1404.7012].

[87] I. M. Shoemaker, *Constraints on Dark Matter Protohalos in Effective Theories and Neutrinophilic Dark Matter*, *Phys. Dark Univ.* **2** (2013) 157–162, [arXiv:1305.1936].

[88] X. Chu and B. Dasgupta, *Dark Radiation Alleviates Problems with Dark Matter Halos*, *Phys.Rev.Lett.* **113** (2014), no. 16 161301, [arXiv:1404.6127].

[89] L. Randall and J. Scholtz, *Dissipative Dark Matter and the Andromeda Plane of Satellites*, arXiv:1412.1839.

[90] J. Sommer-Larsen and A. Dolgov, *Formation of Disk Galaxies: Warm Dark Matter and the Angular Momentum Problem*, **551** (Apr., 2001) 608–623, [astro-ph/9912166].

[91] P. Gondolo and G. Gelmini, *Cosmic abundances of stable particles: Improved analysis*, *Nuclear Physics B* **360** (1991), no. 1 145–179.

[92] L. J. Hall, K. Jedamzik, J. March-Russell, and S. M. West, *Freeze-In Production of FIMP Dark Matter*, *JHEP* **03** (2010) 080, [arXiv:0911.1120].

[93] I. Affleck and M. Dine, *A new mechanism for baryogenesis*, *Nuclear Physics B* **249** (1985), no. 2 361 – 380.

[94] J. Goodman, M. Ibe, A. Rajaraman, W. Shepherd, T. M. Tait, et al., *Constraints on Light Majorana dark Matter from Colliders*, *Phys.Lett.* **B695** (2011) 185–188, [arXiv:1005.1286].

[95] J. Goodman, M. Ibe, A. Rajaraman, W. Shepherd, T. M. Tait, et al., *Constraints on Dark Matter from Colliders*, *Phys.Rev.* **D82** (2010) 116010, [arXiv:1008.1783].

[96] **ATLAS** Collaboration, G. Aad et al., *Search for dark matter candidates and large extra dimensions in events with a photon and missing transverse momentum in pp collision data at $\sqrt{s} = 7$ TeV with the ATLAS detector*, *Phys.Rev.Lett.* **110** (2013), no. 1 011802, [arXiv:1209.4625].

[97] **CDF** Collaboration, T. Aaltonen et al., *A Search for dark matter in events with one jet and missing transverse energy in $p\bar{p}$ collisions at $\sqrt{s} = 1.96$ TeV*, *Phys.Rev.Lett.* **108** (2012) 211804, [arXiv:1203.0742].

[98] **CMS** Collaboration, S. Chatrchyan et al., *Search for Dark Matter and Large Extra Dimensions in pp Collisions Yielding a Photon and Missing Transverse Energy*, *Phys.Rev.Lett.* **108** (2012) 261803, [arXiv:1204.0821].

[99] R. Essig, J. Mardon, and T. Volansky, *Direct Detection of Sub-GeV Dark Matter*, *Phys. Rev.* **D85** (2012) 076007, [arXiv:1108.5383].

[100] P. J. Fox, J. Liu, and N. Weiner, *Integrating Out Astrophysical Uncertainties*, *Phys. Rev.* **D83** (2011) 103514, [arXiv:1011.1915].

[101] E. Del Nobile, G. Gelmini, P. Gondolo, and J.-H. Huh, *Generalized Halo Independent Comparison of Direct Dark Matter Detection Data*, *JCAP* **1310** (2013) 048, [arXiv:1306.5273].

[102] A. L. Fitzpatrick, W. Haxton, E. Katz, N. Lubbers, and Y. Xu, *The Effective Field Theory of Dark Matter Direct Detection*, *JCAP* **1302** (2013) 004, [arXiv:1203.3542].

[103] J. L. Feng, J. Kumar, D. Marfatia, and D. Sanford, *Isospin-Violating Dark Matter*, *Phys. Lett.* **B703** (2011) 124–127, [arXiv:1102.4331].

[104] P. W. Graham, R. Harnik, S. Rajendran, and P. Saraswat, *Exothermic Dark Matter*, *Phys. Rev.* **D82** (2010) 063512, [arXiv:1004.0937].

[105] R. e. a. "Bernabei, *Final model independent result of dama/libra–phase1*, *The European Physical Journal C* **73** (2013), no. 12.

[106] C. Aalseth, P. Barbeau, J. Colaresi, J. D. Leon, J. Fast, et al., *Maximum Likelihood Signal Extraction Method Applied to 3.4 years of CoGeNT Data*, arXiv:1401.6234.

[107] **CDMS** Collaboration, R. Agnese et al., *Silicon Detector Dark Matter Results from the Final Exposure of CDMS II*, *Phys.Rev.Lett.* **111** (2013), no. 25 251301, [arXiv:1304.4279].

[108] **CRESST-II** Collaboration, G. Angloher et al., *Results on low mass WIMPs using an upgraded CRESST-II detector*, *Eur.Phys.J.* **C74** (2014), no. 12 3184, [arXiv:1407.3146].

[109] **LUX** Collaboration, M. Horn et al., *Results from the LUX dark matter experiment*, *Nucl.Instrum.Meth.* **A784** (2015) 504–507.

[110] D. P. Finkbeiner and N. Weiner, *Exciting Dark Matter and the INTEGRAL/SPI 511 keV signal*, *Phys. Rev.* **D76** (2007) 083519, [astro-ph/0702587].

[111] Y. Ascasibar, P. Jean, C. Boehm, and J. Knoedlseder, *Constraints on dark matter and the shape of the Milky Way dark halo from the 511-keV line*, *Mon. Not. Roy. Astron. Soc.* **368** (2006) 1695–1705, [astro-ph/0507142].

[112] G. WEIDENSPOINTNER, G. SKINNER, P. JEAN, J. KNÖDLSEDER, P. VON BALLMOOS, G. BIGNAMI, R. DIEHL, A. W. STRONG, B. CORDIER, S. SCHANNE, et al., *An asymmetric distribution of positrons in the galactic disk revealed by γ-rays*, *Nature* **451** (2008), no. 7175 159–162.

[113] T. Bringmann, X. Huang, A. Ibarra, S. Vogl, and C. Weniger, *Fermi LAT Search for Internal Bremsstrahlung Signatures from Dark Matter Annihilation*, *JCAP* **1207** (2012) 054, [arXiv:1203.1312].

[114] **Fermi-LAT** Collaboration, M. Ackermann et al., *Search for gamma-ray spectral lines with the Fermi large area telescope and dark matter implications*, *Phys.Rev.* **D88** (2013) 082002, [arXiv:1305.5597].

[115] E. Bulbul, M. Markevitch, A. Foster, R. K. Smith, M. Loewenstein, and S. W. Randall, *Detection of An Unidentified Emission Line in the Stacked X-ray spectrum of Galaxy Clusters*, *Astrophys. J.* **789** (2014) 13, [arXiv:1402.2301].

[116] A. Boyarsky, O. Ruchayskiy, D. Iakubovskyi, and J. Franse, *Unidentified Line in X-Ray Spectra of the Andromeda Galaxy and Perseus Galaxy Cluster*, *Phys. Rev. Lett.* **113** (2014) 251301, [arXiv:1402.4119].

[117] O. Urban, N. Werner, S. W. Allen, A. Simionescu, J. S. Kaastra, and L. E. Strigari, *A Suzaku Search for Dark Matter Emission Lines in the X-ray Brightest Galaxy Clusters*, *Mon. Not. Roy. Astron. Soc.* **451** (2015) 2447, [arXiv:1411.0050].

[118] A. Boyarsky, J. Franse, D. Iakubovskyi, and O. Ruchayskiy, *Checking the dark matter origin of 3.53 keV line with the Milky Way center*, arXiv:1408.2503.

[119] S. Riemer-Sorensen, *Questioning a 3.5 keV dark matter emission line*, arXiv:1405.7943.

[120] J. M. Cline, Y. Farzan, Z. Liu, G. D. Moore, and W. Xue, *3.5 keV x rays as the "21 cm line" of dark atoms, and a link to light sterile neutrinos*, *Phys. Rev.* **D89** (2014) 121302, [arXiv:1404.3729].

[121] T. E. Jeltema and S. Profumo, *Discovery of a 3.5 keV line in the Galactic Center and a Critical Look at the Origin of the Line Across Astronomical Targets*, *Mon. Not. Roy. Astron. Soc.* **450** (2015), no. 2 2143–2152, [arXiv:1408.1699].

[122] V. Bonnivard, C. Combet, D. Maurin, A. Geringer-Sameth, S. M. Koushiappas, M. G. Walker, M. Mateo, E. W. Olszewski, and J. I. Bailey, III, *Dark matter annihilation and decay profiles for the Reticulum II dwarf spheroidal galaxy*, arXiv:1504.0330.

[123] D. P. Finkbeiner, *Microwave ism emission observed by wmap*, *Astrophys. J.* **614** (2004) 186–193, [astro-ph/0311547].

[124] D. Hooper, D. P. Finkbeiner, and G. Dobler, *Possible evidence for dark matter annihilations from the excess microwave emission around the center of the Galaxy seen by the Wilkinson Microwave Anisotropy Probe*, *Phys. Rev.* **D76** (2007) 083012, [arXiv:0705.3655].

[125] G. Dobler, D. P. Finkbeiner, I. Cholis, T. Slatyer, and N. Weiner, *The Fermi Haze: A Gamma-ray Counterpart to the Microwave Haze*, **717** (July, 2010) 825–842, [arXiv:0910.4583].

[126] D. Hooper and L. Goodenough, *Dark Matter Annihilation in The Galactic Center As Seen by the Fermi Gamma Ray Space Telescope*, *Phys.Lett.* **B697** (2011) 412–428, [arXiv:1010.2752].

[127] F. Calore, I. Cholis, and C. Weniger, *Background model systematics for the Fermi GeV excess*, arXiv:1409.0042.

[128] R. Bartels, S. Krishnamurthy, and C. Weniger, *Strong support for the millisecond pulsar origin of the Galactic center GeV excess*, arXiv:1506.0510.

[129] S. K. Lee, M. Lisanti, B. R. Safdi, T. R. Slatyer, and W. Xue, *Evidence for Unresolved Gamma-Ray Point Sources in the Inner Galaxy*, arXiv:1506.0512.

[130] I. Cholis, C. Evoli, F. Calore, T. Linden, C. Weniger, and D. Hooper, *The Galactic Center GeV Excess from a Series of Leptonic Cosmic-Ray Outbursts*, arXiv:1506.0511.

[131] A. Geringer-Sameth, M. G. Walker, S. M. Koushiappas, S. E. Koposov, V. Belokurov, et al., *Evidence for Gamma-ray Emission from the Newly Discovered Dwarf Galaxy Reticulum 2*, arXiv:1503.0232.

[132] D. Hooper and T. Linden, *On The Gamma-Ray Emission From Reticulum II and Other Dwarf Galaxies*, arXiv:1503.0620.

[133] **Fermi-LAT** Collaboration, M. Ackermann et al., *Searching for Dark Matter Annihilation from Milky Way Dwarf Spheroidal Galaxies with Six Years of Fermi-LAT Data*, arXiv:1503.0264.

[134] B. Bertoni, D. Hooper, and T. Linden, *Examining The Fermi-LAT Third Source Catalog In Search Of Dark Matter Subhalos*, arXiv:1504.0208.

[135] **Fermi-LAT, DES** Collaboration, A. Drlica-Wagner et al., *Search for Gamma-Ray Emission from DES Dwarf Spheroidal Galaxy Candidates with Fermi-LAT Data*, arXiv:1503.0263.

[136] D. Hooper, C. Kelso, and F. S. Queiroz, *Stringent and Robust Constraints on the Dark Matter Annihilation Cross Section From the Region of the Galactic Center*, *Astropart.Phys.* **46** (2013) 55–70, [arXiv:1209.3015].

[137] **Fermi-LAT** Collaboration, M. Ackermann et al., *Limits on Dark Matter Annihilation Signals from the Fermi LAT 4-year Measurement of the Isotropic Gamma-Ray Background*, arXiv:1501.0546.

[138] M. R. Buckley, E. Charles, J. M. Gaskins, A. M. Brooks, A. Drlica-Wagner, et al., *Search for Gamma-ray Emission from Dark Matter Annihilation in the Large Magellanic Cloud with the Fermi Large Area Telescope*, *Phys.Rev.D* (2015) [arXiv:1502.0102].

[139] L. Goodenough and D. Hooper, *Possible Evidence For Dark Matter Annihilation In The Inner Milky Way From The Fermi Gamma Ray Space Telescope*, arXiv:0910.2998.

[140] K. N. Abazajian and M. Kaplinghat, *Detection of a Gamma-Ray Source in the Galactic Center Consistent with Extended Emission from Dark Matter Annihilation and Concentrated Astrophysical Emission*, *Phys.Rev.* **D86** (2012) 083511, [arXiv:1207.6047].

[141] C. Gordon and O. Macias, *Dark Matter and Pulsar Model Constraints from Galactic Center Fermi-LAT Gamma Ray Observations*, *Phys.Rev.* **D88** (2013) 083521, [arXiv:1306.5725].

[142] D. Hooper and T. R. Slatyer, *Two Emission Mechanisms in the Fermi Bubbles: A Possible Signal of Annihilating Dark Matter*, *Phys.Dark Univ.* **2** (2013) 118–138, [arXiv:1302.6589].

[143] K. N. Abazajian, N. Canac, S. Horiuchi, and M. Kaplinghat, *Astrophysical and Dark Matter Interpretations of Extended Gamma-Ray Emission from the Galactic Center*, *Phys.Rev.* **D90** (2014) 023526, [arXiv:1402.4090].

[144] T. Daylan, D. P. Finkbeiner, D. Hooper, T. Linden, S. K. N. Portillo, et al., *The Characterization of the Gamma-Ray Signal from the Central Milky Way: A Compelling Case for Annihilating Dark Matter*, arXiv:1402.6703.

[145] F. Calore, I. Cholis, C. McCabe, and C. Weniger, *A Tale of Tails: Dark Matter Interpretations of the Fermi GeV Excess in Light of Background Model Systematics*, *Phys.Rev.* **D91** (2015), no. 6 063003, [arXiv:1411.4647].

[146] **PAMELA** Collaboration, O. Adriani et al., *Cosmic-Ray Positron Energy Spectrum Measured by PAMELA*, *Phys.Rev.Lett.* **111** (2013) 081102, [arXiv:1308.0133].

[147] M. e. Ackermann, *Measurement of Separate Cosmic-Ray Electron and Positron Spectra with the Fermi Large Area Telescope*, *Physical Review Letters* **108** (Jan., 2012) 011103, [arXiv:1109.0521].

[148] **AMS** Collaboration, L. Accardo et al., *High Statistics Measurement of the Positron Fraction in Primary Cosmic Rays of 0.5–500 GeV with the Alpha Magnetic Spectrometer on the International Space Station*, *Phys. Rev. Lett.* **113** (2014) 121101.

[149] **PAMELA** Collaboration, O. Adriani et al., *PAMELA results on the cosmic-ray antiproton flux from 60 MeV to 180 GeV in kinetic energy*, *Phys. Rev. Lett.* **105** (2010) 121101, [arXiv:1007.0821].

[150] G. Giesen, M. Boudaud, Y. Genolini, V. Poulin, M. Cirelli, P. Salati, and P. D. Serpico, *AMS-02 antiprotons, at last! Secondary astrophysical component and immediate implications for Dark Matter*, arXiv:1504.0427.

[151] T. Aramaki et al., *Review of the theoretical and experimental status of dark matter identification with cosmic-ray antideuterons*, arXiv:1505.0778.

[152] **IceCube** Collaboration, M. Aartsen et al., *Search for dark matter annihilations in the Sun with the 79-string IceCube detector*, *Phys.Rev.Lett.* **110** (2013), no. 13 131302, [arXiv:1212.4097].

[153] T. Tanaka, K. Abe, Y. Hayato, T. Iida, J. Kameda, Y. Koshio, Y. Kouzuma, M. Miura, S. Moriyama, M. Nakahata, et al., *An indirect search for weakly interacting massive particles in the sun using 3109.6 days of upward-going muons in super-kamiokande*, *The Astrophysical Journal* (2011).

[154] **IceCube** Collaboration, M. G. Aartsen et al., *Search for Dark Matter Annihilation in the Galactic Center with IceCube-79*, arXiv:1505.0725.

[155] B. Bertoni, D. Hooper, and T. Linden, *Is the Gamma-Ray Source 3FGL J2212.5+0703 a Dark Matter Subhalo? (in preparation)*, .

[156] S. D. White and C. S. Frenk, *Galaxy formation through hierarchical clustering*, *Astrophys.J.* **379** (1991) 52–79.

[157] **Fermi-LAT Collaboration** Collaboration, F. Acero et al., *Fermi Large Area Telescope Third Source Catalog*, arXiv:1501.0200.

[158] M. Kuhlen, J. Diemand, and P. Madau, *The Dark Matter Annihilation Signal from Galactic Substructure: Predictions for GLAST*, *Astrophys.J.* **686** (2008) 262, [arXiv:0805.4416].

[159] L. Pieri, G. Bertone, and E. Branchini, *Dark Matter Annihilation in Substructures Revised*, *Mon.Not.Roy.Astron.Soc.* **384** (2008) 1627, [arXiv:0706.2101].

[160] A. Berlin and D. Hooper, *Stringent Constraints on the Dark Matter Annihilation Cross Section From Subhalo Searches with the Fermi Gamma-Ray Space Telescope*, *Phys.Rev.* **D89** (2014), no. 1 016014, [arXiv:1309.0525].

[161] A. V. Belikov, D. Hooper, and M. R. Buckley, *Searching For Dark Matter Subhalos In the Fermi-LAT Second Source Catalog*, *Phys.Rev.* **D86** (2012) 043504, [arXiv:1111.2613].

[162] M. R. Buckley and D. Hooper, *Dark Matter Subhalos In the Fermi First Source Catalog*, *Phys.Rev.* **D82** (2010) 063501, [arXiv:1004.1644].

[163] H.-S. Zechlin, M. Fernandes, D. Elsaesser, and D. Horns, *Dark matter subhalos as Fermi gamma-ray sources and first candidates in the 1FGL catalog*, arXiv:1110.6868.

[164] N. Mirabal, V. Frias-Martinez, T. Hassan, and E. Frias-Martinez, *Fermi's Sibyl: Mining the gamma-ray sky for dark matter subhaloes*, *Mon.Not.Roy.Astron.Soc.* **424** (2012) L64, [arXiv:1205.4825].

[165] N. Mirabal, D. Nieto, and S. Pardo, *The exotic fraction among unassociated Fermi sources*, arXiv:1007.2644.

[166] H.-S. Zechlin and D. Horns, *Unidentified sources in the Fermi-LAT second source catalog: the case for dark matter subhalos*, *JCAP* **1211** (2012), no. 02 050, [arXiv:1210.3852].

[167] A. Geringer-Sameth, S. M. Koushiappas, and M. G. Walker, *A Comprehensive Search for Dark Matter Annihilation in Dwarf Galaxies*, arXiv:1410.2242.

[168] M. Di Mauro and F. Donato, *The composition of the Fermi-LAT IGRB intensity: emission from extragalactic point sources and dark matter annihilations*, arXiv:1501.0531.

[169] V. Springel, J. Wang, M. Vogelsberger, A. Ludlow, A. Jenkins, et al., *The Aquarius Project: the subhalos of galactic halos*, *Mon.Not.Roy.Astron.Soc.* **391** (2008) 1685–1711, [arXiv:0809.0898].

[170] M. A. Sanchez-Conde and F. Prada, *The flattening of the concentration-mass relation towards low halo masses and its implications for the annihilation signal boost*, *Mon.Not.Roy.Astron.Soc.* **442** (2014) 2271, [arXiv:1312.1729].

[171] J. S. Bullock, T. S. Kolatt, Y. Sigad, R. S. Somerville, A. V. Kravtsov, et al., *Profiles of dark haloes. Evolution, scatter, and environment*, *Mon.Not.Roy.Astron.Soc.* **321** (2001) 559–575, [astro-ph/9908159].

[172] J. Munoz-Cuartas, A. Maccio, S. Gottlober, and A. Dutton, *The Redshift Evolution of LCDM Halo Parameters: Concentration, Spin, and Shape*, *Mon.Not.Roy.Astron.Soc.* **411** (2011) 584, [arXiv:1007.0438].

[173] T. Sj[U+FFFD]strand, S. Ask, J. R. Christiansen, R. Corke, N. Desai, et al., *An Introduction to PYTHIA 8.2*, arXiv:1410.3012.

[174] J. Diemand and B. Moore, *The structure and evolution of cold dark matter halos*, *Adv.Sci.Lett.* **4** (2011) 297–310, [arXiv:0906.4340].

[175] S. Bogdanov and J. P. Halpern, *Identification of the high-energy gamma-ray source 3fgl j1544. 6–1125 as a transitional millisecond pulsar binary in an accreting state*, *The Astrophysical Journal Letters* **803** (2015), no. 2 L27.

[176] F. Camilo et al., *Parkes radio searches of Fermi gamma-ray sources and millisecond pulsar discoveries*, arXiv:1507.0445.

[177] F. K. Schinzel, L. Petrov, G. B. Taylor, E. K. Mahony, P. G. Edwards, and Y. Y. Kovalev, *New Associations of Gamma-Ray Sources from the Fermi Second Source Catalog*, *Astrophys. J. Suppl.* **217** (2015), no. 1 4, [arXiv:1408.6217].

[178] M. Sakai, Y. Yajima, and H. Matsumoto, *Nature of the Unidentified TeV Source HESS J1614-518, Revealed by Suzaku and XMM-Newton Observations*, **63** (Nov., 2011) 879, [arXiv:1110.3562].

[179] F. Acero, M. Ackermann, M. Ajello, A. Allafort, L. Baldini, et al., *Constraints on the Galactic Population of TeV Pulsar Wind Nebulae Using FERMI Large Area Telescope Observations*, *Astrophys.J.* **773** (2013) 77, [arXiv:1306.5735].

[180] G. Rowell, D. Horns, Y. Fukui, Y. Moriguchi, H. collaboration, et al., *A closer look at the unidentified tev source hess j1614—518*, in *HIGH ENERGY GAMMA-RAY ASTRONOMY: Proceedings of the 4th International Meeting on High Energy Gamma-Ray Astronomy*, vol. 1085, pp. 241–244, AIP Publishing, 2009.

[181] J. F. Navarro, C. S. Frenk, and S. D. M. White, *The Structure of cold dark matter halos*, *Astrophys. J.* **462** (1996) 563–575, [astro-ph/9508025].

[182] J. R. Mattox et al., *The Likelihood Analysis of EGRET Data*, **461** (Apr., 1996) 396.

[183] E. Massaro, P. Giommi, C. Leto, P. Marchegiani, A. Maselli, M. Perri, S. Piranomonte, and S. Sclavi, *Roma-BZCAT: A multifrequency catalogue of Blazars*, *Astron. Astrophys.* **495** (2009) 691, [arXiv:0810.2206].

[184] S. E. Healey, R. W. Romani, G. B. Taylor, E. M. Sadler, R. Ricci, et al., *CRATES: An All-Sky Survey of Flat-Spectrum Radio Sources*, *Astrophys.J.Suppl.* **171** (2007) 61–71, [astro-ph/0702346].

[185] S. E. Healey, R. W. Romani, G. Cotter, P. F. Michelson, E. F. Schlafly, et al., *CGRaBS: An All-Sky Survey of Gamma-Ray Blazar Candidates*, *Astrophys.J.Suppl.* **175** (2008) 97, [arXiv:0709.1735].

[186] R. N. Manchester, G. B. Hobbs, A. Teoh, and M. Hobbs, *The Australia Telescope National Facility pulsar catalogue*, *Astron. J.* **129** (2005) 1993, [astro-ph/0412641].

[187] N. Gehrels, *Confidence limits for small numbers of events in astrophysical data*, **303** (Apr., 1986) 336–346.

[188] L. Bergstrom, T. Bringmann, I. Cholis, D. Hooper, and C. Weniger, *New limits on dark matter annihilation from AMS cosmic ray positron data*, *Phys.Rev.Lett.* **111** (2013) 171101, [arXiv:1306.3983].

[189] **Fermi-LAT** Collaboration, A. Abdo et al., *The Second Fermi Large Area Telescope Catalog of Gamma-ray Pulsars*, *Astrophys.J.Suppl.* **208** (2013) 17, [arXiv:1305.4385].

[190] P. S. Parkinson, M. Dormody, M. Ziegler, P. Ray, A. Abdo, et al., *Eight gamma-ray pulsars discovered in blind frequency searches of Fermi LAT data*, *Astrophys.J.* **725** (2010) 571–584, [arXiv:1006.2134].

[191] P. Ray, M. Kerr, D. Parent, A. Abdo, L. Guillemot, et al., *Precise Gamma-Ray Timing and Radio Observations of 17 Fermi Gamma-Ray Pulsars*, *Astrophys.J.Suppl.* **194** (2011) 17, [arXiv:1011.2468].

[192] P. Ray, A. Abdo, D. Parent, D. Bhattacharya, B. Bhattacharyya, et al., *Radio Searches of Fermi LAT Sources and Blind Search Pulsars: The Fermi Pulsar Search Consortium*, arXiv:1205.3089.

[193] F. Camilo, P. Ray, S. Ransom, M. Burgay, T. Johnson, et al., *Radio detection of LAT PSRs J1741-2054 and J2032+4127: no longer just gamma-ray pulsars*, *Astrophys.J.* **705** (2009) 1–13, [arXiv:0908.2626].

[194] **Fermi Pulsar Timing Consortium** Collaboration, A. Abdo and A. Abdo, *PSR J1907+0602: A Radio-Faint Gamma-Ray Pulsar Powering a Bright TeV Pulsar Wind Nebula*, *Astrophys.J.* **711** (2010) 64–74, [arXiv:1001.0792].

[195] H. Pletsch, L. Guillemot, B. Allen, M. Kramer, C. Aulbert, et al., *Discovery of Nine Gamma-Ray Pulsars in Fermi-LAT Data Using a New Blind Search Method*, *Astrophys.J.* **744** (2012) 105, [arXiv:1111.0523].

[196] B. Bertoni, S. Ipek, D. McKeen, and A. E. Nelson, *Constraints and consequences of reducing small scale structure via large dark matter-neutrino interactions*, *JHEP* **04** (2015) 170, [arXiv:1412.3113].

[197] L. G. van den Aarssen, T. Bringmann, and C. Pfrommer, *Is dark matter with long-range interactions a solution to all small-scale problems of ΛCDM cosmology?*, *Phys. Rev. Lett.* **109** (2012) 231301, [arXiv:1205.5809].

[198] T. Bringmann, J. Hasenkamp, and J. Kersten, *Tight bonds between sterile neutrinos and dark matter*, *JCAP* **1407** (2014) 042, [arXiv:1312.4947].

[199] P. Ko and Y. Tang, *$\nu\Lambda$Mdark matter: A Model for Sterile Neutrino and Dark Matter Reconciles Cosmological and Neutrino Oscillation Data after BICEP2*, *Phys. Lett. B* **739** (2014) 62–67, [arXiv:1404.0236].

[200] M. Archidiacono, S. Hannestad, R. S. Hansen, and T. Tram, *Cosmology with self-interacting sterile neutrinos and dark matter - A pseudoscalar model*, arXiv:1404.5915.

[201] J. F. Cherry, A. Friedland, and I. M. Shoemaker, *Neutrino Portal Dark Matter: From Dwarf Galaxies to IceCube*, arXiv:1411.1071.

[202] L. E. Strigari, J. S. Bullock, M. Kaplinghat, J. D. Simon, M. Geha, et al., *A common mass scale for satellite galaxies of the Milky Way*, *Nature* **454** (2008) 1096–1097, [arXiv:0808.3772].

[203] M. Viel, G. D. Becker, J. S. Bolton, and M. G. Haehnelt, *Warm dark matter as a solution to the small scale crisis: New constraints from high redshift Lyman-α forest data*, *Phys. Rev. D* **88** (2013) 043502, [arXiv:1306.2314].

[204] S. Vegetti, D. Lagattuta, J. McKean, M. Auger, C. Fassnacht, et al., *Gravitational detection of a low-mass dark satellite at cosmological distance*, arXiv:1201.3643.

[205] S. Vegetti, L. Koopmans, M. Auger, T. Treu, and A. Bolton, *Inference of the Cold Dark Matter substructure mass function at z=0.2 using strong gravitational lenses*, arXiv:1405.3666.

[206] A. M. Green, S. Hofmann, and D. J. Schwarz, *The First wimpy halos*, *JCAP* **0508** (2005) 003, [astro-ph/0503387].

[207] A. Loeb and M. Zaldarriaga, *The Small-scale power spectrum of cold dark matter*, *Phys. Rev. D* **71** (2005) 103520, [astro-ph/0504112].

[208] T. Bringmann, *Particle Models and the Small-Scale Structure of Dark Matter*, *New J. Phys.* **11** (2009) 105027, [arXiv:0903.0189].

[209] **Planck** Collaboration, P. Ade et al., *Planck 2013 results. XVI. Cosmological parameters*, *Astron. Astrophys.* (2014) [arXiv:1303.5076].

[210] F. Iocco, G. Mangano, G. Miele, O. Pisanti, and P. D. Serpico, *Primordial Nucleosynthesis: from precision cosmology to fundamental physics*, *Phys. Rept.* **472** (2009) 1–76, [arXiv:0809.0631].

[211] P. D. Serpico and G. G. Raffelt, *MeV-mass dark matter and primordial nucleosynthesis*, *Phys. Rev. D* **70** (2004) 043526, [astro-ph/0403417].

[212] R. J. Wilkinson, C. Boehm, and J. Lesgourgues, *Constraining Dark Matter-Neutrino Interactions using the CMB and Large-Scale Structure*, *JCAP* **1405** (2014) 011, [arXiv:1401.7597].

[213] C. Boehm, M. J. Dolan, and C. McCabe, *A Lower Bound on the Mass of Cold Thermal Dark Matter from Planck*, *JCAP* **1308** (2013) 041, [arXiv:1303.6270].

[214] K. M. Nollett and G. Steigman, *BBN And The CMB Constrain Neutrino Coupled Light WIMPs*, arXiv:1411.6005.

[215] D. Britton, S. Ahmad, D. Bryman, R. Burnham, E. Clifford, et al., *Improved search for massive neutrinos in $\pi^+ \to e^+\nu$ decay*, *Phys. Rev. D* **46** (1992) 885–887.

[216] **PIENU** Collaboration, M. Aoki et al., *Search for Massive Neutrinos in the Decay $\pi \to e\nu$*, *Phys. Rev. D* **84** (2011) 052002, [arXiv:1106.4055].

[217] R. Abela, M. Daum, G. Eaton, R. Frosch, B. Jost, et al., *Search for an Adark matterixture of Heavy Neutrino in Pion Decay*, *Phys. Lett. B* **105** (1981) 263–266.

[218] R. Hayano, T. Taniguchi, T. Yamanaka, T. Tanimori, R. Enomoto, et al., *Heavy-Neutrino Search Using $K_{\mu 2}$ Decay* , *Phys. Rev. Lett.* **49** (1982) 1305.

[219] A. Artamonov, B. Bassalleck, B. Bhuyan, E. Blackmore, D. Bryman, et al., *Search for heavy neutrinos in $K^+ \to \mu^+\nu_H$ decays*, arXiv:1411.3963.

[220] D. Britton, S. Ahmad, D. Bryman, R. Burnbam, E. Clifford, et al., *Measurement of the $\pi^+ \to e^+\nu$ branching ratio*, *Phys. Rev. Lett.* **68** (1992) 3000–3003.

[221] G. Czapek, A. Federspiel, A. Fluckiger, D. Frei, B. Hahn, et al., *Branching ratio for the rare pion decay into positron and neutrino*, *Phys. Rev. Lett.* **70** (1993) 17–20.

[222] W. J. Marciano and A. Sirlin, *Radiative corrections to $\pi_{\ell 2}$ decays*, *Phys. Rev. Lett.* **71** (1993) 3629–3632.

[223] **MuLan Collaboration** Collaboration, V. Tishchenko et al., *Detailed Report of the MuLan Measurement of the Positive Muon Lifetime and Determination of the Fermi Constant*, *Phys. Rev. D* **87** (2013), no. 5 052003, [arXiv:1211.0960].

[224] **TWIST** Collaboration, R. Bayes et al., *New Experimental Constraints for the Standard Model from Muon Decay*, arXiv:1010.4998.

[225] S. N. Gninenko, *A resolution of puzzles from the LSND, KARMEN, and MiniBooNE experiments*, *Phys. Rev. D* **83** (2011) 015015, [arXiv:1009.5536].

[226] **Particle Data Group** Collaboration, K. Olive et al., *Review of Particle Physics*, *Chin. Phys.* **38** (2014) 090001.

[227] **ALEPH** Collaboration, R. Barate et al., *An Upper limit on the tau-neutrino mass from three-prong and five-prong tau decays*, *Eur. Phys. J. C* **2** (1998) 395–406.

[228] **Belle** Collaboration, K. Belous et al., *Measurement of the τ-lepton lifetime at Belle*, *Phys. Rev. Lett.* **112** (2014), no. 3 031801, [arXiv:1310.8503].

[229] A. Pich, *Precision Tau Physics*, *Prog. Part. Nucl. Phys.* **75** (2014) 41–85, [arXiv:1310.7922].

[230] J. C. Helo, S. Kovalenko, and I. Schmidt, *On sterile neutrino mixing with ν_τ*, *Phys. Rev. D* **84** (2011) 053008, [arXiv:1105.3019].

[231] M. Gonzalez-Garcia, M. Maltoni, and T. Schwetz, *Updated fit to three neutrino mixing: status of leptonic CP violation*, arXiv:1409.5439.

[232] L. Wolfenstein, *Neutrino Oscillations in Matter*, *Phys. Rev. D* **17** (1978) 2369–2374.

[233] S. Mikheev and A. Y. Smirnov, *Resonance Amplification of Oscillations in Matter and Spectroscopy of Solar Neutrinos*, *Sov. J. Nucl. Phys.* **42** (1985) 913–917.

[234] B. Pontecorvo, *Neutrino Experiments and the Problem of Conservation of Leptonic Charge*, *Sov. Phys. JETP* **26** (1968) 984–988.

[235] **Daya Bay** Collaboration, F. An et al., *Spectral measurement of electron antineutrino oscillation amplitude and frequency at Daya Bay*, *Phys. Rev. Lett.* **112** (2014) 061801, [arXiv:1310.6732].

[236] R. J. Wilkes, *New results from super-k and k2k*, *ECONF* **C020805** (2002) TTH02, [hep-ex/0212035].

[237] **MINOS** Collaboration, P. Adamson et al., *Measurement of the neutrino mass splitting and flavor mixing by MINOS*, *Phys. Rev. Lett.* **106** (2011) 181801, [arXiv:1103.0340].

[238] **KamLAND** Collaboration, K. Eguchi et al., *First results from kamland: Evidence for reactor anti- neutrino disappearance*, *Phys. Rev. Lett.* **90** (2003) 021802, [hep-ex/0212021].

[239] **SNO** Collaboration, B. Aharmim et al., *Combined Analysis of all Three Phases of Solar Neutrino Data from the Sudbury Neutrino Observatory*, *Phys. Rev. C* **88** (2013) 025501, [arXiv:1109.0763].

[240] **Borexino** Collaboration, G. Bellini et al., *Measurement of the solar 8B neutrino rate with a liquid scintillator target and 3 MeV energy threshold in the Borexino detector*, *Phys. Rev. D* **82** (2010) 033006, [arXiv:0808.2868].

[241] **Borexino** Collaboration, D. D'Angelo et al., *Recent Borexino results and prospects for the near future*, arXiv:1405.7919.

[242] A. M. Serenelli, W. Haxton, and C. Pena-Garay, *Solar models with accretion. I. Application to the solar abundance problem*, *Astrophys. J.* **743** (2011) 24, [arXiv:1104.1639].

[243] S. Dev and S. Kumar, *Constraints on weakly mixed sterile neutrinos in the light of SNO salt phase and 766.3 Ty KamLAND data*, *Mod. Phys. Lett. A* **20** (2005) 2957–2968, [hep-ph/0504237].

[244] M. Cirelli, G. Marandella, A. Strumia, and F. Vissani, *Probing oscillations into sterile neutrinos with cosmology, astrophysics and experiments*, *Nucl. Phys. B* **708** (2005) 215–267, [hep-ph/0403158].

[245] **Super-Kamiokande** Collaboration, K. Abe et al., *Limits on Sterile Neutrino Mixing using Atmospheric Neutrinos in Super-Kamiokande*, arXiv:1410.2008.

[246] A. Esmaili and A. Y. Smirnov, *Probing Non-Standard Interaction of Neutrinos with IceCube and DeepCore*, *JHEP* **1306** (2013) 026, [arXiv:1304.1042].

[247] E. Akhmedov, A. Kartavtsev, M. Lindner, L. Michaels, and J. Smirnov, *Improving Electro-Weak Fits with TeV-scale Sterile Neutrinos*, *JHEP* **1305** (2013) 081, [arXiv:1302.1872].

[248] S. Schael et al., *Precision electroweak measurements on the Z resonance*, *Phys. Rept.* **427** (2006) 257–454, [hep-ex/0509008].

[249] J. Orloff, A. N. Rozanov, and C. Santoni, *Limits on the mixing of tau neutrino to heavy neutrinos*, *Phys. Lett. B* **550** (2002) 8–15, [hep-ph/0208075].

[250] **NOMAD** Collaboration, P. Astier et al., *Search for heavy neutrinos mixing with tau neutrinos*, *Phys. Lett. B* **506** (2001) 27–38, [hep-ex/0101041].

[251] **DELPHI** Collaboration, P. Abreu et al., *Search for neutral heavy leptons produced in Z decays*, *Z. Phys. C* **74** (1997) 57–71.

[252] B. Batell, M. Pospelov, and A. Ritz, *Exploring Portals to a Hidden Sector Through Fixed Targets*, *Phys. Rev. D* **80** (2009) 095024, [arXiv:0906.5614].

[253] P. deNiverville, M. Pospelov, and A. Ritz, *Observing a light dark matter beam with neutrino experiments*, *Phys. Rev. D* **84** (2011) 075020, [arXiv:1107.4580].

[254] P. deNiverville, D. McKeen, and A. Ritz, *Signatures of sub-GeV dark matter beams at neutrino experiments*, *Phys. Rev. D* **86** (2012) 035022, [arXiv:1205.3499].

[255] B. Batell, P. deNiverville, D. McKeen, M. Pospelov, and A. Ritz, *Leptophobic Dark Matter at Neutrino Factories*, arXiv:1405.7049.

[256] P. P. Giardino, K. Kannike, I. Masina, M. Raidal, and A. Strumia, *The universal Higgs fit*, *JHEP* **1405** (2014) 046, [arXiv:1303.3570].

[257] D. Hooper, M. Kaplinghat, L. E. Strigari, and K. M. Zurek, *MeV Dark Matter and Small Scale Structure*, *Phys. Rev. D* **76** (2007) 103515, [arXiv:0704.2558].

[258] P. Gondolo, J. Hisano, and K. Kadota, *The Effect of quark interactions on dark matter kinetic decoupling and the mass of the smallest dark halos*, *Phys. Rev. D* **86** (2012) 083523, [arXiv:1205.1914].

[259] T. Bringmann and S. Hofmann, *Thermal decoupling of WIMPs from first principles*, *JCAP* **0407** (2007) 016, [hep-ph/0612238].

[260] M. R. Buckley, J. Zavala, F.-Y. Cyr-Racine, K. Sigurdson, and M. Vogelsberger, *Scattering, Damping, and Acoustic Oscillations: Simulating the Structure of Dark Matter Halos with Relativistic Force Carriers*, *Phys. Rev. D* **90** (2014) 043524, [arXiv:1405.2075].

[261] H.-T. Janka, K. Langanke, A. Marek, G. Martinez-Pinedo, and B. Mueller, *Theory of Core-Collapse Supernovae*, *Phys. Rept.* **442** (2007) 38–74, [astro-ph/0612072].

[262] H.-T. Janka, *Explosion Mechanisms of Core-Collapse Supernovae*, *Ann. Rev. Nucl. Part. Sci.* **62** (2012) 407–451, [arXiv:1206.2503].

[263] D. A. Dicus, S. Nussinov, P. B. Pal, and V. L. Teplitz, *Implications of Relativistic Gas Dynamics for Neutrino-neutrino Cross-sections*, *Phys. Lett. B* **218** (1989) 84.

[264] P. Fayet, D. Hooper, and G. Sigl, *Constraints on light dark matter from core-collapse supernovae*, *Phys. Rev. Lett.* **96** (2006) 211302, [hep-ph/0602169].

[265] D. McKeen and A. E. Nelson, *in preparation*, .

[266] G. Mangano, A. Melchiorri, P. Serra, A. Cooray, and M. Kamionkowski, *Cosmological bounds on dark matter-neutrino interactions*, *Phys. Rev. D* **74** (2006) 043517, [astro-ph/0606190].

[267] Y. Farzan and S. Palomares-Ruiz, *Dips in the Diffuse Supernova Neutrino Background*, *JCAP* **1406** (2014) 014, [arXiv:1401.7019].

[268] K. Blum, A. Hook, and K. Murase, *High energy neutrino telescopes as a probe of the neutrino mass mechanism*, arXiv:1408.3799.

[269] I. M. Nugent, *Determination of $|V_{us}|$ from τ Decays*, arXiv:1301.0637.

[270] S. Choubey and T. Ohlsson, *Bounds on Non-Standard Neutrino Interactions Using PINGU*, *Phys. Lett. B* **739** (2014) 357–364, [arXiv:1410.0410].

[271] R. Alonso, S. Antusch, M. Blennow, P. Coloma, A. de Gouvea, et al., *Summary report of MINSIS workshop in Madrid*, arXiv:1009.0476.

[272] B. Bertoni, A. E. Nelson, and S. Reddy, *Dark Matter Thermalization in Neutron Stars*, *Phys. Rev.* **D88** (2013) 123505, [arXiv:1309.1721].

[273] W. H. Press and D. N. Spergel, *Effect of hypothetical, weakly interacting, massive particles on energy transport in the solar interior*, *Astrophys. J.* **294** (1985) 663–673.

[274] W. H. Press and D. N. Spergel, *Capture by the sun of a galactic population of weakly interacting massive particles*, *Astrophys. J.* **296** (1985) 679–684.

[275] I. Goldman and S. Nussinov, *Weakly interacting massive particles and neutron stars*, *Phys. Rev. D* **40** (Nov, 1989) 3221–3230.

[276] A. Gould, B. T. Draine, R. W. Romani, and S. Nussinov, *NEUTRON STARS: GRAVEYARD OF CHARGED DARK MATTER*, *Phys.Lett.* **B238** (1990) 337.

[277] G. Bertone and M. Fairbairn, *Compact Stars as Dark Matter Probes*, *Phys.Rev.* **D77** (2008) 043515, [arXiv:0709.1485].

[278] C. Kouvaris, *WIMP Annihilation and Cooling of Neutron Stars*, *Phys.Rev.* **D77** (2008) 023006, [arXiv:0708.2362].

[279] A. de Lavallaz and M. Fairbairn, *Neutron Stars as Dark Matter Probes*, *Phys.Rev.* **D81** (2010) 123521, [arXiv:1004.0629].

[280] C. Kouvaris and P. Tinyakov, *Can Neutron stars constrain Dark Matter?*, *Phys.Rev.* **D82** (2010) 063531, [arXiv:1004.0586].

[281] C. Kouvaris and P. Tinyakov, *Constraining asymmetric dark matter through observations of compact stars*, *Physical Review D* **83** (2011), no. 8 083512.

[282] C. Kouvaris and P. Tinyakov, *Excluding Light Asymmetric Bosonic Dark Matter*, *Phys.Rev.Lett.* **107** (2011) 091301, [arXiv:1104.0382].

[283] C. Kouvaris and P. Tinyakov, *On (not)-constraining heavy asymmetric bosonic dark matter*, *arXiv preprint arXiv:1212.4075* (2012).

[284] S. D. McDermott, H.-B. Yu, and K. M. Zurek, *Constraints on scalar asymmetric dark matter from black hole formation in neutron stars*, *Physical Review D* **85** (2012), no. 2 023519.

[285] C. Kouvaris, *Limits on Self-Interacting Dark Matter*, *Phys.Rev.Lett.* **108** (2012) 191301, [arXiv:1111.4364].

[286] T. Guver, A. E. Erkoca, M. H. Reno, and I. Sarcevic, *On the capture of dark matter by neutron stars*, arXiv:1201.2400.

[287] J. Bramante, K. Fukushima, and J. Kumar, *Constraints on Bosonic Dark Matter From Observations of Old Neutron Stars*, *Phys.Rev.* **D87** (2013) 055012, [arXiv:1301.0036].

[288] N. F. Bell, A. Melatos, and K. Petraki, *Realistic neutron star constraints on bosonic asymmetric dark matter*, *Phys.Rev.* **D87** (2013) 123507, [arXiv:1301.6811].

[289] J. Fuller and C. Ott, *Dark Matter-induced Collapse of Neutron Stars: A Possible Link Between Fast Radio Bursts and the Missing Pulsar Problem*, *Mon. Not. Roy. Astron. Soc.* **450** (2015), no. 1 L71–L75, [arXiv:1412.6119].

[290] J. Bramante and T. Linden, *Detecting Dark Matter with Imploding Pulsars in the Galactic Center*, *Phys. Rev. Lett.* **113** (2014), no. 19 191301, [arXiv:1405.1031].

[291] M. Ángeles Pérez-García and J. Silk, *Constraining decaying dark matter with neutron stars*, *Phys. Lett.* **B744** (2015) 13–17, [arXiv:1403.6111].

[292] C. Kouvaris and M. A. Perez-Garcia, *Can Dark Matter explain the Braking Index of Neutron Stars?*, *Phys. Rev.* **D89** (2014), no. 10 103539, [arXiv:1401.3644].

[293] C. Kouvaris and P. Tinyakov, *Growth of Black Holes in the interior of Rotating Neutron Stars*, *Phys. Rev.* **D90** (2014), no. 4 043512, [arXiv:1312.3764].

[294] J. Bramante, K. Fukushima, J. Kumar, and E. Stopnitzky, *Bounds on self-interacting fermion dark matter from observations of old neutron stars*, *Phys. Rev.* **D89** (2014), no. 1 015010, [arXiv:1310.3509].

[295] X. Huang, X.-P. Zheng, W.-H. Wang, and S.-Z. Li, *Constraints on millicharged particles by neutron stars*, *Phys. Rev.* **D91** (2015), no. 12 123513.

[296] R. N. Manchester, G. B. Hobbs, A. Teoh, and M. Hobbs, *The Australia Telescope National Facility pulsar catalogue*, *Astron.J.* **129** (2005) 1993, [astro-ph/0412641].

[297] K. M. Zurek, *Asymmetric Dark Matter: Theories, Signatures, and Constraints*, arXiv:1308.0338.

[298] K. Petraki and R. R. Volkas, *Review of asymmetric dark matter*, *Int.J.Mod.Phys.* **A28** (2013) 1330028, [arXiv:1305.4939].

[299] A. O. Jamison, *Effects of gravitational confinement on bosonic asymmetric dark matter in stars*, arXiv:1304.3773.

[300] T. Gherghetta, C. F. Kolda, and S. P. Martin, *Flat directions in the scalar potential of the supersymmetric standard model*, *Nucl.Phys.* **B468** (1996) 37–58, [hep-ph/9510370].

[301] N. Arkani-Hamed, L. J. Hall, H. Murayama, D. Tucker-Smith, and N. Weiner, *Small neutrino masses from supersymmetry breaking*, *Phys.Rev.* **D64** (2001) 115011, [hep-ph/0006312].

[302] D. Hooper, J. March-Russell, and S. M. West, *Asymmetric sneutrino dark matter and the Omega(b) / Omega(dark matter) puzzle*, *Phys. Lett.* **B605** (2005) 228–236, [hep-ph/0410114].

[303] S. Gopalakrishna, A. de Gouvea, and W. Porod, *Right-handed sneutrinos as nonthermal dark matter*, *JCAP* **0605** (2006) 005, [hep-ph/0602027].

[304] G. Belanger, M. Kakizaki, E. Park, S. Kraml, and A. Pukhov, *Light mixed sneutrinos as thermal dark matter*, *JCAP* **1011** (2010) 017, [arXiv:1008.0580].

[305] T. Hebbeker, *Can the sneutrino be the lightest supersymmetric particle?*, *Phys.Lett.* **B470** (1999) 259–262, [hep-ph/9910326].

[306] J. I. Kapusta and C. Gale, *Finite-Temperature Field Theory Principles and Applications*. Cambridge University Press, Cambridge, 2006.

[307] S. Doniach and E. H. Sondheimer, *Green's Functions for Solid State Physicists*. W. A. Benjamin, Inc., Massachusetts, 1974.

[308] S. Reddy, M. Prakash, and J. M. Lattimer, *Neutrino interactions in hot and dense matter*, *Phys.Rev.* **D58** (1998) 013009, [astro-ph/9710115].

[309] K. Saito, T. Maruyama, and K. Soutome, *Collective modes in hot and dense matter*, *Phys.Rev.* **C40** (1989) 407–431.

[310] S. Reddy. private communication, 2013.

[311] N. K. Glendenning, *Compact Stars*. Springer-Verlag, New York, 1997.

[312] J. Lattimer and M. Prakash, *The physics of neutron stars*, *Science* **304** (2004) 536–542, [astro-ph/0405262].

[313] D. Page and S. Reddy, *Dense Matter in Compact Stars: Theoretical Developments and Observational Constraints*, *Ann.Rev.Nucl.Part.Sci.* **56** (2006) 327–374, [astro-ph/0608360].

[314] D. Page, M. Prakash, J. M. Lattimer, and A. W. Steiner, *Superfluid Neutrons in the Core of the Neutron Star in Cassiopeia A*, arXiv:1110.5116.

[315] T. Takatsuka and R. Tamagaki, *Superfluidity in neutron star matter and symmetric nuclear matter*, *Prog.Theor.Phys.Suppl.* **112** (1993) 27–66.

[316] J. Bardeen, L. N. Cooper, and J. R. Schrieffer, *Theory of superconductivity*, *Phys. Rev.* **108** (Dec, 1957) 1175–1204.

[317] A. Burrows, S. Reddy, and T. A. Thompson, *Neutrino opacities in nuclear matter*, *Nucl.Phys.* **A777** (2006) 356–394, [astro-ph/0404432].

[318] F. Camilo and F. A. Rasio, *Pulsars in globular clusters*, *ASP Conf.Ser.* (2005) [astro-ph/0501226].

[319] M. McCullough and M. Fairbairn, *Capture of Inelastic Dark Matter in White Dwarves*, *Phys.Rev.* **D81** (2010) 083520, [arXiv:1001.2737].

[320] C. Conroy, A. Loeb, and D. Spergel, *Evidence Against Dark Matter Halos Surrounding the Globular Clusters MGC1 and NGC 2419*, *Astrophys.J.* **741** (2011) 72, [arXiv:1010.5783].

[321] S. Weinberg, *Superconductivity For Particular Theorists*, *Prog.Theor.Phys.Suppl.* **86** (1986) 43.

[322] A. Schwenk and B. Friman, *Polarization contributions to the spin dependence of the effective interaction in neutron matter*, *Phys.Rev.Lett.* **92** (2004) 082501, [nucl-th/0307089].

[323] P. F. Bedaque, G. Rupak, and M. J. Savage, *Goldstone bosons in the 3P(Z) superfluid phase of neutron matter and neutrino emission*, *Phys.Rev.* **C68** (2003) 065802, [nucl-th/0305032].

[324] M. Plischke and B. Bergersen, *Equilibrium Statistical Physics*. World Scientific Publishing Co. Pte. Ltd., Singapore, 2006.

[325] D. T. Son and M. Wingate, *General coordinate invariance and conformal invariance in nonrelativistic physics: Unitary Fermi gas*, *Annals of Physics* **321** (Jan., 2006) 197–224, [cond-mat/].

[326] M. Baldo and C. Ducoin, *Elementary excitations in homogeneous superfluid neutron star matter: Role of the proton component*, *Phys.Rev.* **C84** (2011) 035806, [arXiv:1105.1311].

[327] M. G. Alford, K. Rajagopal, and F. Wilczek, *Color flavor locking and chiral symmetry breaking in high density QCD*, *Nucl.Phys.* **B537** (1999) 443–458, [hep-ph/9804403].

[328] M. G. Alford, A. Schmitt, K. Rajagopal, and T. Schäfer, *Color superconductivity in dense quark matter*, *Rev.Mod.Phys.* **80** (2008) 1455–1515, [arXiv:0709.4635].

[329] P. F. Bedaque and T. Schäfer, *High density quark matter under stress*, *Nucl.Phys.* **A697** (2002) 802–822, [hep-ph/0105150].

[330] D. B. Kaplan and S. Reddy, *Novel phases and transitions in color flavor locked matter*, *Phys.Rev.* **D65** (2002) 054042, [hep-ph/0107265].

[331] D. Son and M. A. Stephanov, *Inverse meson mass ordering in color flavor locking phase of high density QCD*, *Phys.Rev.* **D61** (2000) 074012, [hep-ph/9910491].